Title
Convection and Gravity Waves in the Tropical Atmosphere

Author
Edman, Jacob Patrick

Publication Date
2017

Convection and Gravity Waves in the Tropical Atmosphere

By

Jacob P. Edman

A dissertation submitted in partial satisfaction of the

requirements for the degree of

Doctor of Philosophy

in

Earth and Planetary Science

in the

Graduate Division

of the

University of California, Berkeley

Committee in charge:

Professor David M. Romps, Chair
Professor John C.H. Chiang
Professor William D. Collins
Professor Inez Fung

Fall 2017

Convection and Gravity Waves in the Tropical Atmosphere

Abstract

Convection and Gravity Waves in the Tropical Atmosphere

by

Jacob P. Edman

Doctor of Philosophy in Earth and Planetary Science

University of California, Berkeley

Professor David M. Romps, Chair

Moist convective clouds play a key role in the earth's energy and water cycles, but their turbulent and localized nature makes it difficult to study how they interact with the large-scale atmospheric circulation. In this dissertation, we study the interaction between convection and the large-scale tropical atmosphere in two ways. First, we develop simple analytical models for how convection interacts with large-scale circulations in the tropical atmosphere. These models are primarily based on a traditional-but-crude approximation of gravity wave dynamics, in which the tropopause is assumed to be a rigid lid. We test these models in cloud-resolving numerical simulations of a small patch of tropical atmosphere and determine that some of these methods pass a simple test of self-consistency, but are far from perfect. Alternately, we take a more sophisticated analytical approach– instead of using the traditional rigid lid model of the tropical atmosphere, we derive novel analytical solutions for pulses of buoyancy (a crude representation of the effects of convective clouds) in an atmosphere with both a troposphere and a stratosphere. This construction allows wave energy to realistically radiate out of the troposphere. We find that allowing wave energy to radiate out of the troposphere causes buoyancy anomalies in the troposphere to decay on timescales of hours to days, in stark contrast to the rigid lid model, which predicts that buoyancy anomalies persist forever in the absence of dissipation.

For Jessica

Contents

List of Figures

List of Tables

Acknowledgments

When I began my time at UC Berkeley, I could not have imagined a better mentor, role model, and friend than I found in my advisor, David Romps. My time in the Romps group has shaped who I am as a person and a scientist, in no small part due to my fellow groupmates Nadir Jeevanjee, Jake Seeley, Wolfgang Langhans, Da Yang, Rusen Oktem, Suqin Duan, Bowen Zhou, and Kyongmin Yeo. Also, I thank the rest of my committee, Inez Fung, John Chiang, and Bill Collins; your mentorship and advice has been invaluable.

Getting to this point certainly would not have been possible without the love and support of the family and friends who have made me a part of their lives. First and foremost, I thank my parents, Barbara and Ron, without whom I would not be here. I am infinitely grateful for your neverending belief in me, and for providing me the opportunities to find my place in the world. I also would not have made it this far without my wife Jessica, and her love and support over the last 5 years. Thank you for being there when I get home in the evening and when I wake up in the morning, for being an adventure companion, and, most importantly, for always reminding me that there is a lot more to life than being a graduate student. For that, I also thank my old friends, Kelsey, Alexandre, Mitchell, and John. I am very glad you are all still with me.

I am also indebted to the many other current and former residents of McCone Hall who welcomed and helped me along the way, including Noah Randolph-Flagg, William Hawley, Stephanie Wuerth, Percy Link, Jesse Day, Tyler Arbour, Octavia Crompton, Tripti Bhattacharya, Ben Fildier, Chris Johnson, Prabhat, Steve Breen, Chelsea Willett, Hannah Bourne, Courtney Sprain, Marissa Tremblay, and Avinash Nayak.

Trail running has been invaluable to my success as a graduate student, so I would also like to express my appreciation to the UC Berkeley fire trails and East Bay Regional Park system for always being around when I needed you, even if you are a bit muddy sometimes. I have spent many, many excellent afternoons and evenings running up the Strawberry Canyon fire trail with Stephanie Wuerth, Clara Eng, Jake Seeley, Noah Randolph-Flagg, and William Hawley. Thank you to Stephanie in particular, for bringing me to the realization that running more than 26.2 miles is awesome, and also for accompanying me for many of the subsequent miles.

For everyone who has been a part of my life so far, thank you for sharing a part of your life with me, and I hope we have not already met for the last time. I would not be the human I am today without all of you.

This dissertation was typeset using the ucastrothesis LaTeX template.

Chapter 1

Introduction

Despite being a vital part of earth's energy and water cycles, many aspects of moist convection in the atmosphere remain poorly understood. The ongoing struggle to parameterize moist convection in global climate models (GCMs) is a prime example of the multiscale complexity of moist convection. A GCM resolves the large-scale atmospheric circulation, but at the time of writing, typical horizontal grid resolutions (50-200 km) are much too coarse to resolve the dynamics of moist convection, which occurs on scales of hundreds of meters to kilometers. This scale separation would seem to lend itself well to parameterization– it certainly makes sense in the midlatitudes, where earth's rotation organizes large-scale atmospheric circulations into the familiar cyclones which bring California most of its rain. These cyclones are much larger and persist for much longer than any individual convective cloud, so their dynamics can be largely understood without considering convection directly. However, in the tropics, where the influence of earth's rotation is negligible, the primary slow, "external", forcing is radiative cooling of the atmosphere. This radiative cooling and the associated downward mass flux is balanced by moist convection. Convective clouds transport energy and water vapor high into the atmosphere, fueled by latent heat released as they ascend. The amount of energy transported by moist convection depends on the rate at which the atmosphere cools, which is in turn tied to the temperature and water vapor content of the atmosphere. Because of this, moist convection directly feeds back on the large-scale circulation in the tropics, which makes disentangling convection from the large-scale circulation quite difficult. In this dissertation, we attempt to gain a deeper understanding of the interactions between convection and large-scale circulations by employing a combination of simple models and analytical techniques.

Chapters 2 and 3 are devoted to understanding how a small patch of tropical atmosphere interacts with the surrounding environment. Is there a simple, self-consistent way of describing the large-scale atmospheric response to an anomalous burst of convection in the patch? In these chapters, we seek to model a single patch of atmosphere, either analytically or using a cloud-resolving model (CRM), and parameterize the large-scale circulation. This type of parameterization has been called a 'supradomain-scale' (SDS) parameterization. There are two main approaches to SDS parameterization, known as the weak-temperature-gradient (WTG) approximation and the weak-pressure-gradient (WPG) approximation. Both approaches take advantage of the fact that horizontal density and temperature gradients must be small in the tropical atmosphere. As we show in Appendix A.1, density gradients are small in the tropics due to the lack of influence earth's rotation there.

WTG simply diagnoses the large-scale convergence required to maintain a fixed vertical temperature profile, which is prescribed externally. The latter approach, WPG, also takes advantage of the small horizontal density variations in the tropical troposphere, but assumes that adjustment to this state takes place via the propagation of monochromatic gravity wave, which crude approximation of how the atmosphere responds to an anomalous burst of convection. Consider this sequence of events: A burst of convection in a column of atmosphere creates a local buoyancy anomaly, which causes the surrounding air to subside and warm. This creates a new buoyancy anomaly adjacent to the original one, and continuity requires the convecting column to rise and cool, removing the initial buoyancy anomaly. This propagating disturbance is a gravity wave. The details of this process are quite complicated in a fully-compressible, stratified atmosphere, and the emitted gravity waves can influence development and supression of convection itself. In WPG, we neglect these difficulties by assuming the emitted gravity wave has a single wavelength. In Chapter 2, we develop a new version of WPG analytically in the context of shallow water equations, and show how it can be extended to fully-compressible atmosphere.

In addition to encapsulating our understanding of how convection interacts with its environment, SDS schemes like WPG and WTG provide an attractive way to test convective parameterizations for global climate models. This type of application, and whether or not SDS schemes are reliable enough to be used in such a way, is discussed further in Chapter 3. With an SDS scheme coupled to a cloud-resolving model (CRM), we resolve the convective dynamics in a small patch of atmosphere, and parameterize the large-scale circulation normally resolved by a GCM. If we replace the CRM (which resolves convection) with a single-column of a GCM (with parameterized convection), we can directly test the reliability of the convective parameterization. Comparing observed divergence profiles and those produced by a single-column of a GCM coupled to the SDS scheme under the same conditions can tell us whether the convective parameterization is doing something reasonable.

How does moist convection, a fast and localized process, spread heat throughout the atmosphere, in order to balance the slow and relatively uniform radiative cooling of the atmosphere? In Chapter 4 we go beyond the simplistic understanding of tropical atmospheric dynamics encapsulated by WPG and WTG, and derive new analytical solutions which show how buoyancy anomalies spread throughout the tropical atmosphere. In general, the gravity waves excited by convection have a continuous spectrum of wavenumbers and frequencies, making analytical solutions difficult. In the past, authors have leveraged the fact that convection stops at the tropopause to greatly simplify the problem by assuming a rigid lid exists at the tropopause. With this assumption, the initial disturbance can be decomposed into a discrete set of normal modes, each with a corresponding wave speed. While this approach has been very useful for understanding basic elements of tropical atmospheric dynamics, including "steady-state" (e.g. Gill 1980) and transient responses (e.g. Matsuno

1966), it has some glaringly-unphysical consequences. For example, the discrete nature of the rigid-lid wave spectrum means an pulse of convection sets off a series of impossibly-sharp wavefronts propagating forever throughout the domain, each at a distinct wave speed. As more and more convection occurs, the energy in the domain grows without bound.

This problem arises because the rigid lid at the tropopause does not allow waves to propagate upward and out of the troposphere and relieve this unphysical build-up of energy. In Chapter 4, we derive analytic solutions for a pulse of buoyancy in an atmosphere without a rigid lid, and show that the upward radiation of wave energy out of the troposphere causes wavefronts to rapidly disperse. Buoyancy anomalies in an atmosphere without a rigid lid decay rapidly, with the longest waves in the tropical troposphere taking only about 10 days to radiate away.

Chapter 2

An Improved Weak Pressure Gradient Scheme for Single-Column Modeling[1]

A new formulation of the weak-pressure-gradient approximation (WPG) is introduced for parameterizing large-scale dynamics in limited-domain atmospheric models. This new WPG is developed in the context of the one-dimensional, linearized, damped shallow-water equations and then extended to Boussinesq and compressible fluids. Unlike previous supradomain-scale parameterizations, this formulation of WPG correctly reproduces both steady-state solutions and first-baroclinic gravity waves. In so doing, this scheme eliminates the undesirable gravity-wave resonance in previous versions of WPG. In addition, this scheme can be extended to accurately model the emission of gravity waves with arbitrary vertical wavenumber.

2.1 Introduction

In recent decades, single-column atmospheric models, including cloud-resolving models and single-column versions of global climate models, have come into widespread use as a means to develop and test new parameterizations for use in global climate models. To compare with observations, these limited-domain models are often forced with an observed profile of large-scale ascent (equivalently, a profile of large-scale convergence). This approach, however, has its drawbacks. For example, convergence profiles often contain significant errors, whether they come from observations (Mapes et al. 2003) or reanalysis (Roads et al. 1998). Additionally, forcing the model in this way neglects feedbacks on the large-scale circulation (Randall et al. 1996; Hack & Pedretti 2000) by unrealistically decoupling the large-scale vertical velocity from moist convection (Mapes 1997).

One way to solve these problems is to allow the model to specify its own convergence profile by parameterizing the large scale dynamics (Sobel & Bretherton 2000), a method dubbed 'supradomain-scale' (SDS) parameterization by Romps (2012b). On the most basic

---

[1] **Material in this chapter originally published in Edman & Romps (2014), © Copyright 2014 AMS.**

level, an SDS parameterization ingests environmental and modeled profiles of temperature and humidity and uses them to calculate the convergence profile, which is defined by the buoyancy of the column relative to its surroundings. Currently, there are two main paradigms for SDS parameterization, known as the weak-temperature-gradient approximation (WTG; e.g., Raymond & Zeng 2005), and the weak-pressure-gradient approximation (WPG; e.g., Romps 2012b). The premise of WTG is that vertical advection of potential temperature relaxes buoyancy differences between the column and the environment on some fixed timescale (Raymond & Zeng 2005; Sessions et al. 2010; Wang & Sobel 2012), while WPG relies on a parameterized form of the pressure-gradient force between the column and the environment to determine vertical velocity (Holton 1973; Nilsson & Emanuel 1999; Raymond & Zeng 2000; Kuang 2008; Blossey et al. 2009; Kuang 2011; Romps 2012b,a). Both schemes address the traditional problems listed above, but thus far neither approach has yielded an entirely satisfactory method for SDS parameterization.

Previous work has shown that prior implementations of WPG and WTG are inherently unable to adequately model steady-state and transient behavior in the same simulation; parameter values must be tuned depending on which is of interest (Romps 2012b). However, in numerical simulations, WPG appears to capture the dynamics of the full 3D atmosphere more realistically than WTG (Romps 2012a). In particular, a buoyancy perturbation in a column can trigger ascent both above and below the perturbation; this nonlocal ascent has the potential to trigger moist convection by removing a convective inhibition layer (Bretherton & Smolarkiewicz 1989; Mapes 1993). Romps (2012a) found that WPG was able to replicate this nonlocal behavior, while WTG can, by definition, only produce ascent at levels with positive buoyancy perturbations.

WPG introduces another difficulty, however. A column coupled to WPG behaves as if it were immersed in a bath of plane waves; for this reason, WPG is sometimes referred to as the damped-wave method (Kuang 2008; Wang et al. 2013). Around the frequency of these plane waves, a buoyancy anomaly in the column can trigger a resonance (with convection in phase with plane-wave-induced ascent) rather than the buoyancy anomaly simply damping away (as would occur by gravity-wave emission from the column in two or three dimensions). In general, this resonant behavior is undesirable for a scheme that seeks to parameterize the interaction between a single column's anomalous convection and its anomalous large-scale convergence.

In this paper, we seek to resolve these difficulties by deriving a modified version of WPG in the context of the 1D, linearized, damped, shallow-water equations. We do this for simplicity, but this does not limit the applicability of the results. The shallow-water equations can be thought of as representing an atmosphere that only permits one vertical mode; water layers of different depths approximate different vertical modes. To gain some intuition for this connection, we may think of the shallow-water system as representing the free troposphere: a source of mass in the shallow-water system corresponds to an injection of mass into the free troposphere from the boundary layer, which is associated with latent heating. Thanks to the mathematics relating the shallow-water equations to vertical modes of a stratified fluid, it is straightforward to extend the shallow-water results to the full atmosphere. Section 2.2

derives analytical solutions to a 1D shallow-water system. This information is then used in Section 2.3 to derive a new and improved set of WPG equations for the shallow-water system. Section 2.4 calculates – for the benchmark system, WTG, and the old and new WPG – the amplitude of the height anomaly driven by an oscillating source. Those solutions are compared for both inviscid and damped flow in Section 2.5, which demonstrates some advantages of the new WPG scheme over other SDS schemes. Section 2.6 extends the WPG scheme to a continuously stratified fluid. Section 2.7 concludes with some discussion.

2.2 Shallow-water equations

The goal of an SDS scheme is to accurately model the large-scale flow between an atmospheric column and its environment. A good SDS scheme will be able to do two things: 1. remove unforced virtual-temperature anomalies from the column on appropriate timescales (i.e., the timescales for gravity waves to exit the column), and 2. generate the correct virtual-temperature anomaly in the presence of a steady-state heating anomaly (where the virtual-temperature anomaly is made possible by a frictional drag on the flow). Both of these behaviors occur in the one-dimensional, linearized, damped, shallow-water equations. Because we can derive analytical solutions for this system, this is where we begin our analysis.

For a shallow-water system of depth D, source Q (units of m s^{-1}), and Rayleigh-damping timescale $1/\alpha$, the following equations govern a small height perturbation h and a small horizontal velocity u:

$$\partial_t h = -D\partial_x u + Q \tag{2.1}$$

$$\partial_t u = -g\partial_x h - \alpha u \,. \tag{2.2}$$

This system relates to the tropical free troposphere (where the Coriolis parameter can be approximated as zero) if we think of mapping h onto the mass of the free troposphere and Q onto the convective mass flux into the free troposphere. Using these equations, we wish to derive two timescales: 1. the transient timescale for unforced height anomalies to exit a column, and 2. the steady-state timescale that relates a column's steady-state height perturbation h to the applied steady-state forcing Q.

To begin, we must pick a "column" of the 1D shallow-water system that we will poke (with an initial height anomaly) and prod (with a steady-state mass source). Without any loss of generality, we choose our column as the region from $x = -L_1$ to $x = L_1$. For the transient case, this is all that we need to define. But, for the steady-state case with drag, we can only achieve a steady state if the source in the column is balanced elsewhere by a sink (i.e., there is no net source summed across the entire domain). In the absence of any drag (i.e., $\alpha = 0$), switching on a steady source in the column would generate two shock waves of h anomaly that would travel forever up and down the x axis, and the height anomaly in the column would hold steady. In the presence of drag, however, switching on a steady source in the column would cause the h anomaly in the column to grow *ad infinitum* as the pressure-gradient force tries to push the growing mass anomaly out to larger and larger distances against the countervailing drag force.

For this reason, we define a region of compensating mass sink of size L_2 to either side of the column. As depicted in Figure 2.1, the source Q in the column of size $2L_1$ is balanced by an equal and opposite source $-QL_1/L_2$ in the wings of combined size $2L_2$. As shown below, the choice of L_2 has a negligible impact on the evolution of transients, but it plays a crucial role in defining the magnitude of height anomalies in the presence of a steady-state forcing. What sets L_2? While it is plausible that L_2 may be comparable to the dissipative scale $\sqrt{gD}/\alpha$ (i.e., the product of the wave speed and the damping timescale), we deem it equally plausible that L_2 is set, in reality, by the dissipative effects of the convective response to the passing wave. In this latter scenario, anomalous convection in some column would generate a transient heating of its surroundings by the emitted gravity waves. This transient heating may inhibit convection, leading to an anomalous cooling that damps the wave. If that transient warming is sufficiently efficient at inhibiting convection, then this damping via convective deficit could serve as a sink for the gravity waves well before the waves extend to the dissipative scale. We do not attempt to resolve this difficult issue here. Instead, we simply leave L_2 as a free parameter and leave its determination to future work.

2.2.1 Transients

In the study of transients, we will assume that the timescale for inviscid gravity waves to exit the column ($L_1/\sqrt{gD}$) is much smaller than the Rayleigh damping timescale ($1/\alpha$). Therefore, we can safely set $\alpha = 0$. Taking ∂_t of (2.1) and $-D\partial_x$ of (2.2) and adding the results, we find an inhomogeneous wave equation for h:

$$\partial_t^2 h - gD\partial_x^2 h = \partial_t Q \,. \tag{2.3}$$

The solution to (2.3) for an arbitrary source Q is given by

$$h(x,t) \;=\; \frac{1}{2}\int\limits_{-\infty}^{t} dt' \left\{ Q\Big[x + c(t-t'), t'\Big] + Q\Big[x - c(t-t'), t'\Big]\right\} , \tag{2.4}$$

where $c = \sqrt{gD}$ is the wave speed. Thus, for an initial pulse $Q(x,t) = Q_0(x)\delta(t)$, $h(x,t)$ is given by two waves of the same shape as Q_0, traveling to the left and right with speed c.

Consider a system with zero h for time $t < 0$ that is given an instantaneous jolt at $t = 0$ defined by the source

$$Q(x,t) \;=\; \left(1+\frac{L_1}{L_2}\right) h_0\delta(t)\mathcal{H}(L_1-x)\mathcal{H}(L_1+x) - \frac{L_1}{L_2}h_0\delta(t)\Big[\mathcal{H}(L_1+L_2-x)\mathcal{H}(L_1+L_2+x)\Big] ,$$

where $\mathcal{H}$ is the Heaviside unit step function. This generates $h(x)$ of the same shape as that depicted in Figure 2.1, with an initial amplitude in the column of $h = h_0$. The solution, from equation (2.4), is

$$h(x,t) \;=\; h_+(x,t) + h_-(x,t) \,,$$

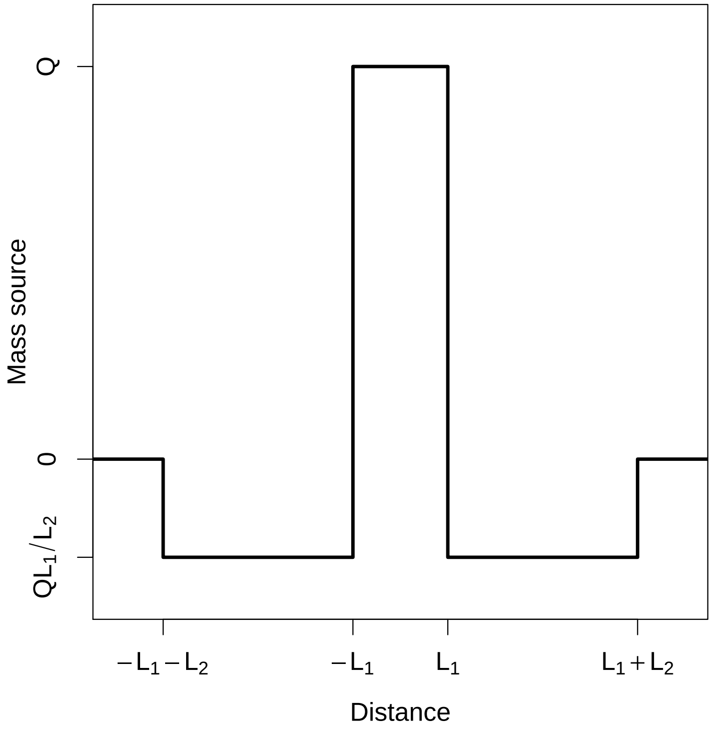

Figure 2.1: The setup of the 1D shallow-water forcings. The forcing Q in the column of size $2L_1$ is balanced by an equal and opposite forcing of $-QL_1/L_2$ in the wings of combined size $2L_2$.

where

$$\begin{aligned} h_\pm(x,t) \;=\; & \left(1+\frac{L_1}{L_2}\right)\frac{h_0}{2}\mathcal{H}(L_1-x\pm ct)\mathcal{H}(L_1+x\mp ct) \\ & -\frac{L_1}{L_2}\frac{h_0}{2}\mathcal{H}(L_1+L_2-x\pm ct)\mathcal{H}(L_1+L_2+x\mp ct)\,. \end{aligned}$$

This solution is just the sum of top-hat pulses traveling in the negative (h_-) and positive (h_+) directions from the source and sink regions at speed c. The timescale for the entire disturbance to propagate out of the column (defined as $-L_1 < x < L_1$) is on the order of $(L_1+L_2)/c$. If L_2 is comparable in size to L_1, then this timescale is of order L_1/c. On the other hand, if we assume that the compensating regions are much larger than the width of the column (i.e. $L_2 \gg L_1$), then the amplitude of the disturbance from the compensating regions is small relative to the disturbance from the column. In this case, we can safely ignore this secondary disturbance from the compensating regions, and the timescale for transients to propagate out of the column is still

$$\tau \;=\; \frac{L_1}{c} \qquad \text{(transient timescale)}\,. \tag{2.5}$$

2.2.2 Steady state

For the steady state case, we consider a Q of the same shape as in Figure 2.1,

$$Q(x,t) \;=\; \left(1+\frac{L_1}{L_2}\right) Q_0 \mathcal{H}(L_1-x)\mathcal{H}(L_1+x) - \frac{L_1}{L_2} Q_0 \mathcal{H}(L_1+L_2-x)\mathcal{H}(L_1+L_2+x)\,.$$

Assuming a positive α, the steady-state solution to equations (2.1) and (2.2) is

$$u(x) \;=\; \begin{cases} \dfrac{Q_0}{D}x & |x| \leq L_1 \\ \dfrac{Q_0 L_1}{D L_2}\operatorname{sign}(x)\Big(L_1+L_2-|x|\Big) & L_1 < |x| < L_1+L_2 \\ 0 & L_1+L_2 \leq |x| \end{cases} \tag{2.6}$$

and

$$h(x) \;=\; \begin{cases} \dfrac{\alpha Q_0}{2c^2}\Big[L_1(L_1+L_2)-x^2\Big] & |x| \leq L_1 \\ \dfrac{\alpha Q_0 L_1}{2c^2 L_2}\Big(L_1+L_2-|x|\Big)^2 & L_1 < |x| < L_1+L_2 \\ 0 & L_1+L_2 \leq |x| \end{cases} . \tag{2.7}$$

This solution is shown in Figure 2.2. By averaging over the column ($x \in [-L_1, L_1]$), we see that the mean steady-state height anomaly is

$$\frac{1}{2L_1}\int_{-L_1}^{L_1} dx\, h(x) \;=\; \frac{\alpha}{c^2} L_1^2 \left(\frac{1}{3}+\frac{1}{2}\frac{L_2}{L_1}\right) Q_0\,. \tag{2.8}$$

This equation for the mean height anomaly is of the form τQ_0, where τ is a timescale relating the source Q_0 to the mean steady-state height anomaly in the column. Therefore, we see that this timescale is

$$\tau \;=\; \frac{\alpha L_1^2}{c^2}\left(\frac{1}{3}+\frac{1}{2}\frac{L_2}{L_1}\right) \qquad \text{(steady-state timescale)}\,. \tag{2.9}$$

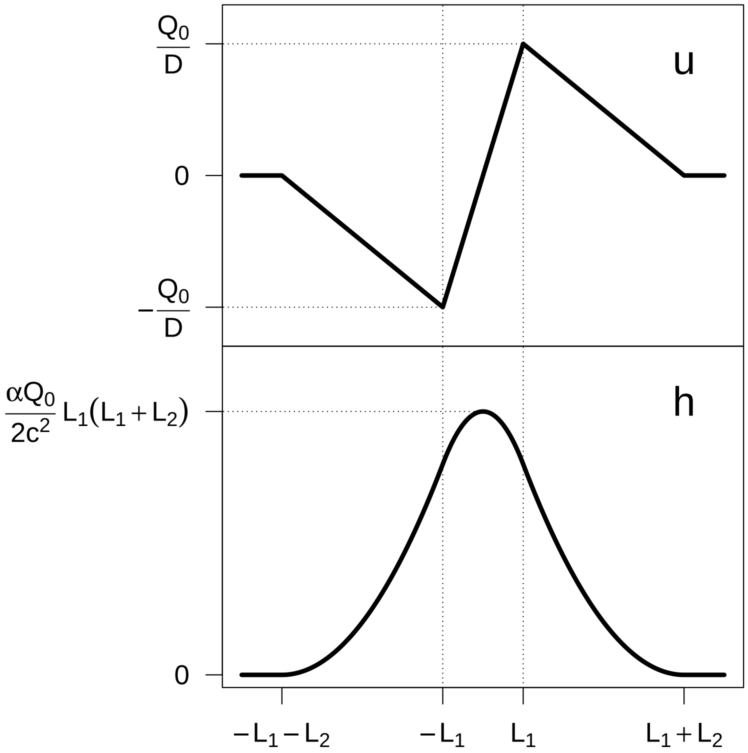

Figure 2.2: The steady-state solution corresponding to equations (2.6) and (2.7).

2.3 New WPG

WPG reduces equations (2.1) and (2.2) to an equation for the evolution of h in a single column embedded in a quiescent environment. The first step in deriving the WPG version of these equations is to take the divergence of (2.2). Next, we approximate the resulting pressure-gradient term $-\partial_x^2 h$ by $\frac{h}{L^2}$, where L represents the distance over which the height anomaly (equivalently, the pressure anomaly) relaxes to zero; the precise value of L will be determined below. Finally, we replace α with the to-be-determined constant α^*. This yields the standard WPG equations,

$$\partial_t h = -D\delta + Q \tag{2.10}$$

$$\partial_t \delta = \frac{gh}{L^2} - \alpha^* \delta \,, \tag{2.11}$$

where $\delta = \partial_x u$ is the divergence. As shown by Romps (2012b), this set of equations is unable to capture simultaneously both the transient and steady-state timescales. Here, we will add a term to the WPG equations in the hope of ameliorating this situation.

The fundamental problem with the WPG equations is that, in the inviscid limit ($\alpha \to 0$), they describe an oscillating system instead of a damped system. If we think of WPG as describing a column immersed in a quiescent environment, then perturbations in the column should exit the column on a gravity-wave propagation timescale, causing the perturbation in the column to damp towards zero. Instead, initial perturbations in the WPG system lead to oscillations: in the case of an unforced and inviscid fluid ($Q = \alpha = 0$), equations (2.10) and (2.11) give $\partial_t^2 h = -(c/L)^2 h$. This describes a normal mode with period $2\pi L/c$ instead of decay towards zero on a timescale of L/c.

Which of the equations (2.10) and (2.11) is responsible for this bad behavior? Equation (2.10) can not be at fault, for it enforces a simple and irrefutable statement of mass conservation for the column. Equation (2.11), on the other hand, is not as ironclad. Its weak point is the approximation

$$-\overline{\partial_x^2 p} \;\approx\; \frac{g}{L^2}\overline{h}\,, \tag{2.12}$$

where a bar denotes an average over $x \in [-L_1, L_1]$. This equation can be written as

$$-\frac{g}{L_1}\,\partial_x h|_{-L_1}^{L_1} \;\approx\; \frac{g}{L^2}\overline{h}\,.$$

In other words, it assumes that the height gradients at the boundaries of the column are proportional to the mean height perturbation in the column. For a transient height anomaly, however, this is not the case. Consider $\delta = 0$ and $h = h_0 \exp(-x^2/L_1^2)$ at time $t = 0$. Taking $Q = \alpha = 0$, this height perturbation evolves as two counter-propagating Gaussian disturbances: one has velocity c, the other has velocity $-c$, and both have an amplitude of $h_0/2$. This is depicted in Figure 2.3. For $t < L_1/c$, the mean height anomaly in the column is positive and the pressure-gradient force (which is proportional to the height gradient in the shallow water model) at $x = \pm L_1$ is accelerating fluid out of the column. For $t > L_1/c$, however, the mean height anomaly is still positive, but the pressure-gradient force has switched signs, and is now accelerating fluid into the column. This example illuminates a key piece of physics missing from the approximation in equation (2.12): the back-reaction caused by the column's modification of its immediate environment. Height anomalies initially within the column at time t are just outside the column at time $t + L_1/c$. In this transient case, the difference in height anomalies between the column and its immediate environment is not $\overline{h}(t)$, as assumed in previous implementations of WPG, but is, instead, something akin to $\overline{h}(t) - \overline{h}(t - L_1/c) \approx (L_1/c)\partial_t\overline{h}$. This suggests that a term similar to $(L_1/c)\partial_t\overline{h}$ might belong on the right-hand side of equation (2.11).

Note that the h term on the right-hand side of (2.11) cannot be entirely replaced by a $\partial_t h$ term because the former is needed to make steady-state solutions possible in the presence of a constant, nonzero Q. Therefore, we explore the consequences of adding the term $(L/c)\partial_t\overline{h}$, multiplied by g/L^2 and a to-be-determined dimensionless number β, to the right-hand side of the divergence equation. This gives

$$\partial_t h \;=\; -D\delta + Q \tag{2.13}$$

$$\partial_t \delta \;=\; \frac{gh}{L^2} + \frac{\beta g}{Lc}\partial_t h - \alpha^* \delta\,. \tag{2.14}$$

In order to put equation (2.14) in a form more easily integrated, we define a new variable δ' related to δ and h as

$$\delta' \; = \; \frac{\delta - \beta g h / cL}{1 - \beta \alpha^* L / c} \, .$$

Expression (2.14) benefits from a cancellation of terms when written in terms of δ'. The resulting equations are

$$\partial_t h \; = \; -D\delta + Q \tag{2.15}$$

$$\partial_t \delta' \; = \; \frac{gh}{L^2} - \alpha^* \delta' \tag{2.16}$$

$$\delta \; = \; \delta' + \frac{\beta L}{c} \partial_t \delta' \, . \tag{2.17}$$

Here, equation (2.16) is a prognostic equation for δ', and equation (2.17) is a diagnostic equation giving δ – the actual divergence – in terms of δ' and its derivative.

To find the correct values for β, L, and α^*, we reduce these equations to a single equation for h and study its steady-state and transient behaviors. The equations reduce to

$$\partial_t^2 h + (\alpha^* + \beta c/L)\partial_t h + \frac{c^2}{L^2} h \; = \; \partial_t Q + \alpha^* Q \, . \tag{2.18}$$

For transient cases with $Q = 0$, a test solution of $h = e^{\omega t}$ gives a dispersion relation of

$$\omega \; = \; -\left(\frac{\alpha^*}{2} + \frac{\beta c}{2L}\right) \pm \sqrt{\left(\frac{\alpha^*}{2} + \frac{\beta c}{2L}\right)^2 - \frac{c^2}{L^2}} \, . \tag{2.19}$$

As discussed in Section 2.2.1, transients should exit the column on a timescale of L_1/c in the inviscid limit. This is achieved by selecting

$$\beta \; = \; 2 \tag{2.20}$$

$$L \; = \; L_1 \, , \tag{2.21}$$

which, in the inviscid limit, reduces (2.19) to $\omega = -c/L_1$. For a steady-state case with constant Q, the solution to (2.18) is $h = (\alpha^* L^2/c^2)Q$, which yields the timescale found in Section 2.2.2 if we choose

$$\alpha^* \; = \; \alpha \left(\frac{1}{3} + \frac{1}{2}\frac{L_2}{L_1}\right) \, . \tag{2.22}$$

For the old WPG, $\beta = 0$ in (2.18), so there is no way to simultaneously capture the transient timescale and the steady-state timescale. Selecting $L = L_1$, we have two choices for α^* in the old WPG. If we match the transient timescale, then

$$\alpha^* \; = \; 2c/L_1 \, .$$

We will call this “version 1” of the old WPG. If we match the steady-state timescale, then we must choose α^* as defined by equation (2.22). We will call this “version 2” of the old WPG.

WTG is similarly unable to capture both the transient and steady-state time scales. In the relaxed form of WTG (e.g., Raymond & Zeng 2005), equation (2.1) is approximated by

$$\delta \;=\; \frac{h}{D\tau}\,, \tag{2.23}$$

where τ is the timescale over which height differences between the column and the environment are removed. If we match the transient time scale (i.e. the time for a gravity wave to propagate out of the column), then

$$\tau \;=\; \frac{L_1}{c}\,.$$

This is the form of τ most commonly used in the literature (e.g., Raymond & Zeng 2005; Sessions et al. 2010; Wang & Sobel 2011); we will call this "version 1" of WTG. An alternative, but potentially interesting choice is to match the steady-state timescale, which gives

$$\tau \;=\; \frac{\alpha^* L_1^2}{c^2}\,.$$

We will call this "version 2" of WTG. The equations for all five SDS schemes are listed in Table 2.1.

2.4 Solutions to an oscillating source

Although we have shown that WPG can match the full 1D solution for inviscid transient and steady state cases, so far we have not demonstrated how WPG performs for cases which do not fit neatly into either of these categories. To explore solutions that lie somewhere between inviscid transients and damped steady states, we calculate here solutions to an oscillating mass source. These solutions are compared against each other in Section 2.5.

2.4.1 Benchmark

Consider a source of the shape depicted in Figure 2.1 that oscillates in time with angular frequency ω,

$$\begin{aligned} Q(x,t) \;=\; & \left(1+\frac{L_1}{L_2}\right) Q_0 \cos(\omega t)\mathcal{H}(L_1-x)\mathcal{H}(L_1+x) \\ & - \frac{L_1}{L_2} Q_0 \cos(\omega t)\mathcal{H}(L_1+L_2-x)\mathcal{H}(L_1+L_2+x)\,. \end{aligned} \tag{2.24}$$

In Appendix B.1, we derive the solution generated by this forcing for the case of the inviscid (i.e., $\alpha = 0$) shallow-water equations. In this inviscid case, the average height anomaly over

SDS scheme	Equations for δ
New WPG	$\partial_t\delta' = \dfrac{gh}{L_1^2} - \alpha\left(\dfrac{1}{3} + \dfrac{1}{2}\dfrac{L_2}{L_1}\right)\delta'$ $\delta = \delta' + \dfrac{2L_1}{c}\partial_t\delta'$
Old WPG v1	$\partial_t\delta = \dfrac{gh}{L_1^2} - \dfrac{2c}{L_1}\delta$
Old WPG v2	$\partial_t\delta = \dfrac{gh}{L_1^2} - \alpha\left(\dfrac{1}{3} + \dfrac{1}{2}\dfrac{L_2}{L_1}\right)\delta$
WTG v1	$\delta = \dfrac{gh}{L_1 c}$
WTG v2	$\delta = \dfrac{gh}{\alpha L_1^2}\left(\dfrac{1}{3} + \dfrac{1}{2}\dfrac{L_2}{L_1}\right)^{-1}$

Table 2.1: Definitions of the horizontal divergence δ in the five supradomain-scale schemes in the context of the damped shallow-water equations with damping rate α, column of width $2L_1$, and compensating regions of net width $2L_2$. Here, g is the gravitational acceleration, $c = \sqrt{gD}$ is the wave speed, and h is the mean height anomaly in the column.

the column is $\bar{h}(t) = h_0 \cos(\omega t + \phi)$, where the amplitude h_0 is

$$\begin{aligned} h_0^{\text{benchmark}} &= \frac{Q_0}{\omega}\Bigg\{\left[\frac{c}{\omega L_1}\sin\left(\frac{\omega L_1}{c}\right)\left[\left(1+\frac{L_1}{L_2}\right)\sin\left(\frac{\omega L_1}{c}\right)-\frac{L_1}{L_2}\sin\left(\frac{\omega(L_1+L_2)}{c}\right)\right]\right]^2 \\ &\quad +\left[-1+\frac{c}{\omega L_1}\sin\left(\frac{\omega L_1}{c}\right)\left[\left(1+\frac{L_1}{L_2}\right)\cos\left(\frac{\omega L_1}{c}\right)-\frac{L_1}{L_2}\cos\left(\frac{\omega(L_1+L_2)}{c}\right)\right]\right]^2\Bigg\}^{1/2} \end{aligned} \tag{2.25}$$

In the presence of damping ($\alpha > 0$), an analytical solution is not possible, so the damped shallow-water equations are integrated numerically to obtain the value of h_0.

2.4.2 New WPG

In the column, equation (2.24) takes the form $Q(t) = Q_0 \cos(\omega t)$. Therefore, to find the corresponding solution from the new WPG scheme, we substitute $Q = Q_0 e^{i\omega t}$, with ω and Q_0 both real, into (2.18) with the values of β, L, and α^* given by equations (2.20–2.22). We then seek a solution of the form $h = h_0 e^{i\omega t + i\phi}$ for real constants h_0 and ϕ. The resulting dispersion relation for ω is

$$-\omega^2 h_0 + (\alpha^* + 2c/L_1)i\omega h_0 + (c^2/L_1^2)h_0 = (i\omega + \alpha^*)Q_0 e^{-i\phi}$$

For brevity, the α^* notation is retained here, although its value is given by equation (2.22). Solving for h_0, we obtain

$$h_0^{\text{WPG,new}} = \sqrt{\frac{\omega^2 + \alpha^{*2}}{(c^2/L_1^2 - \omega^2)^2 + (\alpha^* + 2c/L_1)^2\omega^2}}\, Q_0 \,. \tag{2.26}$$

2.4.3 Old WPG, version 1

The amplitude for version 1 of the old WPG, which is tuned to match the transient timescale, is obtained by setting β to zero in (2.18) and setting $L = L_1$ and $\alpha^* = 2c/L_1$, which gives the dispersion relation

$$-\omega^2 h_0 + (2c/L_1)i\omega h_0 + (c^2/L_1^2)h_0 = (i\omega + 2c/L_1)Q_0 e^{-i\phi} \,.$$

Solving for h_0, we obtain

$$h_0^{\text{WPG,old,v1}} = \frac{\sqrt{\omega^2 + (2c/L_1)^2}}{\omega^2 + (c/L_1)^2}\, Q_0 \,. \tag{2.27}$$

2.4.4 Old WPG, version 2

The amplitude for version 2 of the old WPG, which is tuned to match the steady-state timescale, is obtained by setting β to zero in (2.18) and using the same values for L and α^* used by the new WPG. This gives the dispersion relation

$$-\omega^2 h_0 + \alpha^* i\omega h_0 + (c^2/L_1^2)h_0 = (i\omega + \alpha^*)Q_0 e^{-i\phi}\,.$$

Solving for h_0, we obtain

$$h_0^{\mathrm{WPG,old,v2}} \;=\; \sqrt{\frac{\omega^2+\alpha^{*2}}{(c^2/L_1^2-\omega^2)^2+\alpha^{*2}\omega^2}}\,Q_0\,. \tag{2.28}$$

2.4.5 WTG, version 1

For version 1 of WTG, the dispersion relation is

$$i\omega h_0 = -ch_0/L_1 + Q_0 e^{-i\phi}\,,$$

which gives

$$h_0^{\mathrm{WTG,v1}} \;=\; \frac{Q_0}{\sqrt{\omega^2+c^2/L_1^2}}\,. \tag{2.29}$$

2.4.6 WTG, version 2

For version 2 of WTG, the dispersion relation is

$$i\omega h_0 = -\frac{c^2 h_0}{\alpha^* L_1^2} + Q_0 e^{-i\phi}\,,$$

which gives

$$h_0^{\mathrm{WTG,v2}} \;=\; \frac{Q_0}{\sqrt{\omega^2+\frac{c^4}{\alpha^{*2}L_1^4}}}\,. \tag{2.30}$$

2.5 Comparison of oscillating solutions

To facilitate a comparison of these amplitudes, let us non-dimensionalize the equations with respect to the gravity-wave timescale L_1/c. Introducing non-dimensional variables denoted by a tilde,

$$\begin{aligned}\tilde{h_0} &= \frac{c}{L_1 Q_0}h_0\\ \tilde{\omega} &= \omega L_1/c\\ \tilde{\alpha} &= \alpha L_1/c\\ \tilde{\alpha^*} &= \alpha^* L_1/c\,,\end{aligned}$$

the amplitudes become

$$\begin{aligned}
\tilde{h}_0^{\text{benchmark}} &= \frac{1}{\tilde{\omega}^2}\Bigg\{\Bigg[\sin(\tilde{\omega})\Big[(1+r)\sin(\tilde{\omega}) - r\sin(\tilde{\omega}+\tilde{\omega}/r)\Big)\Big]\Bigg]^2 \\
&\quad + \Bigg[-\tilde{\omega} + \sin(\tilde{\omega})\Big[(1+r)\cos(\tilde{\omega}) - r\cos(\tilde{\omega}+\tilde{\omega}/r)\Big]\Bigg]^2\Bigg\}^{1/2} && (2.31) \\
\tilde{h}_0^{\text{WPG,new}} &= \sqrt{\frac{\tilde{\omega}^2+\tilde{\alpha}^{*2}}{(1-\tilde{\omega}^2)^2+(\tilde{\alpha}^*+2)^2\tilde{\omega}^2}} && (2.32) \\
\tilde{h}_0^{\text{WPG,old,v1}} &= \frac{\sqrt{\tilde{\omega}^2+4}}{\tilde{\omega}^2+1} && (2.33) \\
\tilde{h}_0^{\text{WPG,old,v2}} &= \sqrt{\frac{\tilde{\omega}^2+\tilde{\alpha}^{*2}}{(1-\tilde{\omega}^2)^2+\tilde{\alpha}^{*2}\tilde{\omega}^2}} && (2.34) \\
\tilde{h}_0^{\text{WTG,v1}} &= \frac{1}{\sqrt{\tilde{\omega}^2+1}} && (2.35) \\
\tilde{h}_0^{\text{WTG,v2}} &= \frac{1}{\sqrt{\tilde{\omega}^2+1/\tilde{\alpha}^{*2}}}\,, && (2.36)
\end{aligned}$$

where

$$r \equiv L_1/L_2\,.$$

Recall that equation (2.31) is for inviscid flow only, while the other equations are for general damping. In Section 2.5.3, numerical simulations of the damped shallow-water equations will be used instead of equation (2.31).

2.5.1 Inviscid oscillations for large and small $\tilde{\omega}$

For $\tilde{\omega} \gg 1$, the mass added to the column during the positive phase of Q does not propagate significantly out of the column before it is removed by the negative phase of Q. Therefore, the amplitude h_0 is simply equal to $\int_0^{\pi/2} dt\, Q_0 \cos(\omega t)$, which gives $\tilde{h}_0 = 1/\tilde{\omega}$. The benchmark solution and all of the WPG and WTG schemes give this behavior, which can be confirmed by taking the large-$\tilde{\omega}$ limit of equations (2.31–2.36).

For $\tilde{\omega} \ll 1$, not all of the SDS parameterizations are equivalent, even in the inviscid case.

In the limit of $\tilde{\omega} \to 0$ for inviscid flow, the amplitudes are

$$\tilde{h}_0^{\text{benchmark}} = \left(\frac{1}{3} + \frac{1}{2}\frac{L_2}{L_1}\right)\tilde{\omega} \tag{2.37}$$

$$\tilde{h}_0^{\text{WPG,new}} = \tilde{\omega} \tag{2.38}$$

$$\tilde{h}_0^{\text{WPG,old,v1}} = 2 \tag{2.39}$$

$$\tilde{h}_0^{\text{WPG,old,v2}} = \tilde{\omega} \tag{2.40}$$

$$\tilde{h}_0^{\text{WTG,v1}} = 1 \tag{2.41}$$

$$\tilde{h}_0^{\text{WTG,v2}} = 0\,. \tag{2.42}$$

Note that the benchmark amplitude scales as $\tilde{\omega}$ in the small-$\tilde{\omega}$ limit. This is caused by gravity waves from the adjacent sink regions that propagate into the column. For $\tilde{\omega} = 0$, the solution is simply an inviscid steady state; without any Rayleigh damping, no pressure gradient (i.e., no h gradient) is needed to drive the flow, so $\tilde{h}_0 = 0$. Therefore, the $\tilde{h}_0 \sim \tilde{\omega}$ scaling reflects the approach to an inviscid steady state as $\tilde{\omega}$ is decreased towards zero.

Both the new WPG and version 2 of the old WPG capture the $\tilde{h}_0 \sim \tilde{\omega}$ scaling. An important difference, however, is that these schemes miss the $(1/3 + L_2/2L_1)$ factor in that scaling relationship. In the benchmark simulations, this dependence on L_2 is caused by the fact that a larger sink region (i.e., larger L_2) requires a longer time for the peak of the sink signal to reach the column. This allows the height anomaly in the column to reach a larger amplitude before it is quenched by gravity waves from the sink regions. Since neither the new WPG scheme nor version 2 of the old WPG scheme know anything about L_2 in the absence of damping, it is not possible for them to capture this effect. The other schemes – version 1 of the old WPG and both WTG schemes – are unable to capture any $\tilde{h}_0 \sim \tilde{\omega}$ scaling in the small-frequency limit.

2.5.2 Inviscid oscillations for all $\tilde{\omega}$

For one-dimensional, inviscid, shallow water, an oscillating source $Q(x,t)$ of the form (2.24) gives rise to height oscillations in the column with an amplitude given by (2.31). In the column, this source simplifies to $Q(t) = Q_0 \cos(\omega t)$. When subjected to this $Q(t)$ under the assumption of inviscid flow (i.e., $\alpha = 0$), the five SDS schemes produce height oscillations with amplitudes given by equations (2.32–2.36) with $\tilde{\alpha}^* = \tilde{\alpha} = 0$.

These amplitudes are plotted as a function of $\tilde{\omega}$ in Figure 2.4 for the case of $L_1/L_2 = 1$. The black curve gives the benchmark solution. The green and blue curves correspond to WTG and the old WPG; solid and dashed curves correspond to version 1 and version 2. The red curve plots the solution from the new WPG scheme. Note that WTG version 2 (the dashed green curve) does not appear on this plot because its h_0 is identically zero when $\tilde{\alpha}^* = 0$. With that exception, all the other schemes do well at matching the benchmark amplitude for large $\tilde{\omega}$. As discussed in the previous section, this agreement at large $\tilde{\omega}$ is a trivial consequence of the forcing period being much smaller than the gravity-wave propagation time.

At small $\tilde{\omega}$, the behavior is described by equations (2.37–2.42). The new WPG scheme and version 2 of the old WPG scheme scale their amplitude in proportion to $\tilde{\omega}$ like the benchmark solution, but offset by an overall factor of $1/3 + L_2/2L_1$. The other schemes do poorly in the small-$\tilde{\omega}$ limit.

For $\tilde{\omega} = 1$, versions 2 of WTG and old WPG are both highly discrepant with each other and the benchmark solution: the benchmark has $\tilde{h}_0 \sim 1$, WTG version 2 has $\tilde{h}_0 = 0$, and old WPG version 2 has $\tilde{h}_0 = \infty$. As mentioned above, version 2 of WTG is identically zero for all $\tilde{\omega}$ because it is designed to move height anomalies out of the column on a timescale proportional to α, which is zero in the inviscid limit. Version 2 of the old WPG has a resonance at $\tilde{\omega} = 1$, which manifests itself as an infinite $\tilde{h}_0$ at that frequency. This resonance occurs because that scheme interprets any height anomaly in the column as a consequence of the column sitting in an infinite plane wave of height anomalies with frequency L_1/c. An oscillatory forcing at this frequency is interpreted by this scheme as an amplification of the plane-wave amplitude.

2.5.3 Damped oscillations

To evaluate the WTG and WPG schemes in the presence of damping ($\alpha > 0$), the benchmark solutions must be simulated numerically. The amplitudes obtained from these numerical simulations are plotted as black circles in Figure 2.5, which gives the amplitudes $\tilde{h}_0$ for a range of $\tilde{\omega}$, $\tilde{\alpha}$, and L_1/L_2. The colors and line styles (solid versus dashed) are the same as in Figure 2.4. From left to right, the columns range from $\tilde{\alpha} = 0.1$ to 0.001. From top to bottom, the rows range from $L_1/L_2 = 1$ to 0.01. Each plot depicts $\log_{10} \tilde{h}_0$ as a function of $\log_{10} \tilde{\omega}$, with the abscissa ranging from $\tilde{\omega} = 10^{-4}$ to 10.

The choices of $\tilde{\alpha}$, $\tilde{\omega}$, and L_1/L_2 depicted here are motivated by the following considerations. Imagine that the column (i.e., the region from $-L_1$ to L_1) represents a patch of atmosphere comparable in size to a GCM grid column, i.e., with a width on the order of 100 km. For $L_1/L_2 = 1$, any convective anomaly in the column is compensated for by a convective anomaly of comparable magnitude, but opposite sign, in the adjacent grid cells. On the other hand, it is unlikely that that the compensating region would be significantly smaller than one grid cell, so we consider $L_1/L_2 = 1$ as the upper limit for this ratio. At the lower limit, we consider $L_1/L_2 = 0.01$, which implies a compensating region on the order of 10,000 km. Since this is already comparable to the circumference of the Earth, we take this as the lower limit of L_1/L_2.

A plausible constraint on $\tilde{\omega}$ can be obtained by requiring that gravity waves are able to communicate signals across the compensating region on a timescale short compared to one period of the oscillation; otherwise, the contemporaneous oscillations of the source and sink regions would be acausal. Multiplying the gravity-wave speed (c) by the timescale of the oscillation ($1/\omega$) and requiring it to be larger than L_2, we obtain $c/\omega > L_2$, which can be rewritten as $\tilde{\omega} < L_1/L_2$. In Figure 2.5, this region is occupied by $\log_{10} \tilde{\omega} < 0$ in the top row, < -1 in the middle row, and < -2 in the bottom row. Further consideration of causality leads us to conclude that the maximum size of the sink region, L_2, cannot exceed the dissipative scale c/α (i.e. the length scale over which gravity waves are dissipated by Rayleigh damping). This implies that we should restrict our attention to $\tilde{\alpha} \leq L_1/L_2$. For α, a range of $\tilde{\alpha}$ from 0.1 to 0.001 with $c = 50$ m s^{-1} and $L_1 = 100$ km corresponds to a range of $1/\alpha$ from 0.2 days to 20 days. As shown by Romps (2013), moist convection can generate a damping timescale in the range of 1–10 days, although the precise timescale depends on the convective mass flux and the baroclinicity of the circulation.

Note that versions 1 of WTG and old WPG give the same curves for $\tilde{h}_0$ in all panels of Figure 2.5. This is caused by the fact that the amplitudes in equations (2.33) and (2.35) do not depend on either L_2 or α. As in the inviscid case, their amplitudes plateau at small $\tilde{\omega}$, resulting in poor behavior there. Version 2 of WTG is increasingly bad as $\tilde{\alpha}$ decreases, with the amplitude going to zero in the inviscid limit. Version 2 of the old WPG scheme continues to exhibit a resonance at $\tilde{\omega} = 1$, although the addition of damping prevents the amplitude from going to infinity. The new WPG scheme performs very well when L_1 and L_2 are of the same order of magnitude, as shown by the excellent agreement between the black and red curves in the top row of Figure 2.5. At smaller L_1/L_2 ratios, the new WPG scheme performs well at small frequencies ($\tilde{\omega} \ll 1$, where steady state prevails, and so versions 2 of WTG and WPG also perform well) and around one and larger frequencies ($\tilde{\omega} \gtrsim 1$, where transients dominate, and so versions 1 of WTG and WPG also perform well). In these respects, the new WPG combines the best aspects of previous SDS schemes. Where the new WPG is most deficient is for $\tilde{\omega} \sim 0.01$ for the smallest $\tilde{\alpha}$ (0.001) and the smallest L_1/L_2 (0.01). For that combination of $\tilde{\omega}$, $\tilde{\alpha}$, and L_1/L_2, the frequency is large compared to the damping, making the flow practically inviscid. Since L_2 is large compared to L_1, comparison of equations (2.37) and (2.38) correctly predicts that the new WPG scheme will underestimate the amplitude by a factor of $L_2/2L_1 = 50$.

2.6 Extension to continuously stratified fluids

Given an SDS scheme for the shallow-water equations, it is straightforward to extend it to a continuously stratified fluid. Consider the linearized, Rayleigh-damped, hydrostatic, Boussinesq equations, described by

$$\partial_t u = -\frac{1}{\rho}\partial_x p - \alpha u \tag{2.43}$$

$$\partial_t v = -\frac{1}{\rho}\partial_y p - \alpha v \tag{2.44}$$

$$0 = b - \frac{1}{\rho}\partial_z p \tag{2.45}$$

$$\partial_t b = -N^2 w + Q \tag{2.46}$$

$$\partial_x u + \partial_y v + \partial_z w = 0\,, \tag{2.47}$$

where b is the buoyancy (m s^{-2}), p is the perturbation pressure (Pa), and Q is the buoyancy source (m s^{-3}). These equations can be combined to give a self-contained equation for B:

$$\partial_t^2 \partial_z^2 b + \alpha \partial_t \partial_z^2 b + N^2 \nabla^2 b \;=\; \partial_t \partial_z^2 Q + \alpha \partial_z^2 Q\,. \tag{2.48}$$

For consistency with the one-dimensional shallow-water equations studied in the previous sections, let us drop the y dimension (or, equivalently, consider solutions that are invariant in the y direction). Then, one-dimensional transient waves in an inviscid fluid obey

$$\partial_t^2 \partial_z^2 b + N^2 \partial_x^2 b \;=\; 0\,.$$

For buoyancy patterns with a vertical wavenumber m, i.e., $b(x,z,t) = b(x,t)\sin(mz)$, this is a wave equation with phase speed N/m. Therefore, the transient timescale for these buoyancy patterns is

$$\tau \;=\; \frac{L_1 m}{N} \qquad \text{(transient timescale)}\,. \tag{2.49}$$

Next, consider a steady state, which reduces (2.48) to

$$N^2 \partial_x^2 b \;=\; \alpha \partial_z^2 Q\,. \tag{2.50}$$

For a heating of wavenumber m with compensating regions as depicted in Figure 2.1, Q takes the form

$$\begin{aligned} Q(x,z) \;=\; & \left(1+\frac{L_1}{L_2}\right) Q_0 \sin(mz)\mathcal{H}(L_1 - x)\mathcal{H}(L_1 + x) \\ & \qquad - \frac{L_1}{L_2} Q_0 \sin(mz)\mathcal{H}(L_1 + L_2 - x)\mathcal{H}(L_1 + L_2 + x)\,. \end{aligned}$$

Substituting this forcing into (2.50) along with the test solution $b(x,z) = b(x)\sin(mz)$, we find

$$b(x) \;=\; \begin{cases} \dfrac{\alpha Q_0 m^2}{2N^2}\Big[L_1(L_1+L_2) - x^2\Big] & |x| \le L_1 \\ \dfrac{\alpha Q_0 L_1 m^2}{2N^2 L_2}\Big(L_1 + L_2 - |x|\Big)^2 & L_1 < |x| < L_1 + L_2 \\ 0 & L_1 + L_2 \le |x| \end{cases}\,. \tag{2.51}$$

This solution for $b(x)$ is the same as the solution for $h(x)$ in equation (2.7) with c replaced by N/m. In the column, the mean buoyancy anomaly is

$$\frac{1}{2L_1}\int_{-L_1}^{L_1} dx\, b(x) \;=\; \frac{\alpha m^2}{N^2} L_1^2 \left(\frac{1}{3} + \frac{1}{2}\frac{L_2}{L_1}\right) Q_0\,. \tag{2.52}$$

Therefore, we see that the timescale relating the forcing Q_0 to the steady-state anomaly is

$$\tau \;=\; \frac{\alpha m^2 L_1^2}{N^2}\left(\frac{1}{3} + \frac{1}{2}\frac{L_2}{L_1}\right) \qquad \text{(steady-state timescale)}\,. \tag{2.53}$$

Not surprisingly, this is the same timescale as in (2.9) with c replaced by N/m.

By analogy to the new WPG scheme given in Table 2.1 for the shallow-water equations, the Boussinesq fluid coupled to the new WPG scheme is described by

$$\begin{aligned}
\partial_t b &= -N^2 w + Q && (2.54)\\
\partial_z p &= \rho b && (2.55)\\
\partial_z w &= -\delta && (2.56)\\
\partial_t \delta' &= \frac{1}{\rho}\frac{p}{L_1^2} - \alpha^* \delta' && (2.57)\\
\delta &= \delta' + \frac{2\pi L_1}{HN}\partial_t \delta' \,, && (2.58)
\end{aligned}$$

with $\alpha^* = \alpha(1/3 + L_2/2L_1)$. Here, the buoyancy b plays a role analogous to that of h in the shallow-water equations. Equations (3.10) and (3.11) have no analog in the shallow-water equations, but are present here because the Boussinesq system is a continuously stratified fluid. Note that equations (3.12) and (2.58) are the same as the new WPG equations listed in Table 2.1, but with gh replaced by p and c replaced by NH/π, which is the wave speed of the first baroclinic mode. These equations can be combined to give a self-contained equation for b:

$$\partial_t^2 \partial_z^2 b + \alpha^* \partial_t \partial_z^2 b - \frac{2\pi N}{HL_1}\partial_t b - \frac{N^2}{L_1^2} b \;=\; \partial_t \partial_z^2 Q + \alpha^* \partial_z^2 Q \,. \qquad (2.59)$$

For inviscid transients of the form $b(z,t) = B_0 \exp(i\omega t + imz)$, we get

$$m^2\omega^2 - (2\pi N/HL_1) i\omega - (N/L_1)^2 \;=\; 0\,. \qquad (2.60)$$

If $m = \pi/H$, then

$$\omega \;=\; \frac{HN}{\pi L_1} i\,,$$

and b decays with the timescale $L_1\pi/HN$. This is the correct behavior for the first baroclinic mode. In steady state with $Q = Q_0 \sin(mz)$, the WPG equations reduces to

$$b \;=\; \frac{\alpha^* m^2 L^2}{N^2} Q_0\,. \qquad (2.61)$$

For our choice of α^*, this gives the correct relationship between b and Q.

At first glance, one might be concerned by the presence of the dry first baroclinic wave speed in (2.58), because moist convection coupled to dry dynamics can generate waves that move at speeds different from the dry gravity-wave phase speed. However, this occurs by a superposition of damped, dry, gravity waves, all of which travel at their respective dry phase speeds. To state this in another way, the large-scale gravity-wave dynamics are always dictated by a linear set of equations, regardless of the heat source. No matter how nonlinear the interactions between the convective heat source and the gravity waves, the coupled convection-wave dynamics are simply given by the dry, large-scale dynamics coupled to a heat source. The purpose of any supradomain-scale parameterization is to parameterize these large-scale dry dynamics, so the use of the dry gravity-wave speed is correct here, and in fact, not unique to WPG. Prior implementations of WTG also use the dry, first-baroclinic wave speed to set the relaxation timescale for the temperature profile, τ (Raymond & Zeng 2005; Sessions et al. 2010; Wang & Sobel 2011; Daleu et al. 2012).

For a fully compressible atmosphere, such as that simulated by a cloud-resolving model, WPG is implemented by the addition of a mass source $-\rho\delta$ as described by Romps (2012b). In the new WPG scheme, the divergence δ is governed by

$$\begin{aligned} \partial_t \delta'(z,t) &= \frac{\overline{p}(z,t) - p_0(z)}{\overline{\rho}(z,t) L_1^2} - \alpha^* \delta'(z,t) \qquad (2.62) \\ \delta(z,t) &= \delta'(z,t) + \frac{2\pi L_1}{HN} \partial_t \delta'(z,t)\,, \qquad (2.63) \end{aligned}$$

with $\alpha^* = \alpha(1/3 + L_2/2L_1)$. This pair of equations replaces equation (A1) in the appendix of Romps (2012a). Otherwise, the implementation of this new WPG scheme is identical to that described there and in Romps (2012a).

2.7 Discussion

This new WPG scheme is motivated by the observation that gravity waves can exert a back-reaction on a column of fluid as they exit that column, as illustrated by the change in sign of the dashed curve in Figure 2.3. By adding a term to the governing equation for the large-scale divergence δ, this behavior can be captured. The resulting formulation of WPG can simultaneously capture the timescale of gravity-wave transients (i.e., the time it takes for gravity waves to remove transient pressure anomalies from the column) and the timescale for steady-state solutions (i.e., the time that relates the steady-state buoyancy source to the steady-state buoyancy anomaly). As pointed out by Romps (2012b), neither WTG nor the original WPG are able to do this.

One problem that remains, at least superficially, is the inability of this new WPG to simultaneously capture the correct timescales for more than one transient baroclinic mode. In equation (2.58) for WPG in a Boussinesq fluid, the coefficient of the last term contains a π/H, which is the vertical wavenumber of the first baroclinic mode. As a consequence, the dispersion relation (2.60) only gives the correct timescale for transient modes with this wavenumber; higher wavenumbers are damped too quickly. Fortunately, the key to overcoming this problem is straightforward in the new WPG. Following a spectral decomposition approach akin to suggestions by Bergman & Sardeshmukh (2004) and Mapes (2004) and choosing a basis for the baroclinic modes, denoted by $c_k(z)$, we can write p, δ, and δ' as

$$p(z,t) = \sum_k p_k(t)c_k(z) \tag{2.64}$$

$$\delta(z,t) = \sum_k \delta_k(t)c_k(z) \tag{2.65}$$

$$\delta'(z,t) = \sum_k \delta'_k(t)c_k(z)\,. \tag{2.66}$$

Equations (3.12) and (2.58) can then be modified to

$$\partial_t \delta'_k = \frac{1}{\rho}\frac{p_k}{L_1^2} - \alpha^* \delta'_k \tag{2.67}$$

$$\delta_k = \delta'_k + \frac{2L_1}{N} m_k \partial_t \delta'_k\,, \tag{2.68}$$

where $m_k = k\pi/H$. This differs from equations (3.12) and (2.58) in that the coefficient in (2.68) now contains the vertical wave number m_k, which results in a mode-specific phase speed, N/m_k. In a practical implementation, this simply requires decomposing p into modes at each time step (truncating at some sufficiently high wavenumber n) and integrating n prognostic equations for the n different δ'_k. An analogous decomposition can be made for a compressible fluid.

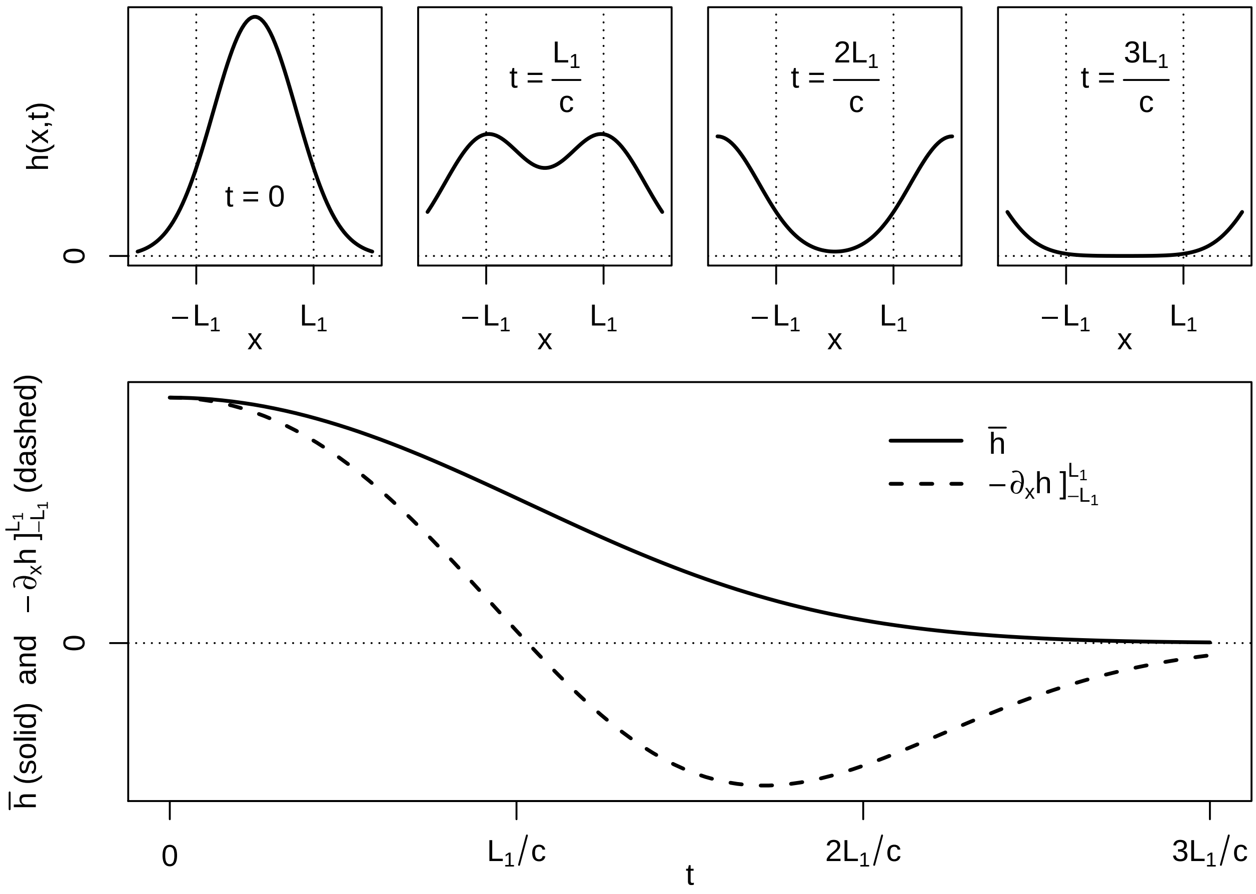

Figure 2.3: For a stationary ($\delta = 0$) Gaussian ($h \propto e^{-x^2/L_1^2}$) centered on the column at time $t = 0$, the solution for $t > 0$ is of two Gaussians propagating to the left and right. As seen in the lower plot, the average h in the column ($\overline{h}$, solid curve) decreases monotonically, but the pressure-gradient force at the edges of the column ($-\partial_x h|_{-L_1}^{L_1}$, dashed curve) switches from divergent to convergent at $t = 1$. This mismatch between $\overline{h}$ and $-\partial_x h|_{-L_1}^{L_1}$ motivates the addition of a new term to the WPG equations.

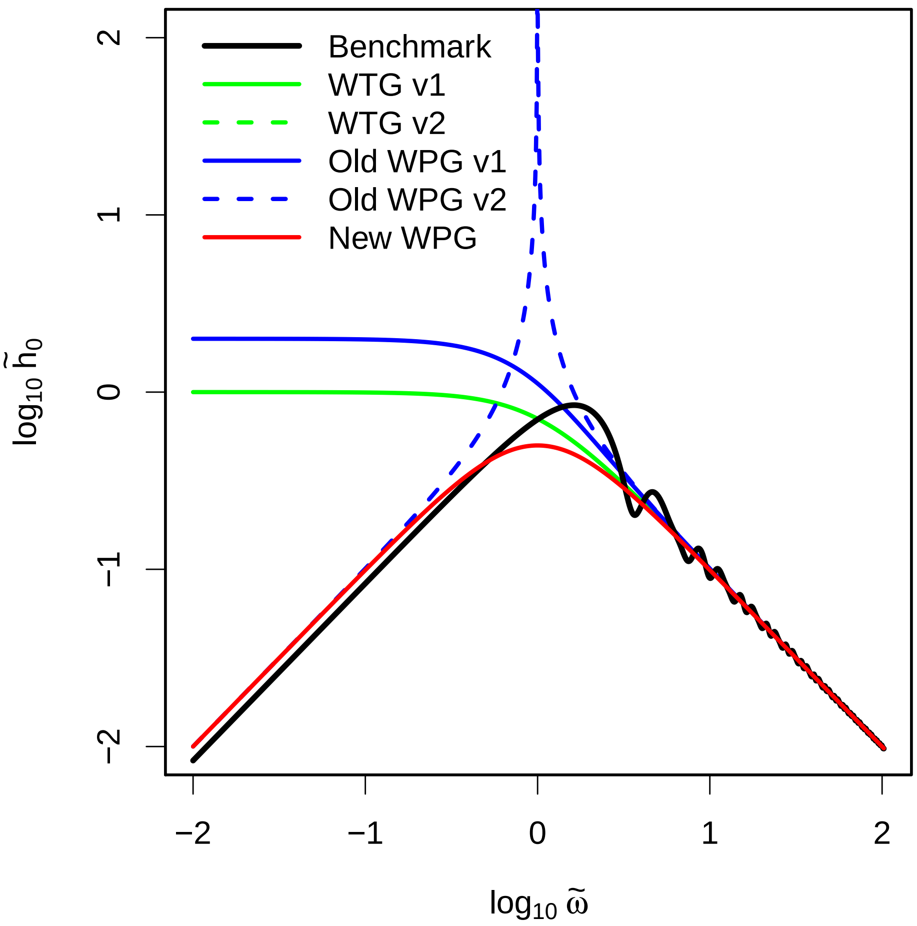

Figure 2.4: For inviscid dynamics ($\alpha = 0$) and $L_1/L_2 = 1$, the non-dimensionalized amplitude $\tilde{h}_0$ in response to an oscillatory forcing Q with non-dimensionalized angular frequency $\tilde{\omega}$.

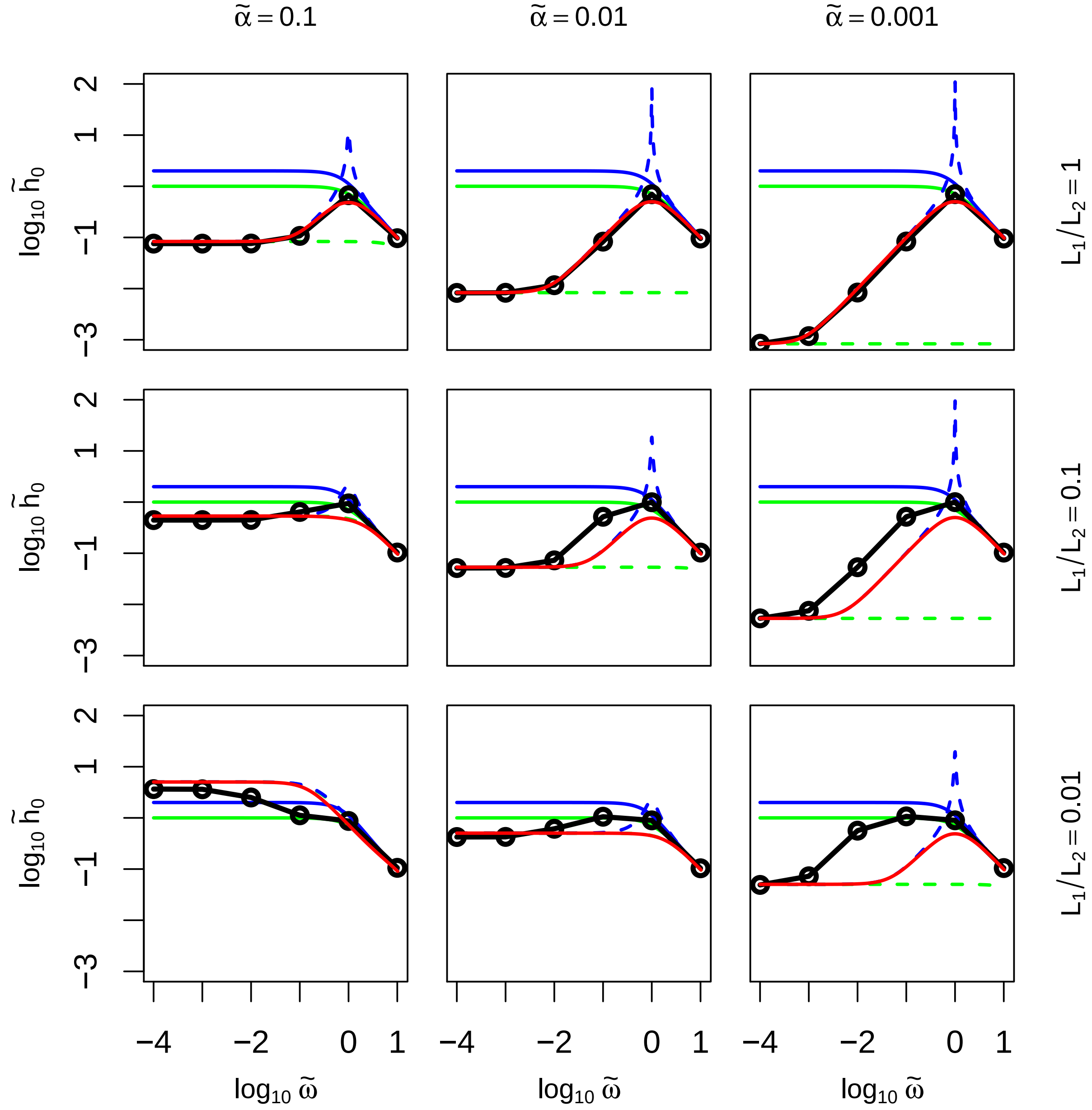

Figure 2.5: The non-dimensionalized amplitude $\tilde{h}_0$ in response to an oscillatory forcing with non-dimensionalized angular frequency $\tilde{\omega}$. Plots of $\log_{10}(\tilde{h}_0)$ versus $\log_{10}(\tilde{\omega})$ are shown for all combinations of $L_1/L_2 = 1$, 0.1, and 0.01 (rows 1 through 3) and non-dimensionalized $\tilde{\alpha} = 0.1$, 0.01, and 0.001 (columns 1 through 3). Results are shown for (black circles) benchmark numerical model, (green solid) WTG v1, (green dashed) WTG v2, (blue solid) old WPG v1, (blue dashed) old WPG v2, and (red) new WPG.

Chapter 3

Self-consistency tests of large-scale-dynamics parameterizations for single-column modeling[1]

Large-scale dynamics parameterizations are tested numerically in cloud-resolving simulations, including a new version of the weak-pressure-gradient approximation (WPG) introduced in Chapter 2 and Edman & Romps (2014), the weak-temperature-gradient approximation (WTG), and a prior implementation of WPG. We perform a series of self-consistency tests with each large-scale dynamics parameterization, in which we compare the result of a cloud-resolving simulation coupled to WTG or WPG with an otherwise identical simulation with prescribed large-scale convergence. In self-consistency tests based on radiative-convective equilibrium (RCE; i.e., no large-scale convergence), we find that simulations either weakly coupled or strongly coupled to either WPG or WTG are self-consistent, but WPG-coupled simulations exhibit a non-monotonic behavior as the strength of the coupling to WPG is varied. We also perform self-consistency tests based on observed forcings from two observational campaigns: the Tropical Warm Pool International Cloud Experiment (TWP-ICE) and the ARM Southern Great Plains (SGP) Summer 1995 IOP. In these tests, we show that the new version of WPG improves upon prior versions of WPG by eliminating a potentially troublesome gravity-wave resonance.

3.1 Introduction

Studies of idealized tropical dynamics using single-column and cloud-resolving simulations frequently incorporate parameterized large-scale dynamics to capture the interaction between

---

[1] **Material in this chapter originally published in Edman & Romps (2015), under a Creative Commons license.**

the modeled domain and the environment (e.g. Chiang & Sobel 2002; Raymond & Zeng 2005; Kuang 2008, 2011; Emanuel & Sobel 2013; Bony et al. 2013). A large-scale dynamics parameterization, also referred to as a supradomain-scale (SDS) parameterization (Romps 2012b), diagnoses the large-scale convergence into a modeled column by comparing the modeled profile of pressure or temperature to a reference environmental profile. There are two main SDS schemes: the weak-temperature-gradient approximation (WTG) and the weak-pressure-gradient or damped-wave approximation (WPG). In the former, horizontal temperature gradients are assumed to be small, and buoyancy differences between the column and the reference environment are relaxed by vertical advection of potential temperature on some fixed timescale (Sobel & Bretherton 2000; Raymond & Zeng 2005; Sessions et al. 2010; Wang & Sobel 2012; Wang et al. 2013). On the other hand, WPG uses a parameterized form of the pressure-gradient force between the column and the reference environment to diagnose large-scale convergence (Holton 1973; Nilsson & Emanuel 1999; Raymond & Zeng 2000; Kuang 2008; Blossey et al. 2009; Kuang 2011; Romps 2012b,a; Edman & Romps 2014).

The goal of an SDS scheme is to produce the convergence profile that a modeled column would experience if immersed in the chosen environment. The convective dynamics within the column are modeled with either a single-column model (SCM), typically with a convective parameterization, or with a cloud-resolving model (CRM). A typical use for an SDS scheme is to feed it a time-dependent profile of temperature or pressure from observations and see whether the SCM or CRM faithfully replicates the observed precipitation. In this case, any mismatch between the observed and modeled precipitation may be due to errors in the SDS scheme, errors in the SCM/CRM, or both. Therefore, these types of simulations are not well-suited for evaluating the SDS schemes.

To evaluate the SDS schemes, we need to eliminate the influence of model error. This can be accomplished by using an SCM/CRM simulation as the benchmark. Consider two simulations that use the same SCM or CRM, as depicted in Figure 3.1. Run 1 may, in general, be forced with any time-dependent convergence, horizontal advection, surface fluxes, and nudging. These forcings may be taken from observations or they may be constructed artificially. Run 2 uses the same set of forcings minus the convergence. Instead of being forced with a time-dependent convergence profile, run 2 uses an SDS scheme to calculate its convergence profile. And, in particular, the SDS scheme uses the temperature (for WTG) or pressure (for WPG) from run 1 as the environmental profile. Since the model used in both runs is the same, and since the forcings are identical aside from the use of the SDS scheme, any differences in the resulting model output will be due to a failure of the SDS scheme. If the model outputs are the same, then we say that the SDS scheme has passed the self-consistency test. Here, "self-consistency" refers to the model behaving the same as itself.

A more explicit example of what we mean by self-consistency is the following. Imagine a large-domain simulation of statistically steady and uniform convection. Now, consider a small subdomain. This small subdomain, if left immersed in the large-domain simulation, is unambiguously stable. If, when coupled to WTG or WPG using a reference profile representative of the larger domain, the small subdomain continues to evolve in the same statistically steady manner as it did when immersed in the large domain, then we would

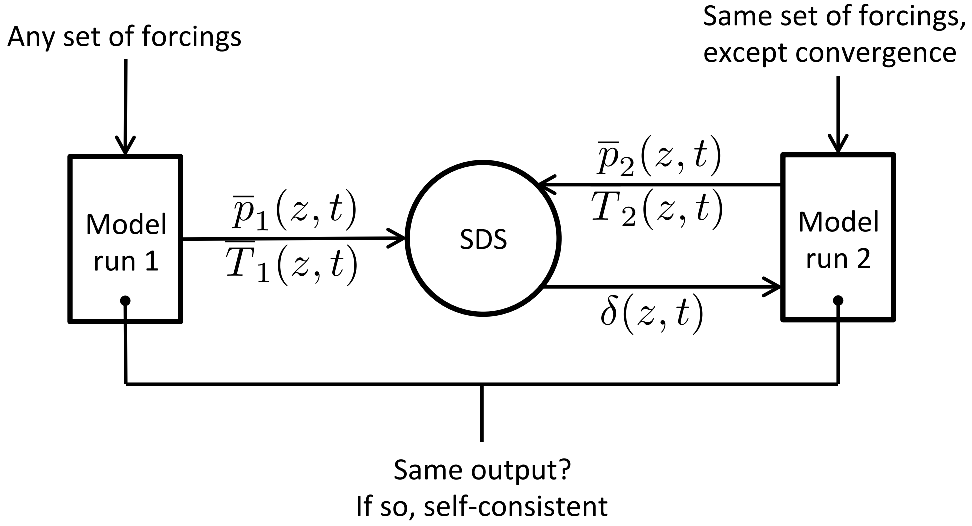

Figure 3.1: A general self-consistency test for an SDS scheme. An SDS scheme passes the self-consistency test if two simulations of the same SCM or CRM give the same output when forced as depicted above. In particular, run 2 is forced with the same set of forcings as run 1, except that the convergence profile is determined from the SDS scheme rather than being prescribed. In the SDS scheme, the environmental profile (either pressure for WPG or temperature for WTG) is taken from run 1.

say that this simulation passes the self-consistency test. If the coupled simulation develops a different large-scale circulation, then the large-scale dynamics parameterization is not faithfully representing the interaction between the smaller subdomain and the large-scale environment. We would say, in this case, that the SDS scheme fails the self-consistency test.

In particular, we will say that an SDS scheme passes the self-consistency test if it generates domain-mean anomalous ascent or descent that is much smaller in magnitude than the radiatively driven clear-sky descent speed in the benchmark simulation. For example, an SDS scheme that perfectly replicates an RCE benchmark will have a domain-mean ascent profile that is zero; since zero is certainly less than $O(0.1)$ of the radiatively driven clear-sky descent speed, this SDS is self-consistent. On the other hand, if the SDS scheme causes the atmosphere to dry out and descend *en masse* to balance radiative cooling, then the domain-mean descent speed will be comparable to the clear-sky descent speed in the benchmark RCE simulation; therefore, this SDS scheme would be considered to have failed the self-consistency test in spectacular fashion.

Much of the work using single-column and cloud-resolving models coupled to large-scale dynamics parameterizations has focused on the conditions leading to multiple equilibria (i.e., the presence of distinct wet and dry equilibrium states; Sobel et al. 2007; Sessions et al. 2010) or on comparisons with observations (e.g., Wang et al. 2013). There has been comparatively little effort expended on studying whether or not commonly used SDS schemes can simply reproduce the behavior of a model immersed in a larger version of itself. This is the goal of the self-consistency tests we conduct in this study. In order to reliably compare model results with observations, one might reasonably expect that an SDS scheme must be able to pass a self-consistency test. Some implementations of WTG have been shown to fail self-consistency tests (Raymond & Zeng 2005; Raymond 2007; Daleu et al. 2012), and Kuang (2011) found that one implementation of WPG was passes for some parameter choices, but not others.

But, is it fair to expect these SDS schemes to succeed in these self-consistency tests? What if failing a self-consistency test simply reflects a true instability in convecting atmospheres, whereby a statistically uniform patch of atmosphere evolves a large-scale circulation? Indeed, it has been suggested that the existence of multiple equilibria in single-column models with an SDS scheme is related to the phenomenon of convective aggregation (Sobel et al. 2007). Fortunately, we can exclude this possibility so long as we use fixed radiative cooling profiles in the self-consistency tests. Although convective aggregation has been studied extensively in numerical models (Held et al. 1993; Bretherton et al. 2005; Stephens et al. 2008; Muller & Held 2012; Jeevanjee & Romps 2013; Emanuel et al. 2014; Wing & Emanuel 2014), there has been no example of convective aggregation with fixed, horizontally uniform radiative cooling. In fact, all indications are that interactive radiation (i.e., radiation that interacts with water vapor and clouds) is essential to the triggering and maintenance of convective aggregation. Therefore, when using fixed radiation, SDS schemes should be able to pass self-consistency tests .

A key motivation for this study is to test the new form of WPG introduced in Chapter 2 and Edman & Romps (2014) in a cloud-resolving framework. In that study, we used an idealized shallow-water framework to show that the new WPG improves upon previous implementations of WPG and WTG by more accurately capturing steady-state and transient dynamics. Additionally, in the idealized system, this new form of WPG removes a potentially troublesome gravity-wave resonance found in prior versions of WPG. In such a case, rather than damping the buoyancy anomaly away on the timescale for gravity-wave emission from the column, the column coupled to old WPG behaves as though an infinite, convectively-coupled wave is passing through the domain (Romps 2012b). This behavior is undesirable if one is attempting to parameterize the interaction between convection and large-scale convergence. In this study, we present evidence that this gravity wave resonance can cause problems in simulations coupled to WPG and show that it is eliminated entirely in the new WPG presented in Chapter 2 and Edman & Romps (2014).

In this paper, we use cloud-resolving simulations with and without large-scale dynamics parameterizations to test the claims of improvement to WPG made by Edman & Romps (2014) using self-consistency tests. First, we perform self-consistency tests with WPG and WTG using a cloud-resolving model in a simple radiative-convective equilibrium (RCE) framework. We also perform self-consistency tests with observed forcings, by comparing simulations forced with vertical-velocity observations from two observational campaigns – the Tropical Warm Pool International Cloud Experiment (TWP-ICE; Fridlind et al. 2010) and the Atmospheric Radiation Measurement (ARM) Southern Great Plains (SGP) intensive observational period (IOP) of July 1995 (Ghan et al. 1999) – with simulations using large-scale dynamics parameterized by new WPG, old WPG, and WTG. Section 3.2 describes the implementations of the three large-scale dynamics parameterizations used in this study (2 versions of WPG, 1 version of WTG). Section 3.3 describes the RCE self-consistency tests and contains a brief discussion of their implications. In section 3.4, we describe the self-consistency tests based on the TWP-ICE and SGP data and discuss the gravity wave resonance problem in old WPG. We conclude with a brief discussion in Section 3.5.

3.2 Implementations of WPG and WTG

The SDS scheme that we refer to as "old WPG" is the version used in Romps (2012a). The horizontal divergence $\delta(z,t)$ is calculated by

$$\partial_t \delta(z,t) = \frac{1}{L^2} \frac{\overline{p}(z,t) - p_0(z,t)}{\overline{\rho}(z,t)} - \alpha^* \delta(z,t)\,, \tag{3.1}$$

where the overbar represents the horizontal average over the column and a subscript 0 denotes the environmental reference profile that is provided to the parameterization. The length scale L and time scale $1/\alpha^*$ are input parameters to the scheme.

"New WPG" is a modification to old WPG introduced in Chapter 2 and Edman & Romps

(2014), in which equation 3.1 is replaced by the following pair of equations:

$$\partial_t \delta'(z,t) = \frac{1}{L^2}\frac{\overline{p}(z,t) - p_0(z,t)}{\overline{\rho}(z,t)} - \alpha^* \delta'(z,t)\,, \tag{3.2}$$

$$\delta(z,t) = \delta'(z,t) + \frac{2\pi L}{HN}\partial_t \delta'(z,t)\,. \tag{3.3}$$

Here, the horizontal divergence $\delta(z,t)$ is the old WPG divergence $\delta'(z,t)$ modified by a term proportional to the length scale L divided by the first-baroclinic wave speed NH/π (i.e. the time for a dry first-baroclinic wave to cover a distance L), where N is a reference Brunt-Väisälä frequency and H is the height scale. This factor is added to account for the back reaction exerted on a column of fluid by gravity waves exiting the column, as described in Chapter 2 and Edman & Romps (2014).

We implement WTG in the relaxed form following Raymond & Zeng (2005), where the vertical velocity $w(z,t)$ is calculated as

$$w(z,t) = \frac{\overline{\theta}_v(z,t) - \theta_{v0}(z,t)}{\tau \max[\gamma, \partial_z \theta_{v0}(z,t)]} \tag{3.4}$$

above a height of 1 km. Below $z = 1$ km, w is linearly interpolated to zero at the surface. A minimum stability of $\gamma = 0.01$ K km^{-1} is enforced in the denominator to avoid singularities, and τ is a relaxation time scale that is an input parameter to the scheme. This vertical velocity is then converted to a horizontal divergence $\delta(z,t)$ by

$$\delta(z,t) = -\frac{1}{\overline{\rho}(z,t)}\partial_z[\overline{\rho}(z,t) w(z,t)] \tag{3.5}$$

The horizontal divergence calculated by an SDS scheme defines a mass source, $-\rho\delta$, which is added to the cloud-resolving model's tendencies of density, water vapor, and temperature. Following Romps (2012a), we also include the horizontal advective effect of convergence over the modeled domain in the tendencies of potential temperature and water vapor. This is represented by a second-order centered method, such that the tendency equations have the following modifications:

$$\partial_t \rho(\mathbf{x},t) = -\rho(\mathbf{x},t)\delta(z,t) + \ldots \tag{3.6}$$

$$\partial_t \left[\rho(\mathbf{x},t) q_v(\mathbf{x},t)\right] = -\rho(\mathbf{x},t)\delta(z,t)\left\{q_v(\mathbf{x},t) + \frac{1}{2}[q_{v0}(z) - q_v(\mathbf{x},t)]\right\} + \ldots \tag{3.7}$$

$$\partial_t \left[\rho(\mathbf{x},t) \theta(\mathbf{x},t)\right] = -\rho(\mathbf{x},t)\delta(z,t)\left\{\theta(\mathbf{x},t) + \frac{1}{2}[\theta_0(z) - \theta(\mathbf{x},t)]\right\} + \ldots \tag{3.8}$$

Note that the above equation for potential temperature θ was incorrectly written in terms of absolute temperature in Romps (2012a), but it was correctly implemented in terms of potential temperature both there and here.

All simulations are performed using the fully-compressible, cloud-resolving model Das Atmosphärische Modell (DAM, Romps 2008) with 2-km grid spacing in the horizontal, a doubly periodic domain, and no Coriolis force. The vertical grid is stretched, ranging from approximately 50-m grid spacing near the surface, up to 1 km near the model top, which is at 32 km.

3.3 Self-consistency in RCE

Radiative-convective equilibrium (RCE) is a state of no mean convergence into the simulated column, and it serves as a particularly simple situation in which to test self-consistency. We use the following basic procedure for the self-consistency tests: 1) run a cloud-resolving model to RCE with fixed SST and fixed radiative cooling, without any SDS scheme; 2) run an identical simulation, but coupled to either WPG or WTG, using the mean profiles of pressure (for WPG) or temperature (for WTG) from the first simulation as the reference environment. These two steps correspond to model runs 1 and 2 in Figure 3.1. If the SDS scheme passes the self-consistency test, run 2 should exhibit no mean ascent.

For both runs 1 and 2, surface fluxes are calculated using a bulk aerodynamic formula over an ocean with a fixed SST of 300 K and the profile of radiative cooling is fixed as the average of an otherwise identical 120-day RCE simulation with interactive radiation. Run 1 lasts 240 days; run 2 is initialized from a 3D snapshot taken at the end of the run 1, and it lasts 90 days. The reference profiles of temperature, pressure, and water vapor used as input to the SDS schemes in run 2 are averages over the last 120 days of run 1.

Self-consistency in RCE appears to depend on the choice of relaxation parameter for each scheme (e.g., τ for WTG and L for both WPGs). We test three choices of relaxation parameter for each scheme, corresponding to different adjustment timescales (τ) for WTG, and different length scales (L) for WPG. The three values of L are 128 km, 1280 km, and 12800 km. The smallest value of L is twice the width of the domain and the largest is $\approx 1/3$ the circumference of the earth at the equator. For WTG, τ is set to L/c, where $c \approx 50$ m s^{-1} is the approximate wave speed of the first baroclinic mode in the tropical atmosphere, so τ takes the values 0.725, 7.25, and 72.5 hours. Additional simulations (not shown) with a larger domain (144 x 144 km) indicate that WTG may become more self-consistent with larger domain sizes, while WPG is much less sensitive.

Figure 3.2 shows the precipitation time series from the last part of run 1 (RCE) and the entirety of run 2 (the SDS parameterized simulations) for each choice of SDS scheme and relaxation parameter. Run 2 begins at day 240 and continues until day 330; thick, colored lines show results for WTG (top), old WPG (middle), and new WPG (bottom). For all SDS schemes with the parameter choice corresponding to the slowest adjustment (e.g., $\tau = 72.5$ hours and $L = 12800$ km; orange lines in figure 3.2) the precipitation time series for run 2 is nearly indistinguishable from the RCE in run 1 (thin black lines). In those cases, the parameterized adjustment is so weak that the column is effectively decoupled from the environment.

For $L = 1280$ km, both new and old WPG exhibit oscillatory behavior on a $\approx$ 10-day timescale, similar to that seen in Kuang (2011), and there is less mean precipitation than in the RCE run. The 10-day oscillation and most of the change in the mean disappears for $L = 128$ km, but larger variability on shorter timescales remains (although this is somewhat reduced for new WPG relative to old WPG). For both choices of τ, WTG appears more similar to the RCE case than any of the versions of WPG. There is almost no change in the mean precipitation relative to the RCE case, but the case with $\tau = 7.25$ hours has a $\approx$ 10-day period oscillation similar to both versions of WPG, albeit with smaller amplitude. Note that this 10-day oscillation is distinct from the gravity-wave resonance discussed previously; it is not possible for the gravity wave resonance to occur in WTG or new WPG. Also, the p and w anomalies are in phase for 10-day period oscillations, in contrast to the gravity wave resonance where the p and w anomalies are in quadrature.

Figure 3.3 shows the resulting vertical-velocity profiles for each of the "run 2" simulations, averaged over the full 90 days. For a large-scale dynamics parameterization that is perfectly self-consistent, the mean vertical-velocity profile would be zero at all heights, i.e., the same as the RCE state. This requirement is very closely met in the cases of $\tau = 72.5$ hours and $L = 12800$ km; these parameters are planetary-scale, so that the coupling to large-scale dynamics is so weak that it has a negligible effect on the modeled convection and the column is actually in RCE. For other values of L and τ, there are noticeable deviations of the vertical-velocity profiles from zero; these deviations will be compared to the radiatively drive descent speeds below. As expected, the mean vertical-velocity profiles for new and old WPG are nearly identical; the two schemes only differ in their treatment of transient disturbances.

One striking feature of these simulations is the agreement between WPG and WTG for small L and τ; for $L = 128$ km and $\tau = 0.725$ hours, the vertical-velocity profiles are almost identical, with strongly third-baroclinic structure. This agrees with the findings of Kuang (2012), who found that simulations of atmospheric circulations over SST hotspots using WTG and WPG converge to a similar third-baroclinic structure (see figures 10 and 11 of Kuang (2012)) in the limit of small L and τ. It is notable that this same structure persists in our RCE self-consistency tests, in the absence of any SST anomaly.

On the other hand, WTG and WPG exhibit very different behavior as the relaxation parameter is increased. For WTG, increasing τ reduces the mean vertical motion, which decreases monotonically toward zero until the column is in RCE (e.g., the simulations with $\tau = 72.5$ hours). This agrees with the findings of Daleu et al. (2012), although their model had descending motion for all values of τ; clearly some aspects of this circulation are dependent on the model setup, although the parameter dependence seems robust. In contrast, the vertical motion in the WPG simulations does not monotonically decrease toward zero as L is increased. When L is increased from 128 km to 1280 km, the third-baroclinic structure in the vertical-velocity profile disappears, and is replaced by first-baroclinic descent with more than twice the magnitude. But, as L is increased further, the column does in fact approach RCE (e.g., the WPG simulations with $L = 12800$ km). The WPG simulations of Kuang (2012) also show this tendency toward deeper structure for larger L, but the non-monotonic approach to RCE is a novel feature of these simulations.

Although these nonzero vertical-velocity profiles tell us that WTG and WPG are not perfect, are they "good enough" for practical use? Our criteria for passing a self-consistency test – that the vertical-velocity errors are small compared to radiatively driven clear-sky subsidence – is designed to answer this question. The net radiative cooling rate of the troposphere is equal to about 1 K day^{-1}. The subsidence rate is given by $w = gQ/N^2T$, where N is the Brunt-Väisälä frequency and Q is the radiative cooling rate in dimensions of Kelvin per time. Using values realistic for the mid-troposphere, this results in $w \approx -4$ mm

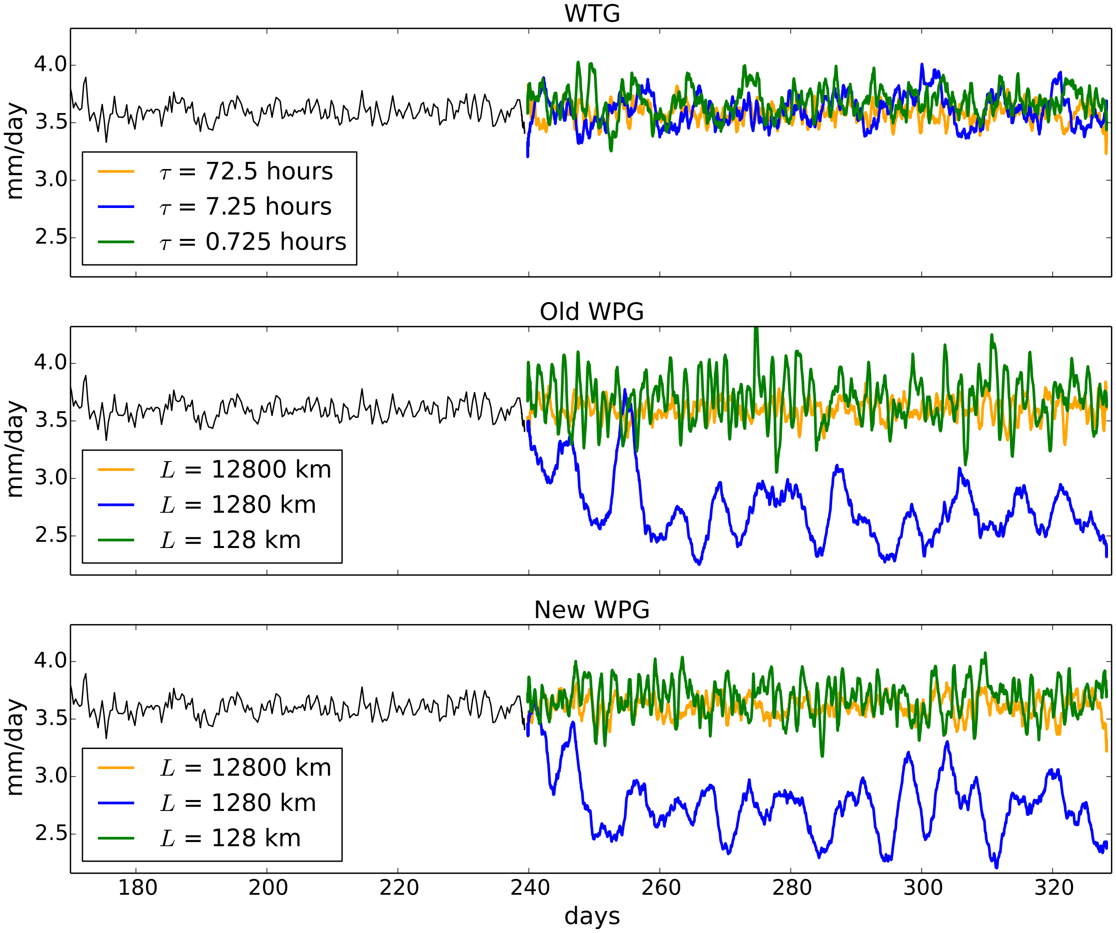

Figure 3.2: Rainfall time series for the RCE self-consistency tests. In all panels, the thin black line depicts the domain-averaged precipitation from the RCE simulation. The results of the coupled simulations (WTG, top; old WPG, middle; new WPG, bottom) are shown after day 240; the green lines represent the precipitation from simulations with the strongest coupling to WPG or WTG (e.g. $L = 128$ km for WPG, $\tau = 0.725$ hours for WTG), the blue lines show the intermediate choice, and the orange lines show the case with the weakest coupling, which is effectively RCE for all the SDS schemes.

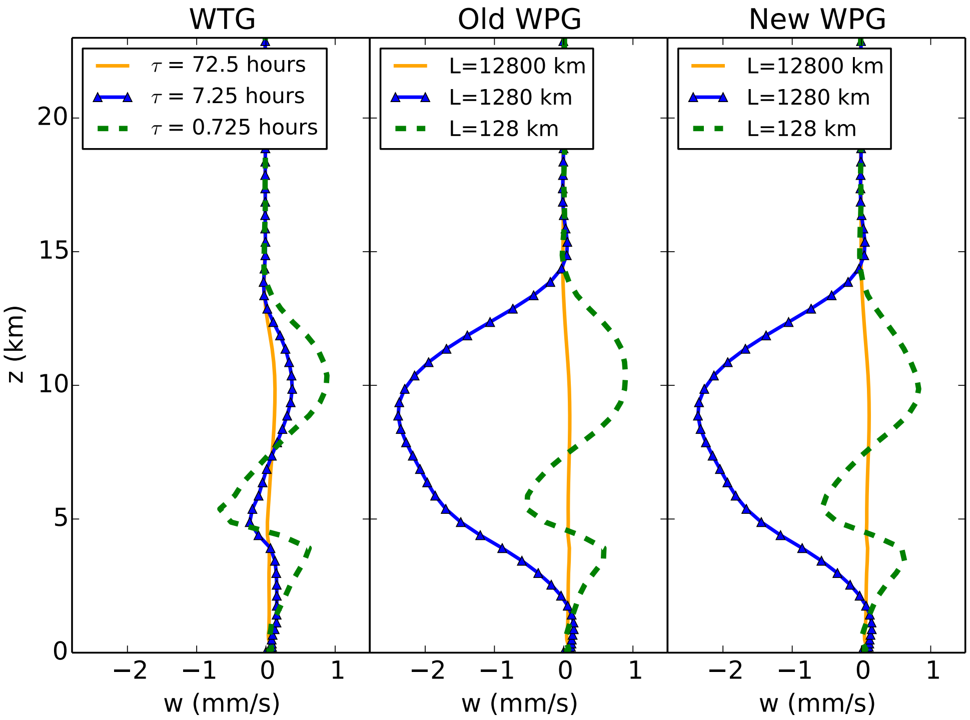

Figure 3.3: 90-day mean profiles of vertical velocity from RCE self-consistency tests for each of the large-scale dynamics parameterizations (left, WTG; middle, old WPG; right, new WPG) for three parameter choices (see legend).

s^{-1}. For all three values of τ, the domain-mean w in the WTG simulations is $\lesssim 1$ mm s^{-1}, which is much smaller in magnitude than ≈ 4 mm s^{-1}, so we conclude that WTG passes these self-consistency tests. The story is a bit different, however, for WPG. For small and large L (128 km and 12800 km), the WPG profiles are nearly identical to the WTG profiles for small and large τ (0.725 and 72.5 hours), and they meet the requirement for self-consistency. For intermediate L (1280 km), however, the WPG profile takes a value of about -2 mm s^{-1}, which is comparable to the radiatively driven clear-sky descent speed of about -4 mm s^{-1}. For intermediate L, therefore, we conclude that new and old WPG do not pass these self-consistency tests. In the next section, we perform self-consistency tests with observed forcing, which emphasizes the ability of each SDS scheme to deal with transient disturbances.

3.4 Self-consistency with observed forcings

We adapted case studies from two observational campaigns focused on single-column model intercomparisons: the Tropical Warm Pool International Cloud Experiment (TWP-ICE, Fridlind et al. 2010) and the July 1995 intensive observation period (IOP) at the ARM Southern Great Plains site (Ghan et al. 1999). However, rather than use the observed environmental reference profiles to drive WPG and WTG (e.g., as in Wang et al. 2013), we "filter" the observations through a benchmark simulation forced with the observed vertical velocity, and then use the pressure and temperature profiles from the benchmark simulation as input to WPG and WTG. This is the same procedure depicted in Figure 3.1. This self-consistency test allows for a direct comparison between the benchmark and SDS-enabled simulations without contamination from any model or observational errors other than those introduced by the SDS scheme itself.

For the time-varying self-consistency tests, we use a 128-km square domain. The benchmark simulation is forced with the observed large-scale vertical velocity from observations. The simulations with parameterized large-scale dynamics derive their own vertical velocity using time-varying reference profiles taken from the benchmark simulation. Because WPG and WTG have been shown to respond strongly to variations in surface fluxes (Wang et al. 2013), but we are mainly interested in their ability to produce convergence profiles consistent with heating anomalies in the column, we use time-invariant surface and advective forcings and non-interactive (but time-varying) radiative cooling profiles for both the benchmark and WPG/WTG coupled experiments.

Additionally, all simulations are initialized using observed profiles of wind, temperature, and humidity; the temperature field is perturbed with 0.01-K noise in the first layer of the domain. Parameters for new and old WPG are set following Edman & Romps (2014), with $L = 128$ km (the size of the domain) and $\alpha^* = \alpha(1/3 + r/2)$, where $1/\alpha$ is the Rayleigh damping timescale for the troposphere, taken here to be 5 days. The value of r is not well constrained (see discussion in Chapter 2), but it represents the ratio of the size of the region affected by anomalous convection in the modeled column to the size of the anomalously convecting column; here we set $r = 10$. For new WPG, we set the factor $2\pi/HN = 0.042$ s m^{-1}, corresponding to $H = 15$ km and $N = 0.01$ s^{-1}. For WTG, we set τ as the time for a first baroclinic wave to traverse the domain $\tau = 128$ km/49 m s^{-1} $= 0.725$ hours, which is comfortably within the range established by previous studies (e.g., Cohen & Craig 2004; Wang & Sobel 2011; Wang et al. 2013).

3.4.1 TWP-ICE

For the TWP-ICE self-consistency test, the surface fluxes and radiative cooling profile for the benchmark and WPG/WTG runs are taken from a simulation identical to the benchmark simulation (prescribed observed vertical velocity), but with surface fluxes calculated interactively using the bulk aerodynamic formula over an ocean with SST fixed at the observed mean of 302 K, and radiation calculated interactively every 10 minutes. To assess the relative performance of WTG, old WPG, and new WPG, we compare the precipitation time series from each simulation with parameterized large-scale dynamics against the precipitation time series from the benchmark simulation. Precipitation is a relatively holistic way to assess performance, because it is closely related to the large-scale convergence produced by the SDS scheme.

The resulting precipitation time series are shown in Figure 3.4. WTG, old WPG, and new WPG are shown in the top, middle, and bottom panels, respectively. In all three panels, the result of the benchmark simulation is shown by the thin black line. By eye, all of the parameterizations perform relatively well throughout the entire 16-day period. More quantitatively, the R^2 values are 0.590, 0.656, and 0.780 for WTG, old WPG, and new WPG, respectively. In the first half of the simulation period, both new WPG and WTG capture the timing and magnitude of the relatively large, almost-daily precipitation events in the benchmark, although the peaks for the WTG case lag the benchmark slightly, and the amplitude of the largest event at the end of day 5 is too small. Old WPG gets the timing of the events roughly correct, but more often than not produces larger amplitudes than the benchmark. In the latter half of the simulation, when the benchmark is characterized by smaller amplitude precipitation events, WTG performs better than either new WPG or old WPG, which both predict more intermittent precipitation in the latter half of the simulation than the benchmark.

3.4.2 ARM-Southern Great Plains

In addition to the TWP-ICE experiments, we perform tests using a nearly identical model setup and procedure applied to data from the July 1995 intensive observation period (IOP) at the ARM Southern Great Plains (SGP) site (Ghan et al. 1999). A time-varying radiative cooling profile (from a separate simulation) and time-invariant surface advective tendencies (from observations) are applied as in the TWP-ICE experiments. Because this field site is over land rather than ocean, we prescribe the time-mean of the observed surface fluxes for all SGP simulations. Additionally, for the WPG runs, we apply the same boundary layer linearization used in WTG to reduce the sensitivity to the diurnal cycle of heating.

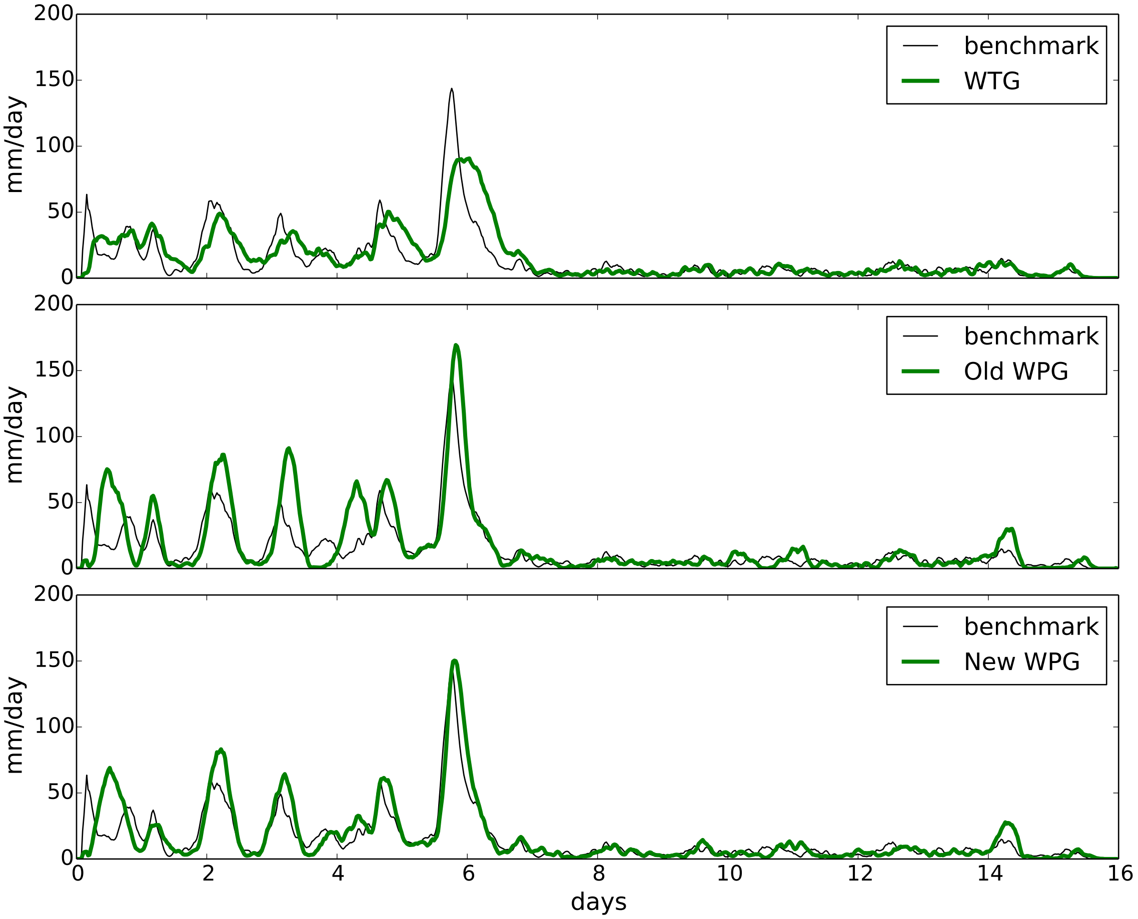

Figure 3.4: Precipitation time series for the TWP-ICE test case. In all panels, the thin black line is the precipitation rate from the benchmark simulation with prescribed w. The thick green line in the top panel is the precipitation from the simulation coupled to WTG ($\tau = 0.725$ hours); the middle and bottom panels show old WPG and new WPG ($L = 128$ km for both), respectively.

We do not include the effects of rotation, despite the fact that the ARM SGP site is located at 36.5° N, well outside the tropics. At this latitude, the Rossby deformation radius is ≈2000 km, which is an order of magnitude greater than the horizontal extent of the model domain. Thus, we might expect that rotation would not affect the dynamics contained within the model domain, and the assumption of weak temperature and pressure gradients across the model domain and the environment are not grossly violated. Also, convection in the midlatitudes is more strongly forced by large-scale convergence than in the tropics; on these grounds we might expect parameterized large-scale dynamics to actually perform better in midlatitudes than in the tropics.

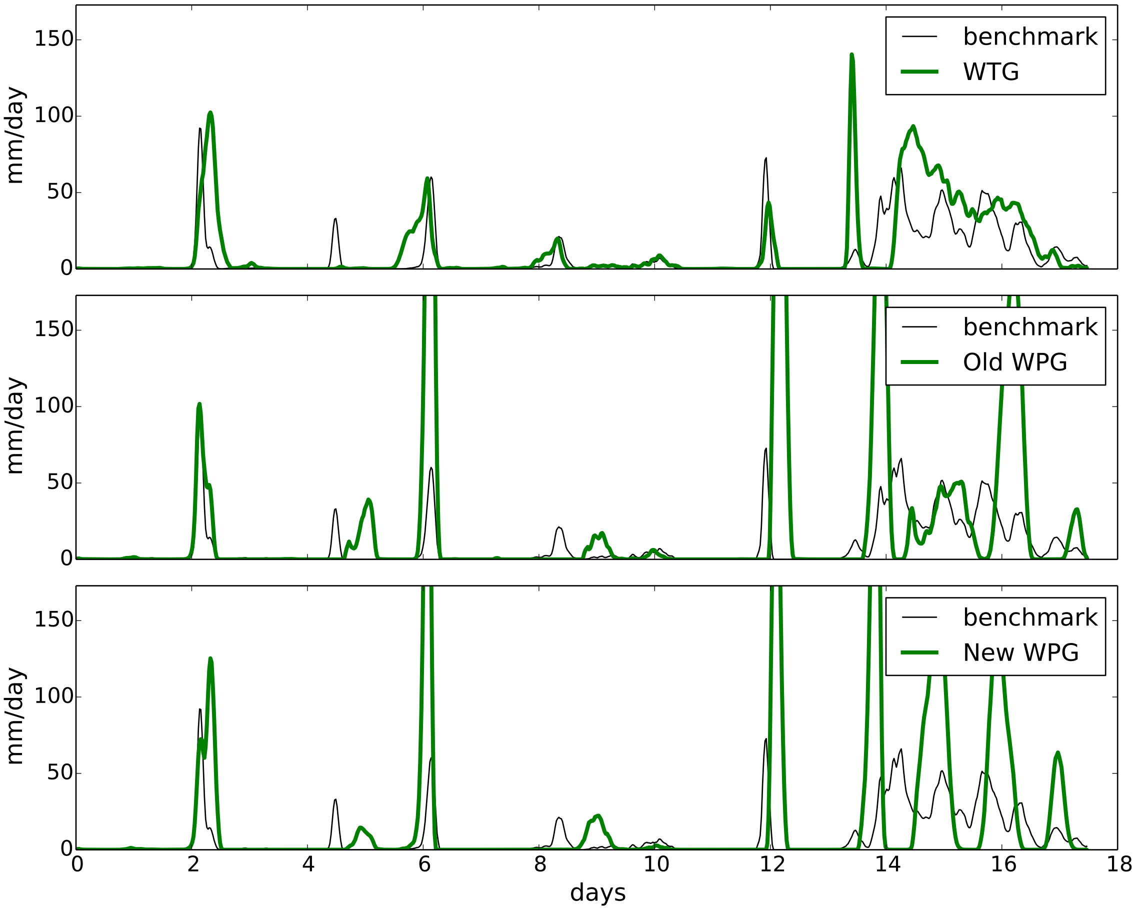

Figure 3.5: Same as Figure 3.4, but for the SGP test case. Maximum rainfall rates for the old WPG and new WPG cases are 422 mm/day and 365 mm/day, respectively.

Figure 3.5 shows the precipitation time series from simulations based on the SGP case using WTG (top), old WPG (middle), and new WPG (bottom). Again, in all three panels, precipitation from the benchmark simulation (forced vertical velocity) is shown by the thin black line.

By eye, we see that WTG outperforms both new and old WPG for this case, although none of the parameterizations perform as well as in the TWP-ICE self-consistency test. The precipitation events in WTG (top panel, thick red line) are close to the same magnitude as the benchmark, with the exception of the event on day 13, which is spuriously large, and the event on day 4, which is absent. The timing of WTG precipitation events is similar to the benchmark, although some WTG events lead the benchmark by up to 12 hours (days 6 and 8) while others lag by a few hours (days 2 and 14). On the other hand, both versions of WPG over-predict the magnitude of almost all precipitation events, and the timing is significantly delayed for the events on days 4, 8, and 12. Furthermore, WTG simulates the persistent rainfall from days 14-16 of the benchmark simulation better than both versions of WPG, which predict almost-daily precipitation events with magnitudes much larger than the benchmark.

3.4.3 Gravity wave resonance

We performed an additional set of simulations based on the SGP case, similar to the time-varying self-consistency tests described above, but instead using time-varying surface fluxes and interactive radiation for both the benchmark and WTG/WPG coupled runs. This is still a self-consistency test, as the benchmark and WTG/WPG coupled runs are subject to the same forcings, but now the SDS scheme must respond to forcings other than column buoyancy anomalies. This framework is perhaps more representative of how WTG and WPG might be used to test CRM's ability to reproduce the properties of the observed atmosphere. One other important difference between these simulations and the SGP simulations described above (and shown in Figure 3.5) is the use of a moister initial condition, which leads to larger magnitude precipitation events in the benchmark and coupled simulations, but should not affect the dynamical resonance we explore in this section.

The results of this experiment are shown in Figure 3.6. Old WPG (middle panel, orange solid line) clearly performs the worst of the three large-scale dynamics parameterizations, with peak precipitation rates more than twice as large as the benchmark case, and, starting around day 12, a series of large rainfall events seemingly unrelated to anything in the benchmark simulation. These wild oscillations are not present in new WPG, and they are the result of the gravity wave resonance mentioned earlier.

Why the resonance?

From the precipitation time series in Figure 3.6, it is clear that new WPG is a substantial improvement over old WPG. This improvement is due to the improved handling of transient disturbances in new WPG; in particular, new WPG eliminates the spurious gravity-wave

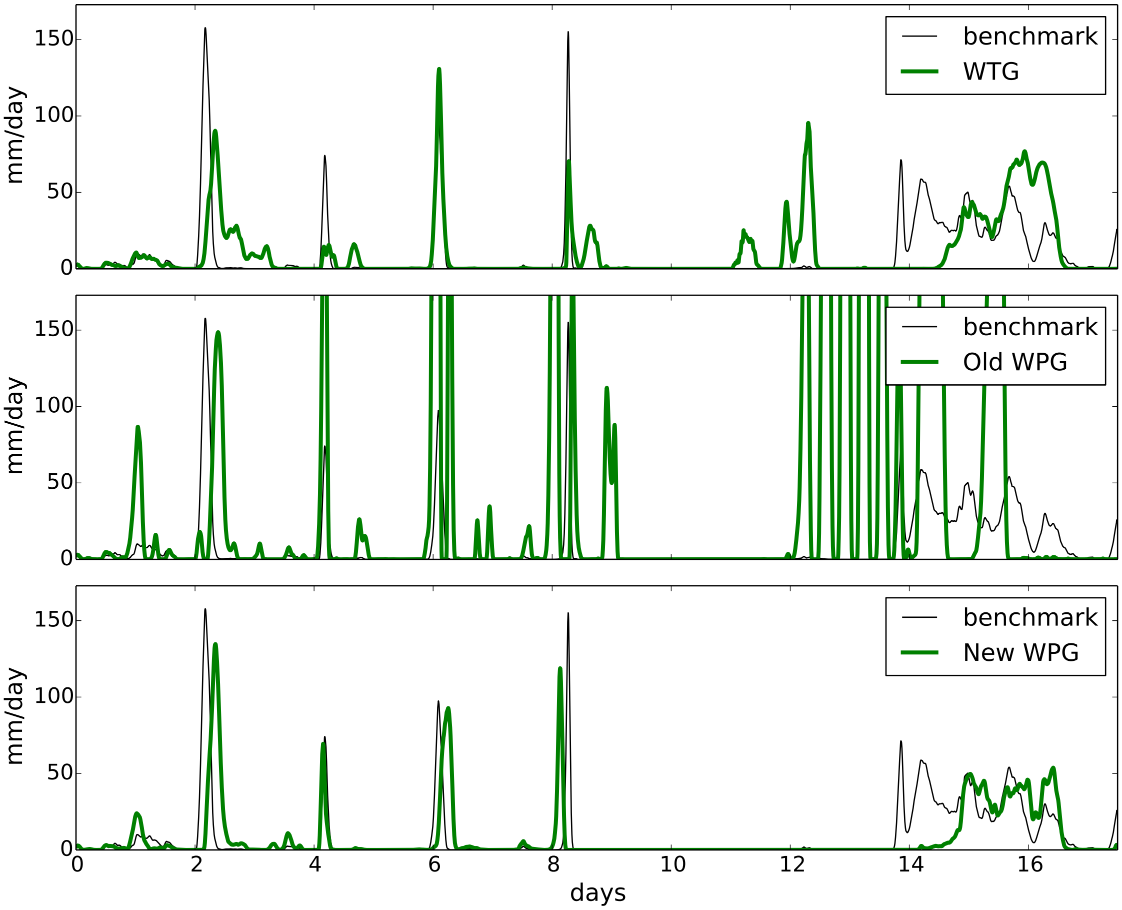

Figure 3.6: Precipitation time series for the SGP case with interactive radiation and time-varying surface and advective forcings. In all panels, the thin black line is the precipitation rate from the benchmark simulation with prescribed w. The thick green lines in all panels show precipitation from the SDS-coupled runs; in the top panel is the precipitation from the simulation coupled to WTG ($\tau = 0.725$ hours); the middle and bottom panels show old WPG and new WPG ($L = 128$ km for both), respectively. Maximum rainfall rate for the old WPG case is 1470 mm/day.

resonance in old WPG, as shown in Chapter 2 and Edman & Romps (2014). The resonance works as follows: a column coupled to old WPG behaves as though a plane wave of wavelength L is passing through the domain; buoyancy anomalies with nearly the same frequency as this wave can trigger a resonance, amplifying the anomaly rather than damping it away. For the shallow-water case considered in Chapter 2 and Edman & Romps (2014), the resonance occurs only at the frequency $f = \omega/(2\pi) = c/(2\pi L)$, where $c = \sqrt{gh}$ is the wave speed in a shallow fluid of depth h. Through a separation of variables, it can be shown that a continuously stratified fluid obeys a set of shallow water equations, each corresponding to a different 'equivalent depth' (e.g., Matsuno 1966). If one imposes a so-called 'rigid lid' somewhere in the atmosphere (i.e., $w \to 0$ at some z), the vertical structure of the stratified fluid can be decomposed into a discrete set of vertical modes, each with a distinct wave speed c. While perhaps not physically realistic, the rigid lid assumption has been justified in the literature (e.g. Mapes 1998) and is often invoked in studies of tropical circulations (e.g., Dias et al. 1983; Haertel & Johnson 1998; Tulich et al. 2007). Because the continuously stratified fluid supports a spectrum of wave speeds and vertical structures, old WPG has the potential for gravity wave resonance at any of the discrete frequencies $f_i = c_i/(2\pi L)$, where c_i is wave speed of the i^{th} vertical mode.

To see this explicitly, consider the Boussinesq equations linearized about a motionless hydrostatic base state. If we use the old WPG approximation, these equations become

$$\begin{aligned} \partial_t b &= -N^2 w + Q && (3.9)\\ \partial_z p &= \rho b && (3.10)\\ \partial_z w &= -\delta && (3.11)\\ \partial_t \delta &= \frac{1}{\rho}\frac{p}{L^2} - \alpha^* \delta\,. && (3.12) \end{aligned}$$

Here, b is the buoyancy, Q is the buoyancy forcing, α^* is a damping term, and δ is the horizontal divergence. Assuming N^2 is constant with height and the dynamics are inviscid ($\alpha^* = 0$), these equations can be reduced to the following equation for the buoyancy:

$$\partial_t^2 \partial_z^2 b - \frac{N^2}{L^2} b \; = \; \partial_t \partial_z^2 Q\,. \tag{3.13}$$

For a forcing of the form $Q = Q_0 e^{i\omega t + imz}$, where ω is the forcing frequency and m is the vertical wavenumber, the solutions for b can take the form $B_0 e^{i\omega t + imz}$. Plugging this into equation (3.13), we find an expression for the amplitude of the buoyancy anomaly B_0:

$$B_0 = -\frac{im^2\omega}{m^2\omega^2 - N^2/L^2} Q_0\,. \tag{3.14}$$

The amplitude B_0 goes to infinity as ω goes to N/mL. Since N/m is the phase speed of a hydrostatic gravity wave with vertical wave number m, we find that the gravity wave resonance occurs at $f = \omega/(2\pi) = c_m/(2\pi L)$, where c_m is the phase speed of the mode with vertical wave number m. Therefore, we expect that the gravity wave resonance in old WPG could manifest at a variety of frequencies and with particular vertical structures, corresponding to the vertical modes m and their associated phase speeds c_m.

In Chapter 2 and Edman & Romps (2014), we showed that new WPG eliminated this gravity-wave resonance in the shallow-water system. Here, we show that new WPG eliminates the gravity wave resonance in a continuously stratified fluid for any vertical mode. The Boussinesq system for new WPG is:

$$\begin{aligned}
\partial_t b &= -N^2 w + Q && (3.15)\\
\partial_z p &= \rho b && (3.16)\\
\partial_z w &= -\delta && (3.17)\\
\partial_t \delta' &= \frac{1}{\rho}\frac{p}{L^2} - \alpha^* \delta' && (3.18)\\
\delta &= \delta' + \frac{2\pi L}{HN}\partial_t \delta' \,. && (3.19)
\end{aligned}$$

The difference between these equations and those for old WPG is the addition of (3.19), which alters δ by a term proportional to the time for a first-baroclinic mode to propagate across a distance L. This incorporates the effect of the gravity wave back-reaction discussed in Chapter 2 and Edman & Romps (2014).

Reducing these equations to a single equation for the buoyancy in the inviscid case ($\alpha^* = 0$), we get

$$\partial_t^2 \partial_z^2 b - \frac{2\pi N}{HL}\partial_t b - \frac{N^2}{L^2} b \;=\; \partial_t \partial_z^2 Q \,. \qquad (3.20)$$

For an oscillating source $Q = Q_0 e^{i\omega t + imz}$ (where ω and m real and nonzero), we search for solutions of the form $b = B_0 e^{i\omega t + imz}$ and find

$$B_0 = -\frac{im^2\omega}{m^2\omega^2 - \frac{2\pi N}{HL} i\omega - \frac{N^2}{L^2}} Q_0 \,. \qquad (3.21)$$

Clearly, there is no combination of real m and real ω that can make the denominator zero. Therefore, there is no resonance for any forcing – i.e., for any frequency and vertical wavenumber – in new WPG.

Vertical mode decomposition

In the above example using constant N^2, the sine functions form an orthogonal basis with which we can expand any vertical profile. For the general case of $N^2(z)$, we can define a set of vertical modes by solving the vertical structure equation,

$$\frac{d^2 W(z)}{dz^2} + \frac{N^2(z)}{c_m^2} W(z) = 0 \,, \qquad (3.22)$$

where $W(z)$ is the vertical structure function for w. Subject to boundary conditions $w = 0$ at the surface and the tropopause, this produces a set of orthogonal eigenfunctions corresponding to discrete wave speeds c_m.

We perform this decomposition for the SGP simulation coupled to old WPG using the mean $N^2(z)$ and placing a rigid lid at the cold-point tropopause ($z = 16.4$ km). The first two vertical modes are plotted on the right side of Figure 3.7. To gain some insight into the wild oscillations beginning around day 12 of the old WPG simulation, we project the vertical profile of w (averaged every 5 minutes) onto these vertical modes; the result is the bottom left panel of Figure 3.7. Compared to the actual w time series from the simulation (top left panel), the first two modes capture the basic features of the oscillation: a shallow (mode 2) circulation leads a deeper (mode 1) circulation, with a frequency of approximately 4 cycles/day.

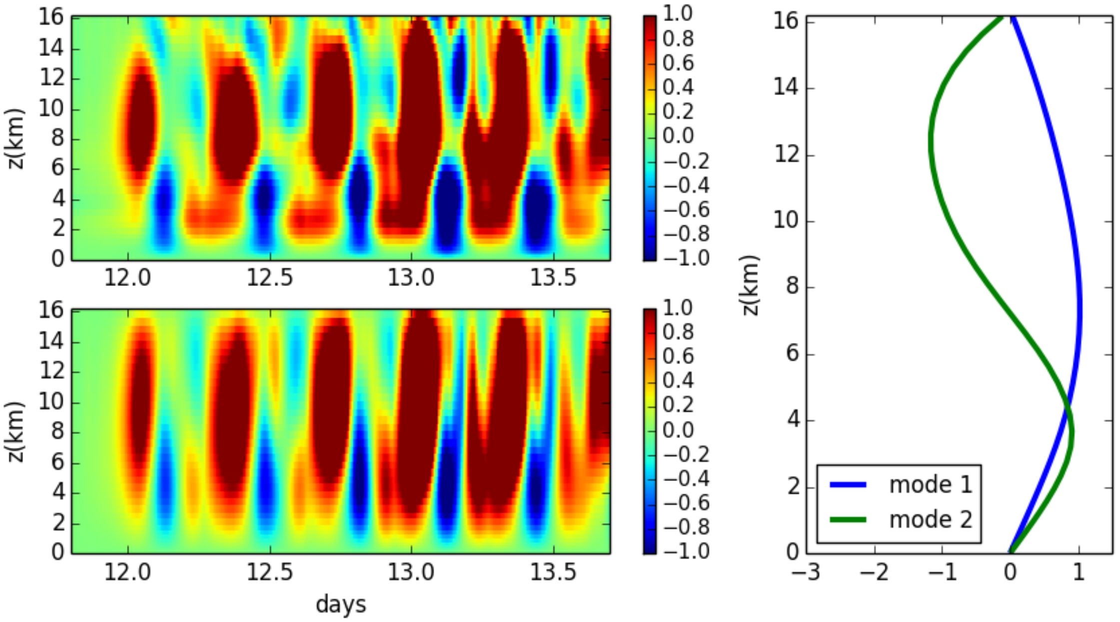

Figure 3.7: (top) Time series of w from the SGP simulation with interactive radiation and time-varying surface and advective forcings coupled to old WPG. (bottom) Projection of w time series onto the first two vertical modes. (right) First two vertical modes with a rigid lid at the tropopause.

The top panel of Figure 3.8 shows the time series of projection coefficients for each of the first four vertical modes. Clearly, most of the amplitude is contained in the first three modes. The bottom panel shows the power spectra of the projection coefficients for the first four vertical modes; the x-axis is rescaled by the factor $2\pi L$ such that it is in units of wave speed. The vertical black lines correspond to the wave speeds of the different vertical modes, e.g., $c_1 = 55.2$ m s^{-1} and $c_2 = 28.2$ m s^{-1}. If the oscillations are indeed caused by the gravity wave resonance in old WPG, then we expect the peaks in the power spectra to align with one or more of these vertical lines. The strongest peak for all modes occurs at c_2, the resonance we would associate with the vertical structure of mode 2. This is consistent with the behavior in Figure 3.7, where the mode 2 circulation appears to trigger the deeper circulation, causing them to oscillate at the same frequency. Mode 1 also has a peak near $c_1 = 55.2$ m s^{-1} and another around 5 m s^{-1}; the peak at c_1 is due to gravity wave resonance with a mode-1 vertical structure, while the peak near 5 m s^{-1} appears to be associated with higher vertical modes.

3.5 Discussion

In this study, we have evaluated three methods for parameterizing large-scale dynamics (SDS schemes) in CRMs, using a self-consistency framework designed to isolate errors introduced by the SDS scheme from errors in the convection simulated by the CRM. WTG, old WPG, and new WPG are all pass RCE self-consistency tests for large τ and L (large-scale environment weakly coupled to the column) and for small τ and L (large-scale environment strongly coupled to the column). For intermediate L, however, old WPG and new WPG exhibit domain-mean descent that is comparable to the radiatively driven clear-sky descent and, therefore, do not pass this part of the self-consistency test.

These mixed results do not necessarily doom the enterprise of parameterizing large-scale dynamics. One notable limitation of the versions of WPG and WTG considered here is that they rely on a single parameter related to the wave speed of a particular baroclinic mode (τ in WTG, β in new WPG); others have suggested that a spectral decomposition approach might be the best way forward (Bergman & Sardeshmukh 2004; Mapes 2004). Herman & Raymond (2014) recently introduced a 'spectral WTG' based on this approach, and new WPG could be extended to a spectral framework as well.

The secondary goal of this study is to evaluate the new form of WPG introduced in Chapter 2 and Edman & Romps (2014), and confirm that it represents a significant advance over prior implementations of WPG. We find that, in a self-consistency test based on observations from TWP-ICE, new WPG simulates the benchmark precipitation time series better than old WPG and WTG, but in a test based on observations from the ARM SGP site, both versions of WPG perform poorly, and WTG performs better than either version WPG.

We also show the traditional version of WPG (e.g. Romps 2012a) is prone to a potentially troublesome gravity wave resonance, where buoyancy anomalies near the natural frequency of the column are amplified rather than damped away. In another set of self-consistency tests based on the ARM SGP observations (Figure 3.6), which use interactive radiation and time-varying surface and advective forcings, we find that old WPG is severely affected by this gravity-wave resonance, and that the new version of WPG eliminates this resonance and simulates precipitation time series better than old WPG. As a result, we find that this gravity-wave resonance can pose a significant problem in observationally-based experiments, but we confirm the new version of WPG does not suffer from this deficiency.

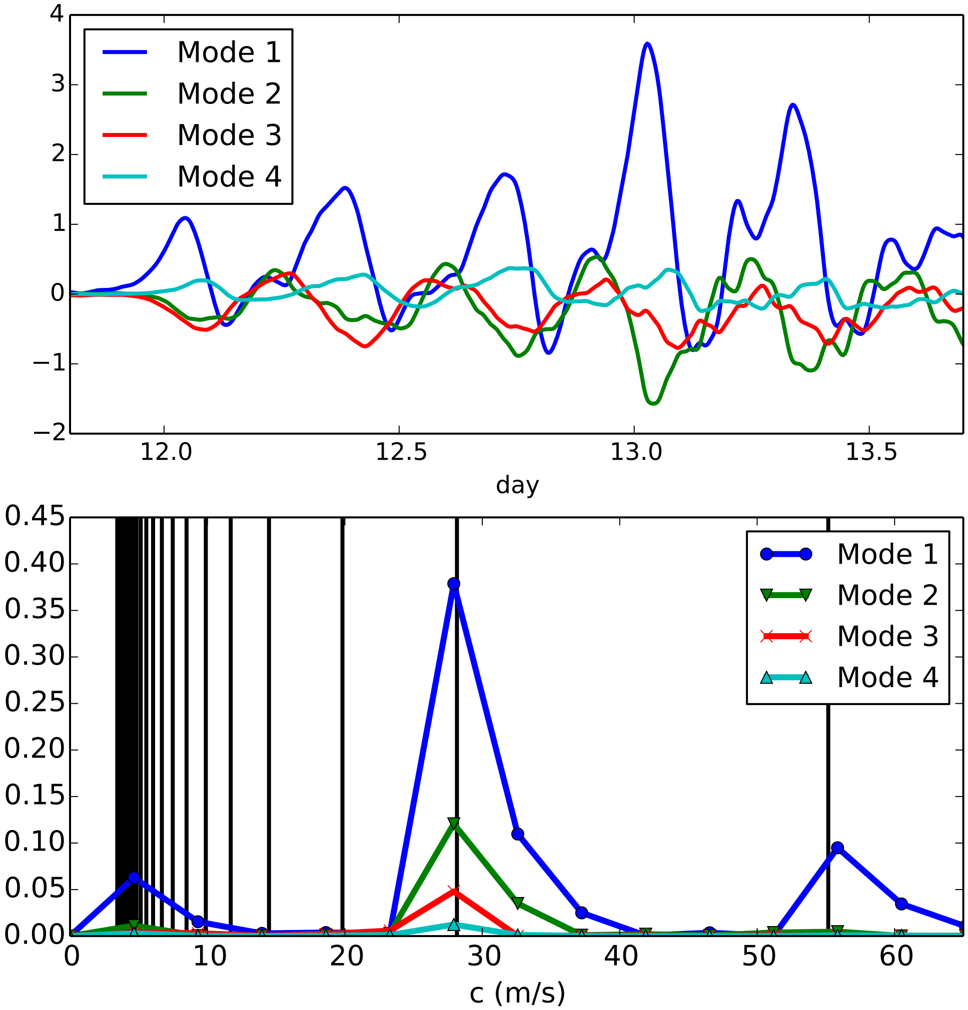

Figure 3.8: (top) Time series of projection coefficient for the first four vertical normal modes. (bottom) Power spectra for the time series of projection coefficients for the first four vertical modes. The x-axis has been rescaled to be in units of wave speed; the black vertical lines correspond to the wave speeds of the vertical modes.

Chapter 4

Beyond the rigid lid: Baroclinic modes in a structured atmosphere[1]

The baroclinic-mode decomposition is a fixture of the tropical-dynamics literature due to its simplicity and apparent usefulness in understanding a wide range of atmospheric phenomena. However, its derivation relies on the assumption that the tropopause is a rigid lid, which artificially restricts the vertical propagation of wave energy. This causes tropospheric buoyancy anomalies of a single vertical mode to remain coherent for all time in the absence of dissipation. Here, we derive the Green's functions for these baroclinic modes in a two-dimensional troposphere (or, equivalently, a three-dimensional troposphere with one translational symmetry) that is overlain by a stratosphere. These Green's functions quantify the propagation and spreading of gravity waves generated by a horizontally localized heating, and they can be used to reconstruct the evolution of any tropospheric heating. For a first-baroclinic two-dimensional right-moving or left-moving gravity wave with a characteristic width of 100 km, its initial horizontal shape becomes unrecognizable after 4 hours, at which point its initial amplitude has also been reduced by a factor of $1/\pi$. After this time, the gravity wave assumes a universal shape that widens linearly in time. For gravity waves on a periodic domain the length of Earth's circumference, it takes only 10 days for the gravity waves to spread their buoyancy throughout the entire domain.

4.1 Introduction

Much of the atmospheric tropical-dynamics literature has relied on spectrally-discretized and truncated models that reduce the primitive equations to a set of shallow-water equations for the first one or two baroclinic modes (e.g., Matsuno 1966; Gill 1980; Neelin & Held 1987; Mapes 1993). This class of simple models is capable of replicating important aspects of the tropical atmospheric circulation. For example, some studies (e.g., Wheeler & Kiladis

---

[1] **Material in this chapter originally published in Edman & Romps (2017), © Copyright 2017 AMS.**

1999; Hendon & Wheeler 2008) have documented features in the tropical spectra of outgoing longwave radiation that appear quite similar to the linear equatorial waves predicted by Matsuno (1966). Others (e.g., Gill 1980; Neelin & Held 1987) have constructed simple models that capture many of the observed features of steady tropical circulations using only the first baroclinic mode.

The spectral discretization used by these simple models is only formally justified if the tropopause behaves like a rigid lid, and the spectral truncation to the first one or two modes is valid only if the heating has a particularly simple structure. It has indeed been observed that the first one or two baroclinic modes dominate diabatic heating profiles in the tropical troposphere, at least around mesoscale convective systems (Mapes & Houze 1995). Past work often interprets first and second baroclinic-mode heating as corresponding to deep-convective and stratiform clouds, respectively (e.g., Mapes 2000; Haertel & Kiladis 2004). However, the tropopause is far from being a rigid lid, and, in a semi-infinite atmosphere, any heat source confined to the troposphere excites waves with a continuous spectrum of vertical structures, even if the heating is dominated by a single baroclinic mode (Pandya et al. 1993; Mapes 1998; Lindzen 2003).

A further objection to this spectral discretization and truncation comes from considering the response to transient heating in a model with a rigid lid. Bretherton & Smolarkiewicz (1989) introduced the canonical description of gravity-wave adjustment in a non-rotating fluid, in which wave fronts of compensating subsidence propagate away from the heat source at discrete gravity-wave speeds corresponding to each baroclinic mode. This model has proved useful for understanding how convective clouds may initiate convection in their local environments (Mapes 1993), and for parameterizing the interaction of convection and large-scale circulations (e.g., Raymond & Zeng 2000; Cohen & Craig 2004; Edman & Romps 2014). However, this picture of purely horizontal wave radiation is at best incomplete: it predicts that wave fronts produced by a pulse of heating will propagate forever unless there is some dissipation in the system. In order to prevent this pathological behavior, simple models based on one or two baroclinic modes often invoke strong damping in the form of Rayleigh friction and Newtonian cooling, with timescales of about 1-10 days (e.g., Matsuno 1966; Chang 1977; Gill 1980; Wu et al. 2000; Sobel et al. 2001; Sugiyama 2009; Chan & Shepherd 2014). Some have found this need for strong damping unsettling (e.g., Battisti et al. 1999), but recent work has suggested that it could be produced by convective momentum transport (Lin et al. 2008; Romps 2014).

As other studies have pointed out (e.g., Pandya et al. 1993), the upward radiation of wave energy modifies the rigid-lid picture, smoothing out sharp wave fronts that would otherwise propagate forever in the absence of any dissipative friction or radiation. This diffusion of sharp wave fronts occurs because the vertical component of the group velocity for hydrostatic gravity waves is proportional to the horizontal wavenumber. Therefore, the largest horizontal wavenumbers are the first to radiate out of the troposphere (Gill 1982), rapidly smoothing out any sharp features in the tropospheric gravity wave. Eventually, all of the nonzero horizontal wavenumbers radiate into the stratosphere, leaving the troposphere with a non-propagating, horizontally uniform buoyancy anomaly.

Some studies have suggested that internal gravity waves radiate out of the troposphere on timescales relevant to dynamics. Mapes (1998) attempted to parameterize the smoothing of wavefronts emanating from a mesoscale convective system using a Gaussian kernel. And, Yano & Emanuel (1991) found that upward radiation of wave energy suppresses the growth of the wind-induced surface heat exchange (WISHE) instability for all but the longest equatorial modes.

In another study, Chumakova et al. (2013, henceforth CRT) found a set of exponentially decaying solutions to the linearized two-dimensional Boussinesq equations in a layer of fluid with constant buoyancy frequency N_1 (i.e., the troposphere) overlain by a layer of fluid with a buoyancy frequency N_2 greater than N_1 (i.e., the stratosphere). We will refer to these exponentially decaying solutions as CRT modes. A single CRT mode of buoyancy (from equations 17 and 18 of CRT) can be written as[2]

$$b_{k,m}^{\mathrm{CRT}}(x,z,t) = \begin{cases} b_0 \sin(mz) \exp\left[-i\frac{N_1|k|}{m}t + ikx\right] & z \le H \\ b_0 \frac{N_2^2}{N_1^2} \sin(mH) \exp\Big[- i\frac{N_1|k|}{m}t \\ \qquad +ikx - i\frac{N_2}{N_1}m(z-H)\Big] & z > H \end{cases}, \quad (4.1)$$

where

$$m = \frac{n\pi + i\tanh^{-1}(N_1/N_2)}{H} \quad (4.2)$$

is a complex vertical wavenumber, n is an integer, k is a horizontal wavenumber, H is the height of the tropopause, and b_0 is a constant with dimensions of buoyancy. This buoyancy distribution can be generated at time $t=0$ in an initially quiescent atmosphere by applying a heating of $Q = b_{k,m}^{\mathrm{CRT}}(x,z,0)\delta(t)$, where δ is the Dirac delta function. The resulting pattern of buoyancy propagates horizontally with speed $\mathrm{Re}(N_1/m)$ and decays exponentially with an e-folding time of $-1/\mathrm{Im}(N_1|k|/m)$.

In principle, the CRT modes can be used to construct solutions to some initial-value problems, but there are a host of problems with this approach: the CRT modes do not have the same vertical structure as rigid-lid normal modes; the CRT modes are not orthogonal; the CRT modes are divergent in the $N_2 = N_1$ limit; the buoyancy in the initial state of each CRT mode is not confined to the troposphere; and the energy density of each CRT mode grows exponentially without bound as you move upwards in the stratosphere. The unboundedness is essential to how the CRT modes work: the CRT modes are constructed to decay exponentially in time, but, to have an upward-propagating pattern of gravity waves in the stratosphere that decays exponentially with time, the pattern must grow exponentially with height.

---

[2] There are a couple of typos in equation 18 of CRT. The expressions for ρ_n and p_n are missing factors of $i\rho_0$ and $i\rho_0 N_1^2$, respectively. In equation (4.4), we have also extended the CRT modes into the stratosphere by enforcing continuity of $(1/N^2)\partial_t b$ and $(1/N^2)\partial_z\partial_t b$ at $z = H$, which guarantee continuity of u and w.

Another way in which the CRT modes are unphysical is that they fail to generate a steady state in response to a steady tropospheric heating. In a 2D Boussinesq fluid at rest, the response to a steady heating is steady and finite within an ever-expanding region centered at the location of the heating. To see that the CRT modes do not achieve this state, first consider the heating

$$Q(x,z,t) = \begin{cases} B_0 \sin(mz)\delta(x)\delta(t) & z \leq H \\ B_0 \frac{N_2^2}{N_1^2} \sin(mH) \exp\Big[- i \frac{N_2}{N_1} m(z-H) \Big] \delta(x)\delta(t) & z > H \end{cases} , \quad (4.3)$$

where m is defined as in equation (4.2) with integer n. Here and throughout, we will use a lowercase b to denote a buoyancy (with units of m s^{-2}), an uppercase B to denote a horizontally integrated buoyancy (m^2 s^{-2}), and Q to denote a heating or, in other words, a tendency of buoyancy (m s^{-3}). Since the Fourier transform of $\delta(x)$ is $1/\sqrt{2\pi}$, this buoyancy evolves as

$$b_m^{\mathrm{CRT}}(x,z,t) = \frac{B_0}{2\pi b_0} \int_{-\infty}^{\infty} dk \, b_{k,m}^{\mathrm{CRT}}(x,z,t)$$
$$= \begin{cases} \frac{B_0}{2\pi} \mathrm{Im} \left\{ \sin(mz) \left[\frac{1}{N_1 t/m + x} + \frac{1}{N_1 t/m - x} \right] \right\} & z \leq H \\ \frac{B_0}{2\pi} \frac{N_2^2}{N_1^2} \mathrm{Im} \Big\{ \sin(mH) e^{-i \frac{N_2}{N_1} m(z-H)} & \\ \qquad \times \left[\frac{1}{N_1 t/m + x} + \frac{1}{N_1 t/m - x} \right] \Big\} & z > H \end{cases} . \quad (4.4)$$

This solution has a left-moving pulse of buoyancy and a right-moving pulse of buoyancy that both smear out with time. As with the single-k solution in equation (4.1), this has an energy density that grows exponentially with height in the stratosphere. This behavior was baked in by the heating in equation (4.3), which had to be chosen that way in order to make use of the CRT modes. When integrated horizontally and temporally, that heating grows exponentially with height in the stratosphere.

From this solution, we can find the solution to a heating that has the same spatial structure as (4.3), but has a Heaviside unit step function of time $\mathcal{H}(t)$ instead of a $\delta(t)$, i.e., the heating is switched on at $t = 0$ and held on. The solution to this is $\int_0^t dt' \, b_m^{\mathrm{CRT}}(x,z,t')\mathcal{H}(t)$, which is proportional to $\log\left[1 - (N_1 t/mx)^2\right]$, which grows logarithmically without bound. Since this behavior occurs for any m satisfying (4.2), the CRT modes do not admit any steady-state solutions to a steady heating.

The left panel of Figure 4.1 illustrates this pathology for an $n = 1$ heating (closely approximating a first-baroclinic structure in the troposphere) of the form in equation (4.3) with $\delta(t)$ replaced with $\mathcal{H}(t)$. The values of H, N_1, and N_2 are chosen to be representative of the tropical atmosphere. Based on Figure 4.2, which shows the mean of 3-hourly soundings

Table 4.1: Unless otherwise specified, throughout the chapter we will default to these parameter values, which are typical for Earth's tropics.

Parameter	Symbol	Value
Buoyancy frequency in the troposphere	N_1	0.01 s^{-1}
Depth of the troposphere	H	17 km
Stratification ratio	N_2/N_1	2.5

from the Department of Energy's Atmospheric Radiation Measurement (ARM) site in Darwin, Australia from January 18 to February 3, 2006, these values are set to $H = 17$ km, $N_1 = 0.01$ s^{-1} and $N_2 = 0.025$ s^{-1} here and throughout the chapter. For ease of reference, these values are printed in Table 4.1. In the left panel of Figure 4.1, each colored line plots the time series of mid-tropospheric buoyancy at a specific distance from the origin. For example, the darkest blue curve is the buoyancy at $x = 10$ km, which will feel the leading edge of the gravity wave pass over it at a normalized time of $\text{Re}(N_1/m)t = 10$ km. The darkest red curve is the buoyancy at $x = 100$ km, which will feel the leading edge of the gravity wave pass over it at a normalized time of $\text{Re}(N_1/m)t = 100$ km. If these solutions behaved as expected from rigid-lid thinking, then the buoyancy at each of these locations would plateau at a value of $2\text{Re}(N_1/m)/B_0$ shortly after the wave front has passed. Instead, the buoyancy at all of these locations continues to rise logarithmically. This undesirable behavior is a consequence of the stratospheric heating that is baked into the CRT modes. As we will see in section 4.2.4, steady heating that is confined to the troposphere generates a steady buoyancy field.

In this study, we take a different approach than CRT. Rather than seek a set of vertical modes for an atmosphere without a rigid lid at the tropopause, we solve the initial-value problem directly. In section 4.2, we derive a Green's function for a pulse of buoyancy in the troposphere with baroclinic vertical structure for the simplest atmosphere without a rigid lid at the tropopause: the two-dimensional, non-rotating Boussinesq equations with two layers of constant but differing stratification. In the subsequent sections, we explore how this simple change to a more realistic upper boundary condition results in buoyancy anomalies that quickly spread out as they propagate, in stark contrast to the rigid-lid case.

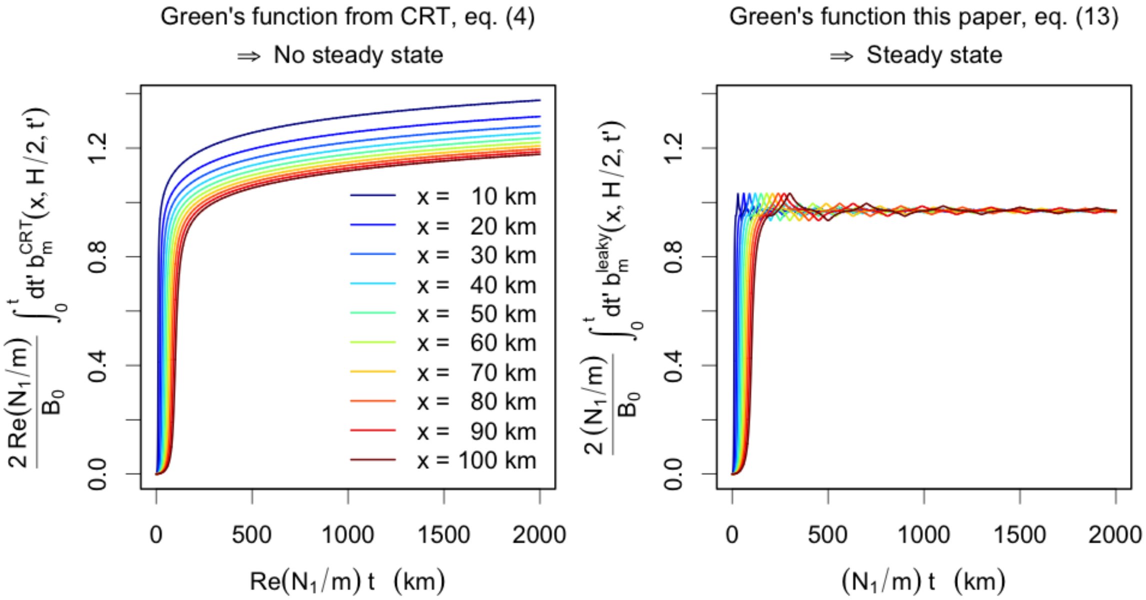

Green's function from CRT, eq. (4)
⇒ No steady state

Green's function this paper, eq. (13)
⇒ Steady state

Figure 4.1: (left) The time series of mid-tropospheric buoyancy for a variety of distances from the origin, ranging from 10 to 100 km, for a steady $n = 1$ heating (approximating a first baroclinic mode in the troposphere) that is held on for all $t > 0$, which is obtained by integrating the CRT Green's function in equation (4.4). The time on the abscissa is normalized by the propagation speed of the wave front, $\mathrm{Re}(N_1/m)$. The buoyancies on the ordinate are normalized by $2\mathrm{Re}(N_1/m)/B_0$, which is naively the value to which the mid-tropospheric buoyancy would asymptote shortly after the wave front passes. (right) Same, but for the Green's function presented in equation (4.13).

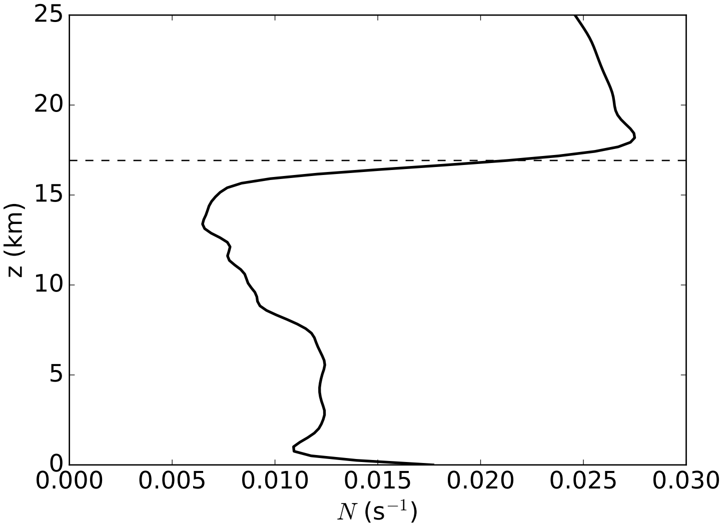

Figure 4.2: Mean profile of the Brunt-Väisäilä frequency N calculated from soundings taken every 3 hours at the Darwin ARM site from January 18, 2006 to February 3, 2006. The dashed line denotes the cold-point tropopause at 16.9 km.

4.2 The leaky-lid Green's function

The Boussinesq equations describing hydrostatic linear perturbations to a two-dimensional, nonrotating, stratified fluid at rest are

$$\partial_t u = -\frac{\partial_x p}{\rho_0} \tag{4.5a}$$

$$0 = -\frac{\partial_z p}{\rho_0} + b \tag{4.5b}$$

$$\partial_t b = -N^2 w + Q \tag{4.5c}$$

$$0 = \partial_x u + \partial_z w\,, \tag{4.5d}$$

where u is the horizontal speed, w is the vertical speed, ρ_0 is a constant density, p is the pressure perturbation, b is the buoyancy, and Q is the buoyancy source or, in other words, the heating. Let N be piecewise constant in height such that

$$N = \begin{cases} N_1 & 0 \le z \le H \\ N_2 & H < z \end{cases}\,, \tag{4.6}$$

where H is the tropopause. When $N_2 > N_1$, this is a simple analogue for Earth's atmosphere in which the troposphere is capped by the more stratified stratosphere. The derivation in section 4.2.4, however, applies equally well to any value of N_2/N_1 from zero to infinity.

In the following subsections, we will review the Green's functions for a troposphere with a rigid lid ($N_2 = \infty$) and a troposphere with no lid ($N_2 = N_1$), and then present the Green's function for a troposphere with a leaky lid ($N_1 < N_2 < \infty$), which, as we will see, connects the rigid-lid and no-lid limits. To derive any of these Green's functions, we write the set of Boussinesq equations (4.5) as a wave equation for b,

$$\partial_t^2 \partial_z^2 b + N^2 \partial_x^2 b = \partial_t \partial_z^2 Q \,, \tag{4.7}$$

and we seek a solution for a baroclinic tropospheric heating of the form

$$Q(x, z, t) = B_0 \sin(mz) \mathcal{H}(H - z) \delta(x) \delta(t) \,, \tag{4.8}$$

where B_0 is a constant, H is the depth of troposphere, and m is taken to be one of the baroclinic modes, i.e., $m = n\pi/H$ where n is an integer.

4.2.1 Green's function for a rigid lid

To begin, we reproduce the well-known solution for an atmosphere with a rigid lid at the tropopause, which corresponds to $N_2 = \infty$. The rigid lid requires $w = 0$ at $z = H$, so we can formally decompose the solutions to (4.7) into a set of vertical normal modes with discrete eigenvalues. This decomposition gives the traditional baroclinic modes, or rigid-lid modes, which are sines (for b and w) and cosines (for p and u) with nodal or anti-nodal points at the surface and tropopause (Gill 1982). Each baroclinic mode is governed by a set of shallow-water equations with wavespeed N_1/m, where m is the eigenvalue corresponding to a particular baroclinic mode.

For a troposphere with a rigid lid, the Green's function – i.e., the solution to (4.7) for a baroclinic pulse specified by equation (4.8) – is

$$b_m^{\text{rigid}}(x, z, t) \;=\; \frac{B_0}{2}\Big[\delta(N_1 t/m \,+\, x) \,+\, \delta(N_1 t/m \,-\, x)\Big] \,\times\, \mathcal{H}(t) \sin(mz) \mathcal{H}(H \,-\, z) \,. \tag{4.9}$$

This describes two delta-function pulses of buoyancy propagating to the left and right with the same baroclinic vertical structure as the forcing. The nature of this solution follows directly from the discrete spectrum of vertical modes for a layer of fluid with a rigid lid. By design, the source specified by equation (4.8) excites exactly one of the normal modes of this system, which travels with a constant horizontal wave speed $c = N_1/m$. In the absence of dissipation, these pulses will propagate forever.

4.2.2 Green's function for no lid

Next, consider a troposphere with no lid, which corresponds to $N_2 = N_1$. In this case, the Green's function – i.e., the solution to (4.7) for a baroclinic pulse specified by equation (4.8) –

was found by Pandya et al. (1993) to be

$$b_m^{\text{no lid}}(x,z,t) = \frac{B_0}{2\pi}\cos(mH)\sin\left(HN_1t/x\right)\sin\left(N_1tz/x\right) \times \left[\frac{1}{N_1t/m+x}+\frac{1}{N_1t/m-x}\right]. \tag{4.10}$$

Despite the appearance of singularities at $x = \pm N_1t/m$, the solution is smooth there; at those locations, the divergence from the $1/(N_1t/m \pm x)$ terms is canceled by the $\sin(HN_1t/x)$ term since m is an integer multiple of π/H. The two pulses of buoyancy propagate horizontally at the same speed as in the rigid-lid case, but they spread out into smooth blobs rather than retaining their delta-function shape.

Another notable difference from the rigid-lid solution is the complex vertical structure of the buoyancy field. Unlike the rigid-lid solution, which has the same vertical structure as the heating, the no-lid buoyancy field projects onto every baroclinic mode: the buoyancy is not all of the same baroclinicity as the heating. This reflects the fact that the baroclinic modes are not the vertical eigenfunctions of the system when the rigid lid is raised beyond the tropopause. In fact, when there is no lid at all, as in this case, the eigenvalue spectrum becomes continuous. The relationship between the continuous and discrete spectra is precisely that of the continuous and discrete Fourier transforms. As the spatial domain increases in size, the discrete transform approaches the continuous one. Despite this, the linearized governing equations (4.5) require that the horizontally-integrated buoyancy maintains the same baroclinic structure as the source for all time, regardless of N_2. For example, in the case of a first-baroclinic source, the horizontally-integrated buoyancy is first-baroclinic for all time. This property can most easily be seen by integrating equation (4.5c) over x and noting that the integral of w over x must be zero by continuity. Remarkably, it can be confirmed numerically that the horizontal integral of $b_m^{\text{no lid}}$ equals $B_0\sin(mz)\mathcal{H}(H-z)$.

To get a quantitative sense of how the no-lid solution compares to the rigid-lid solution, consider the buoyancy at $x = \pm N_1t/m$, which are the centers of the propagating pulses. Taking the limit of equation (4.10) as $|x| \to N_1t/m$, we find

$$b_m^{\text{no lid}}(\pm N_1t/m, z, t) = \frac{B_0m^2H}{2\pi N_1t}\sin(mz)\,. \tag{4.11}$$

Note that all of the buoyancy at $x = \pm N_1t/m$ is contained in the same vertical mode m as the initial perturbation. Note, also, that the amplitude goes as $1/t$. Since the horizontally-integrated buoyancy is constant and projects only onto the baroclinic mode of the source, this implies that the width of the left-moving or right-moving pulse is proportional to t; more specifically, its width is approximately $\pi N_1t/m^2H$.

In summary, the one-way propagating buoyancy pulses can be described as propagating at a constant speed of $c = N_1/m$ at their center and with edges that spread away from each center at a speed of $\pi N_1/2m^2H = (\pi/2mH)c$. We will see in section 4.2.4 how this is modified for $N_2 > N_1$.

4.2.3 Simple model for the decay of amplitude

What causes the pulses of buoyancy to decay in amplitude and spread out? It is illuminating to think of the counter-propagating pulses of buoyancy as packets of internal gravity waves propagating away from the source. Without a rigid lid at the tropopause, internal gravity waves can propagate out of the troposphere. The vertical group velocity for internal gravity waves is proportional to the horizontal wavenumber, which means that shorter waves radiate out of the troposphere faster than longer waves. It is this process that causes the dispersal of the initial delta functions noted above. After a sufficiently long time, all that remains is a non-propagating, horizontally-uniform buoyancy anomaly in the troposphere. Note that the net heating to the troposphere is the same whether or not there is a rigid lid at the tropopause: wave energy can propagate upward, but the buoyancy is still confined to the troposphere.

We can construct a simple model for the decay in amplitude at $|x| = N_1 t/m$ by considering the upward radiation of gravity waves. From the dispersion relation for hydrostatic gravity waves defined by (4.7), we find that $\omega = N_1|k|/m$, where k is the horizontal wavenumber, so the horizontal speed of a hydrostatic gravity wave is $c_x = N_1/m$, and the vertical group velocity of a hydrostatic gravity wave is $c_{gz} = N_1|k|/m^2$. A natural timescale τ_k for a gravity wave of horizontal wavenumber k to radiate up and out of the troposphere is the depth of the troposphere H divided by the vertical group velocity, or

$$\tau_k = \frac{m^2 H}{N_1|k|}\,. \tag{4.12}$$

Therefore, we posit that the amplitude of a plane wave of buoyancy in the troposphere decays like $\exp(-t/\tau_k)$.

For a buoyancy pulse that begins as a delta function in x, we can approximate the evolution of the resulting counter-propagating buoyancy pulses (or wave packets) by modifying the rigid lid solution (4.9) to include this exponential decay of gravity waves. Taking the Fourier transform of equation (4.9) yields

$$\tilde{b}_m^{\text{rigid}}(k,z,t) \;=\; \frac{1}{\sqrt{2\pi}}\int_{-\infty}^{\infty} dx\, e^{ikx} b_m^{\text{rigid}}(x,z,t) \;=\; \frac{B_0}{2\sqrt{2\pi}}\left(e^{ikN_1t/m} + e^{-ikN_1t/m}\right)\sin(mz)\,.$$

We can approximate the decay of gravity waves that occurs in the no-lid atmosphere by multiplying this Fourier-transformed rigid-lid solution by $\exp(-t/\tau_k)$, i.e.,

$$\tilde{b}_m^{\text{no lid}}(k,z,t) \approx \frac{B_0}{2\sqrt{2\pi}}\left(e^{ikN_1t/m} + e^{-ikN_1t/m}\right) e^{-t/\tau_k}\sin(mz)\,.$$

Since $1/\tau_k$ is proportional to $|k|$, this modification does not alter the horizontally-integrated buoyancy, which is contained in the $k = 0$ mode. By performing an inverse Fourier transform evaluated at $|x| = N_1 t/m$, we get

$$\begin{aligned} b_m^{\text{no lid}}(\pm N_1 t/m, z, t) &\approx \frac{1}{\sqrt{2\pi}} \int_{-\infty}^{\infty} dk\, e^{\pm ikN_1 t/m} \tilde{b}_m^{\text{no lid}}(k, z, t) \\ &= \frac{1 + 2m^2H^2}{1 + 4m^2H^2} \frac{B_0 m^2 H}{\pi N_1 t} \sin(mz) \approx \frac{B_0 m^2 H}{2\pi N_1 t} \sin(mz)\,, \end{aligned}$$

which is the expression previously derived in equation (4.11). This confirms (4.12) as the approximate residence timescale for plane waves in the troposphere.

4.2.4 Green's function for a leaky lid

Having explored the limiting cases of a rigid lid and no lid, we can turn to our goal of deriving the Green's function for the case of a troposphere with a leaky lid, which corresponds to $N_1 < N_2 < \infty$. For details of the derivation, see Appendix A. The Green's function – i.e., the solution to (4.7) for a baroclinic pulse specified by equation (4.8) – is found to be

$$b_m^{\text{leaky}}(x, z, t) = \begin{cases} \frac{B_0}{2\pi} \frac{\cos(mH)\sin(HN_1t/x)}{\frac{N_1}{N_2} + \left(\frac{N_2}{N_1} - \frac{N_1}{N_2}\right)\sin^2(HN_1t/x)} \\ \quad \times \left[\frac{1}{N_1t/m+x} + \frac{1}{N_1t/m-x}\right] \\ \quad \times \sin\left(N_1tz/x\right) \\ \hfill \text{for } z \le H \\ \\ \frac{B_0}{2\pi} \frac{\cos(mH)\sin(HN_1t/x)}{\frac{N_1}{N_2} + \left(\frac{N_2}{N_1} - \frac{N_1}{N_2}\right)\sin^2(HN_1t/x)} \\ \quad \times \left[\frac{1}{N_1t/m+x} + \frac{1}{N_1t/m-x}\right] \frac{N_2}{2N_1} \Bigg\{ \\ \qquad \left(\frac{N_2}{N_1} + 1\right) \sin\left[\frac{N_1tz}{x} + \left(\frac{N_2}{N_1} - 1\right)\frac{N_1t(z-H)}{x}\right] \\ \quad + \left(\frac{N_2}{N_1} - 1\right) \sin\left[\frac{N_1tH}{x} + \frac{N_2t(H-z)}{x}\right] \Bigg\} \\ \hfill \text{for } z > H \end{cases} . \tag{4.13}$$

This solution is valid over the full range of N_2/N_1, from 0 to ∞, which means that it encompasses both the rigid-lid and no-lid solutions. When $N_2/N_1 = 1$, b_m^{leaky} equals $b_m^{\text{no lid}}$, i.e., it gives the solution for constant N from equation (4.10). In the limit of $N_2/N_1 \to \infty$, $b_m^{\text{leaky}} = b_m^{\text{rigid}}$, i.e., it gives the solution for a rigid-lid tropopause from equation (4.9).

Figure 4.3 compares the no-lid solution ($N_1 = N_2 = 0.01$ s^{-1}) and the leaky-lid solution ($N_1 = 0.01$ s^{-1} and $N_2 = 0.025$ s^{-2}) at $t = 1$ hour in response to the tropospheric heating in equation (4.8) with $H = 17$ km, $m = \pi/H$, and $B_0 = 1$ m^2 s^{-2}. Compared to the no-lid solution, the first-baroclinic gravity waves are more coherent in the troposphere, i.e., they are more compact in the horizontal and have higher peak buoyancies. At the tropopause, there is a discontinuity in buoyancy at the tropopause due to the discontinuity of N^2 in equation

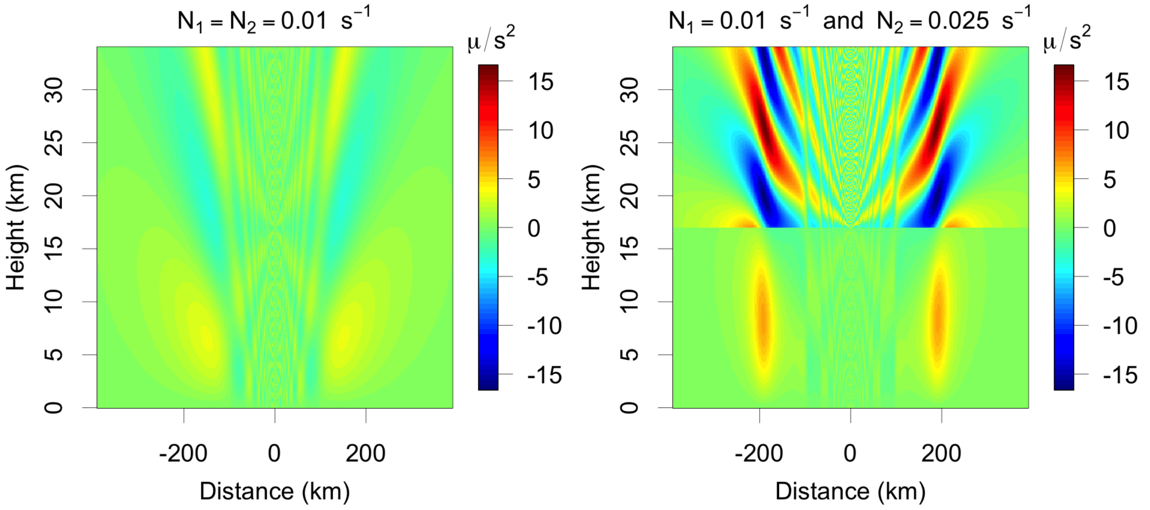

Figure 4.3: (left) The no-lid solution $b_m^{\text{no lid}}$ at $t = 1$ hour in an atmosphere with $N_1 = N_2 = 0.01$ s^{-1} that was subjected to the heating given by equation (4.8) with $H = 17$ km, $m = \pi/H$, and $B_0 = 1$ m^2 s^{-2}. (right) Same, but for b_m^{leaky} with $N_1 = 0.01$ s^{-1} and $N_2 = 0.025$ s^{-1}.

(4.5c). In the stratosphere, the oscillations in buoyancy have a vertical wavelength that is shorter by the factor N_1/N_2, and their amplitude is greater. As with the no-lid solution, it can be confirmed that the leaky-lid solution has the following properties: b_m^{leaky} satisfies (4.7) with $Q = 0$ for all $t > 0$; $(1/N^2)\partial_t b_m^{\text{leaky}}$ and $(1/N^2)\partial_z\partial_t b_m^{\text{leaky}}$ are continuous across the tropopause, guaranteeing continuity of u and w there; the horizontal integral of b_m^{leaky} equals $B_0 \sin(mz)\mathcal{H}(H - z)$; and b_m^{leaky} is zero for all $|x| > 0$ at $t = 0$.

Although t appears in several places in equation (4.13), the temporal evolution of b_m^{leaky} is surprisingly simple. Defining $\hat{x} = mx/N_1 t$, we can write b_m^{leaky} as

$$\begin{aligned} b_m^{\text{leaky}}&(x,z,t) \\ &= \frac{B_0 m}{2\pi N_1 t}\frac{\cos(mH)\sin(mH/\hat{x})\sin(mz/\hat{x})}{\frac{N_1}{N_2}+\left(\frac{N_2}{N_1}-\frac{N_1}{N_2}\right)\sin^2(mH/\hat{x})} \\ &\qquad\times\left[\frac{1}{1+\hat{x}}+\frac{1}{1-\hat{x}}\right] \qquad \text{for } z \le H\,. \end{aligned} \tag{4.14}$$

Writing b_m^{leaky} in this way makes clear that the shape of the buoyancy distribution is invariant in time: the buoyancy distribution simply stretches out linearly in time (i.e., position $\hat{x}$ in the distribution travels away from the origin at speed $\hat{x}N_1/m$) as its overall amplitude decreases as $1/t$. Therefore, one plot of b_m^{leaky} is sufficient to illustrate its evolution for all time.

Plots of b_m^{leaky} are shown in the top row of Figure 4.4 for cases of, from left to right: no lid and first baroclinic ($N_2/N_1 = 1$ and $m = \pi/H$); no lid and second baroclinic ($N_2/N_1 = 1$ and $m = 2\pi/H$); leaky lid and first baroclinic ($N_2/N_1 = 2.5$ and $m = \pi/H$); and leaky lid

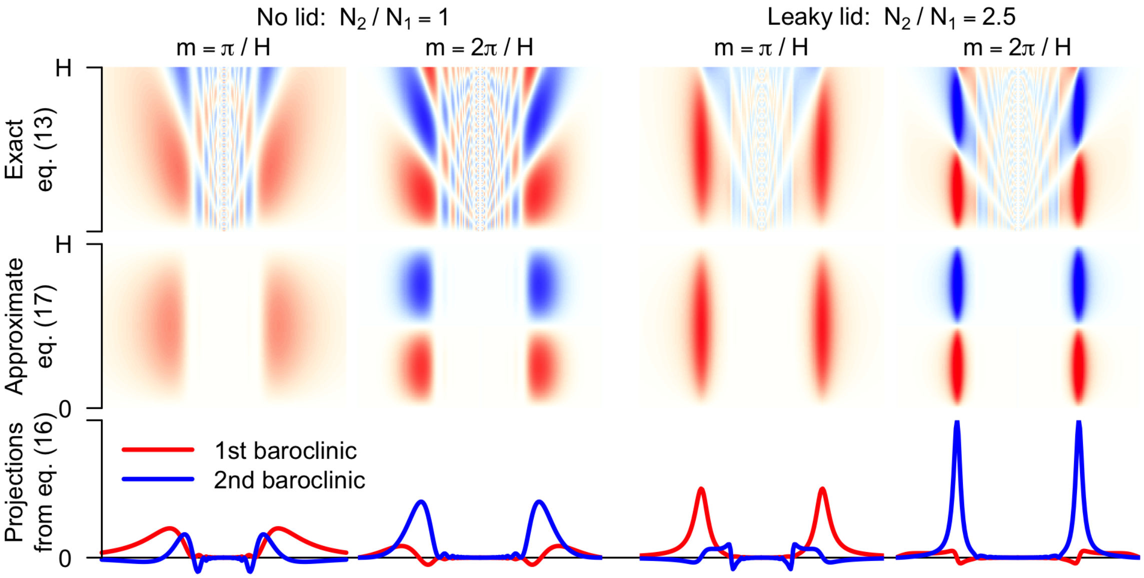

Figure 4.4: (top row) The Green's function b_m^{leaky} in equation (4.13) for all combinations of $N_2/N_1 \in (0, 1)$ and $m \in (\pi/H, 2\pi/H)$ on a common color scale at the times when the pulses have reached a common distance, with red being positive and blue being negative. (middle row) Same, but for the approximation to b_m^{leaky} given in equation (4.17). (bottom row) The projections of b_m^{leaky} onto the first-baroclinic and second-baroclinic rigid-lid modes, as given by equation (4.16).

and second baroclinic ($N_2/N_1 = 2.5$ and $m = 2\pi/H$). For an apples-to-apples comparison, these are plotted on the same color scale at a time in their evolution when the pulses have reached a common distance from the origin (i.e., at a time for the second-baroclinic pulses that is twice the time for the first-baroclinic pulses). The abscissa ranges over plus or minus twice that distance. The ordinate ranges over the full depth of the troposphere.

At the center of each pulse, b_m^{leaky} evaluates to

$$b_m^{\text{leaky}}(\pm N_1 t/m, z, t) = \frac{N_2}{N_1}\frac{B_0 H m^2}{2\pi N_1 t}\sin(mz) \qquad \text{for } z \leq H\,. \tag{4.15}$$

Since the buoyancy pulses travel at a speed of $c_{gx} = N_1/m$, their amplitude is proportional to $m/c_{gx}t$. For the same distance traveled (i.e., for the same value of $c_{gx}t$), the amplitude of the wave is proportional to the baroclinicity (i.e., proportional to m). Since the width of the buoyancy pulse is inversely proportional to the amplitude, this means that, when a second-baroclinic pulse has traveled 100 km, it is twice as compact in the horizontal as the second-baroclinic pulse when it reaches 100 km. In summary, the nth-baroclinic pulse spreads out at $1/n^2$ the rate per time, and $1/n$ the rate per distance, as compared to a 1st-baroclinic pulse.

Although the buoyancy pulse at $x = \pm N_1 t/m$ has the same baroclinicity as the initial heating, this is not generally true at other x. This is expected since any initial vertical structure that is zero in the stratosphere is not a normal mode of the leaky-lid atmosphere. The eigenvalue spectrum is continuous for any atmosphere that is unbounded in the z-direction, so any such initial vertical structure projects onto an infinite number of normal modes, all of which have different phase speeds. These different components of the initial buoyancy distribution radiate away from the initial heat source at different speeds, and thus begin decohering immediately, leading to the complicated horizontal and vertical structure of $b_m^{\text{no lid}}$ for $t > 0$, which is visible in the top row of Figure 4.4. Mathematically, this complexity stems from the tz/x argument in equation (4.13).

Given this complexity, how can we make contact with the standard rigid-lid paradigm? Is there some way that we can write b_m^{leaky} in terms of the rigid-lid modes even though the rigid-lid modes are not normal modes of the leaky-lid atmosphere? The answer is yes: we could simply write b_m^{leaky} as a sum of rigid-lid modes. But, this approach is of little conceptual advantage if, say, a first-baroclinic heating generates a buoyancy pulse that projects strongly onto higher-baroclinic modes.

We can quantify these contributions by projecting b_m^{leaky} onto the various baroclinic modes. The projection of b_m^{leaky} onto baroclinic mode m', which we will denote by $a_{m,m'}^{\text{leaky}}$, is

$$\begin{aligned} a_{m,m'}^{\text{leaky}}(x,t) &= \frac{2}{H}\int_0^H dz\, \sin(m'z) b_m^{\text{leaky}}(x,z,t) \\ &= \frac{2B_0 N_1 t x^2}{\pi m m' H} \frac{\sin^2\left(HN_1 t/x\right)}{\frac{N_1}{N_2} + \left(\frac{N_2}{N_1} - \frac{N_1}{N_2}\right)\sin^2\left(HN_1 t/x\right)} \\ &\quad \times \frac{\cos(mH)\cos(m'H)}{\left[\left(N_1 t/m\right)^2 - x^2\right]\left[\left(N_1 t/m'\right)^2 - x^2\right]}\,. \end{aligned} \tag{4.16}$$

For the four cases shown in the top row of Figure 4.4, the projections onto the first and second baroclinic modes are shown in the bottom row of Figure 4.4. These are plotted on common axes with the red curves representing the projection onto the first baroclinic mode and the blue curves representing the projection onto the second baroclinic mode. In the no-lid troposphere, a first-baroclinic heating generates a buoyancy pattern that projects strongly onto the second-baroclinic mode; as seen in the lower-left panel of Figure 4.4, the maximum amplitude of the $m' = 2\pi/H$ projection is nearly as large as the maximum amplitude of the $m' = \pi/H$ projection. For the leaky-lid with a realistic N_2/N_1, however, a first-baroclinic heating generates a buoyancy pattern that projects predominantly onto the first baroclinic mode.

Based on these findings, we conclude that, unlike in a no-lid atmosphere, the projection of the buoyancy onto its original vertical structure is a good approximation in a leaky-lid atmosphere with a realistic stratification jump. This means, for example, that we can approximate b_m^{leaky} by $a_{m,m}^{\text{leaky}}\sin(mz)$:

$$\begin{aligned} b_m^{\text{leaky}}(x,z,t) \approx \frac{B_0}{2\pi} & \frac{\sin^2\left(HN_1t/x\right)}{\frac{N_1}{N_2} + \left(\frac{N_2}{N_1} - \frac{N_1}{N_2}\right)\sin^2\left(HN_1t/x\right)} \\ & \times \frac{x}{mH}\left[-\frac{1}{(N_1t/m+x)^2} + \frac{1}{(N_1t/m-x)^2}\right]\sin(mz) \\ & \qquad \text{for } z \leq H\,. \end{aligned} \tag{4.17}$$

This approximation has the great advantage of having a rigid-lid vertical structure – i.e., the $\sin(mz)$ – while still retaining the horizontal decoherence generated by the leaky lid.

This approximation to b_m^{leaky} is plotted in the middle row of Figure 4.4. For the no-lid atmosphere, the approximation misses much of the structure of the buoyancy, especially for a first-baroclinic heating. For a leaky-lid atmosphere, however, the approximation is quite accurate.

Finally, let us return to Figure 4.1. The right panel shows the response to a first-baroclinic heating that is confined to the troposphere and is turned on at time $t = 0$. Unlike the CRT modes, which must be excited by heating the stratosphere as well, the atmosphere reaches a steady state in response to this steady tropospheric heating. Since any steady tropospheric heating can be constructed out of the b_m^{leaky} Green's functions, this tells us that, for a leaky-lid atmosphere, any steady heating confined to the troposphere will generate a steady response.

4.2.5 Leaky-lid wave decay

The preceding analysis tells us about the evolution of buoyancy caused by a heating confined to $x = 0$ in the troposphere. But, what about a heating that is sinusoidal in x? How does the leaky lid modify the tropospheric residence time for such waves?

In principle, we could use the Green's function b_m^{leaky} to calculate the evolution of a horizontally sinusoidal heating, but, in practice, we were unable to find a way to perform this calculation analytically. Instead, we can make an educated guess based on what we have learned so far and then check that guess against a numerical calculation. In equation (4.11), we introduced a time scale for waves in the no-lid troposphere, and a comparison of equations (4.11) and (4.15) suggests a simple modification for the leaky-lid troposphere. Equations (4.11) and (4.15) are the amplitudes of the tropospheric buoyancy at $x = \pm N_1 t/m$ for the no-lid and leaky-lid cases, respectively. These expressions differ only by an overall factor of N_2/N_1. Since amplitude and width of a buoyancy pulse are inversely related, this means that a one-way-propagating buoyancy pulse widens N_1/N_2 times slower in the presence of a leaky lid. Since the emission of waves from the troposphere is responsible for widening the pulse, this implies that waves exit the troposphere N_1/N_2 times slower in the leaky-lid case compared to the no-lid case and, therefore, reside in the troposphere N_2/N_1 times longer. Therefore, equation (4.12) generalizes to

$$\tau_k = \frac{N_2}{N_1}\frac{m^2 H}{N_1|k|}\,. \tag{4.18}$$

This timescale exhibits the behavior we expect from studying the Green's function. Namely, the residence time is longer for longer waves (smaller $|k|$) and for more rigid lids (larger N_2/N_1).

4.2.6 Numerical validation of the wave timescale

To confirm that the timescale in (4.18) is a good approximation for a freely propagating gravity wave in an atmosphere with two layers of differing N, we performed a series of numerical simulations using Dedalus, a flexible, open-source, Python-based framework for solving partial differential equations (www.dedalus-project.org). Dedalus is a spectral solver, and we decompose the domain using a Chebyshev basis in the z direction and Fourier modes in the horizontal. We solve the linearized Boussinesq system (4.5a)-(4.5d) on a periodic domain of width $L = 3000$ km, with rigid boundaries at the top and bottom of the domain. The tropopause is located at $H = 17$ km, and the rigid top is placed at 170 km, which is sufficiently high to prevent reflected waves from re-entering the troposphere for the duration of the simulation.

To test equation (4.18), we initialize the system with a buoyancy perturbation confined to the troposphere, characterized by a single horizontal wavenumber k and vertical structure corresponding to a single baroclinic mode m. While we are ultimately interested in the amplitude of the buoyancy anomaly, diagnosing the wave energy, which is proportional to the amplitude squared, provides a straightforward (and single-signed) way of bookkeeping in this simple simulation setup. We compare the evolution of the wave energy in the troposphere to the timescale predicted by (4.18), bearing in mind that, because energy is proportional to amplitude squared, the decay timescale for energy is $\tau_k/2$. Each simulation is run for for at least τ_k, over which we expect the energy in the troposphere to undergo two e-foldings. We run a total of 80 simulations, corresponding to all combinations of: $m = \pi/H$ and $2\pi/H$; $N_2/N_1 = 1$, 2, 3, 4, and 5; and $k = 2\pi n/L$ for integer values of n from 3 through 10, which correspond to horizontal wavelengths ranging from 300 km to 1000 km. At each time step, the buoyancy is projected onto the baroclinic mode of the original heating and the tropospheric energy in that mode is calculated. The decay timescale is then estimated as -2 times the inverse of the slope of the linear regression of the logarithm of tropospheric energy versus time. The τ_k calculated from each simulation is plotted against the theoretical τ_k from (4.18) in Figure 4.5, along with a dashed one-to-one line. Figure (4.5) shows very good agreement between the theory and simulation for most parameter values, confirming that the approximate timescale in equation (4.18) correctly characterizes the emission rate of internal gravity waves from an Earth-like troposphere.

4.3 Lifetime of a pulse of buoyancy

We are now prepared to investigate how a heating of finite width propagates through a two-dimensional troposphere. In principle, we can use the Green's function to calculate how

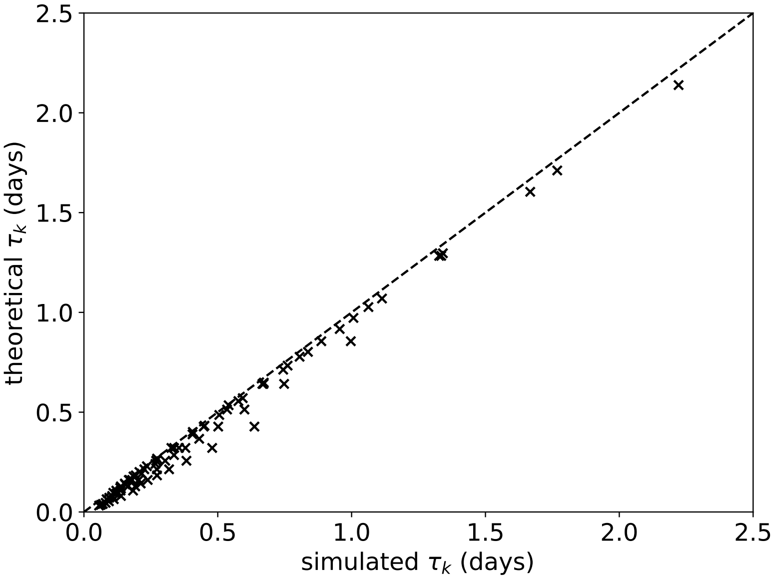

Figure 4.5: Simulated tropospheric decay timescale τ_k versus that predicted from equation (4.18) for 80 simulations, which encompass all combinations of $N_2/N_1 = 1$, 2, 3, 4, and 5, and $k = 2\pi n/3000$ km^{-1} for integer values of n from 3 through 10, for both the first and second vertical mode $(m = \pi/H, 2\pi/H)$.

any buoyancy distribution evolves to a horizontally uniform final state. For simplicity, we focus here on heatings that have a top-hat distribution in the horizontal,

$$Q = b_0 \mathcal{H}(a/2 - |x|)\delta(t)\sin(mz)\,, \tag{4.19}$$

where a is the width of the heating. This generates a buoyancy distribution at $t = 0^+$ that is given by $b_m^{\text{top hat}}(x, z, 0^+) = b_0 \mathcal{H}(a/2 - |x|)\sin(mz)$.

To find out how this buoyancy evolves in time, we can convolve this initial buoyancy distribution with the Green's function, i.e., with the b_m^{leaky} from equation (4.13). Before we do that, however, let us see if we can learn something about its behavior by considering the residence timescales for its Fourier components. The Fourier transform of $b_m^{\text{top hat}}(x, z, 0^+)$ is

$$\begin{aligned}\tilde{b}_m^{\text{top hat}}(k, z, 0^+) &= \frac{1}{\sqrt{2\pi}}\int_{-\infty}^{\infty} dx\, e^{ikx} b_m^{\text{top hat}}(x, z, 0^+) \\ &= \frac{2b_0}{\sqrt{2\pi}}\frac{\sin(ak/2)}{k}\sin(mz)\mathcal{H}(H - z)\,. \end{aligned} \tag{4.20}$$

The Fourier transform of the same amount of horizontally integrated buoyancy concentrated at $x = 0$, i.e., $b_m^{\text{leaky}}(x, z, 0^+)$ from equation (4.13) with $B_0 = ab_0$, is

$$\tilde{b}_m^{\text{leaky}}(k, z, 0^+) = \frac{1}{\sqrt{2\pi}}\int_{-\infty}^{\infty} dx\, e^{ikx} b_m^{\text{leaky}}(x, z, 0^n+) = \frac{ab_0}{\sqrt{2\pi}}\sin(mz)\mathcal{H}(H - z)\,. \tag{4.21}$$

Taylor expanding (4.20) in k, we find

$$\tilde{b}_m^{\text{top hat}}(k, z, 0^+) = \tilde{b}_m^{\text{leaky}}(k, z, 0^+)\left(1 - \frac{a^2k^2}{24} + \dots\right)\,.$$

For $|k|$ satisfying $a^2k^2/24 \ll 1$, i.e., for $|k| \lesssim 1/a \ll 2\sqrt{6}/a$, the Fourier transform of $\tilde{b}_m^{\text{top hat}}$ is practically indistinguishable from the Fourier transform of $\tilde{b}_m^{\text{leaky}}$.

Since waves emanate from the troposphere on a timescale proportional to their wavenumber, there will be a time τ^{melt} when wavenumbers $|k| > 1/a$ will have mostly left the troposphere. After that time, $\tilde{b}^{\text{top hat}}(k, z, t)$ is practically indistinguishable from $\tilde{b}^{\text{leaky}}(k, z, t)$. We refer to τ^{melt} as the timescale for "melting" because this is the time by which the initial horizontal shape of the buoyancy pulse has melted away. Based on the preceding argument, we can define τ^{melt} as the time at which wavenumber $1/a$ has experienced an e-folding of decay, i.e., we define τ^{melt} as the τ_k from equation (4.18) with $k = 1/a$,

$$\tau^{\text{melt}} = \frac{N_2}{N_1}\frac{m^2Ha}{N_1}\,. \tag{4.22}$$

By equation (4.15), the amplitude of b_m^{leaky} at $x = \pm N_1\tau^{\text{melt}}/m$ and $t = \tau^{\text{melt}}$ is $b_0/2\pi$.

We can now summarize the evolution of the initial top-hat pulse. At time $t = am/2N_1$, the top-hat buoyancy pulse of magnitude b_0 and width a splits into two pulses, each with magnitude $b_0/2$ and width a, one of which is right-moving and the other left-moving. At time $t = \tau^{\text{melt}}$, each of the unidirectional pulses has melted down to a peak amplitude of $b_0/2\pi$ and is indistinguishable from an initial delta-function buoyancy pulse. For $t > \tau^{\text{melt}}$, the buoyancy evolves as b_m^{leaky} with the amplitude at $x = \pm N_1 t/m$ equal to $b_0 \tau^{\text{melt}}/2\pi t$.

Figure 4.6 compares the evolution of the initial top hat (solid red), as calculated numerically by convolution with the Green's function, against the evolution of an initial delta-function source (dashed green) with the same horizontally integrated buoyancy for the case of $N_2/N_1 = 2.5$. Also shown is the evolution of the top-hat pulse for a rigid lid (dashed black), i.e., for $N_2/N_1 = \infty$. The abscissa is a normalized distance in which unity is the distance traveled in an amount of time equal to τ^{melt}. As expected, the top-hat pulse has become indistinguishable from an initial delta-function pulse by the time $t = \tau^{\text{melt}}$.

We can perform a further check of τ^{melt} by numerically convolving an initial top-hat distribution with the Green's function b_m^{leaky} from (4.13) and diagnosing the time when the amplitude at $|x| = N_1 t/m$ equals $b_0/2\pi$. The top panel of Figure 4.7 shows the amplitude of the right-moving half of a first-baroclinic top hat at $x = N_1 t/m$ for $N_2/N_1 = 1$, 2.5, 5, and 10. The x-axis is normalized by τ^{melt} so that the curves are independent of the width of the initial top hat. The first-baroclinic Green's function amplitude, i.e., $b_m^{\text{leaky}}(N_1 t/m, H/2, t)$, is given by the dashed black line. As the right-mover and left-mover separate at small t/τ^{melt}, there are undulations in the buoyancy distribution that cause the buoyancy to briefly exceed its initial value of $b_0/2$. By $t/\tau^{\text{melt}} = 1$, though, all the curves have converged to the Green's function amplitude.

The lower panel of Figure 4.7 shows the approximate τ^{melt} from equation (4.22) plotted against the τ^{melt} diagnosed from the time it takes for the numerically-integrated, right-moving, first-baroclinic, top-hat pulses to decrease their peak amplitude to $b_0/2\pi$. The top hats are integrated for all combinations of $a = 100$, 500, 2000, 4000 and 8000 km, and $N_2/N_1 = 1$, 2.5, 5, and 10. These points all fall very close to the black-dashed one-to-one line.

A few things are notable about the lifetimes of buoyancy anomalies implied by τ^{melt}. First, the timescale is proportional to N_2/N_1, so that as $N_2/N_1 \to \infty$, $\tau_{\text{melt}} \to \infty$ too, which is what we expect for the rigid-lid limit. It is also proportional to the width of the pulse, so wider buoyancy anomalies retain their horizontal shape longer. Finally, it is quadratic in m, the baroclinic mode of the initial anomaly. This has potentially significant implications for the wave spectrum of equatorial Kelvin waves: the second-baroclinic pulses retain their original shapes four times as long as first-baroclinic pulses.

In general, these decay timescales are quite fast. For a first-baroclinic buoyancy pulse ($m = \pi/H$) in an Earth-like atmosphere ($N_2/N_1 = 2.5$, $N_1 = 0.01\ \text{s}^{-1}$, $H = 17$ km) with a width of 100 km, the original horizontal shape of the left-moving and right-moving buoyancy pulses melts away in only four hours, which is how long it takes each pulse to travel about 800 km from their origin. By that time, each of the pulses has been reduced in amplitude by a factor of $1/\pi$. After this time, the amplitudes decrease as $1/t$, so that, by eight hours, the peak amplitudes have been reduced by another factor of two.

Although the "melting" time depends on the characteristic width of the initial pulse of heating, the time to homogenize that heating over a periodic domain is independent of the

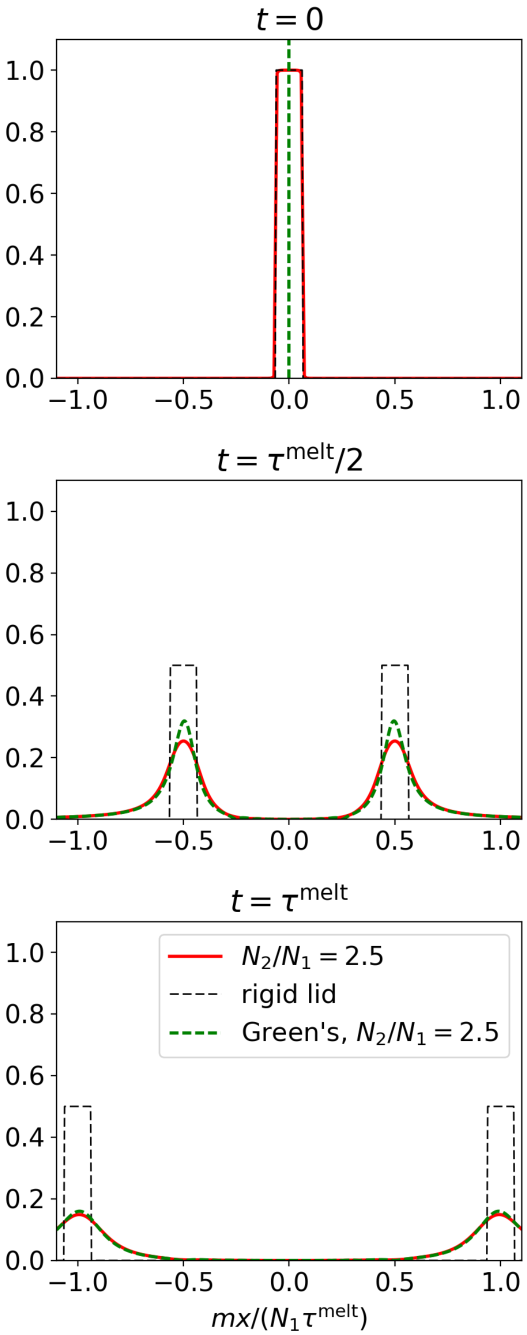

Figure 4.6: The red solid line shows the projection of buoyancy from a first-baroclinic top-hat heating onto the first baroclinic mode at $t = 0$, $\tau^{\mathrm{melt}}/2$, and τ^{melt} for $N_2/N_1 = 2.5$, which is found by numerically convolving a top hat with the baroclinic Green's function (4.13). The green dashed line shows the baroclinic Green's function (4.13) with the same profile of horizontally integrated buoyancy. This is an excellent approximation to the top hat for times greater than the τ^{melt} of equation (4.22). The abscissa is the distance normalized by the baroclinic wavespeed (N_1/m) times τ^{melt}.

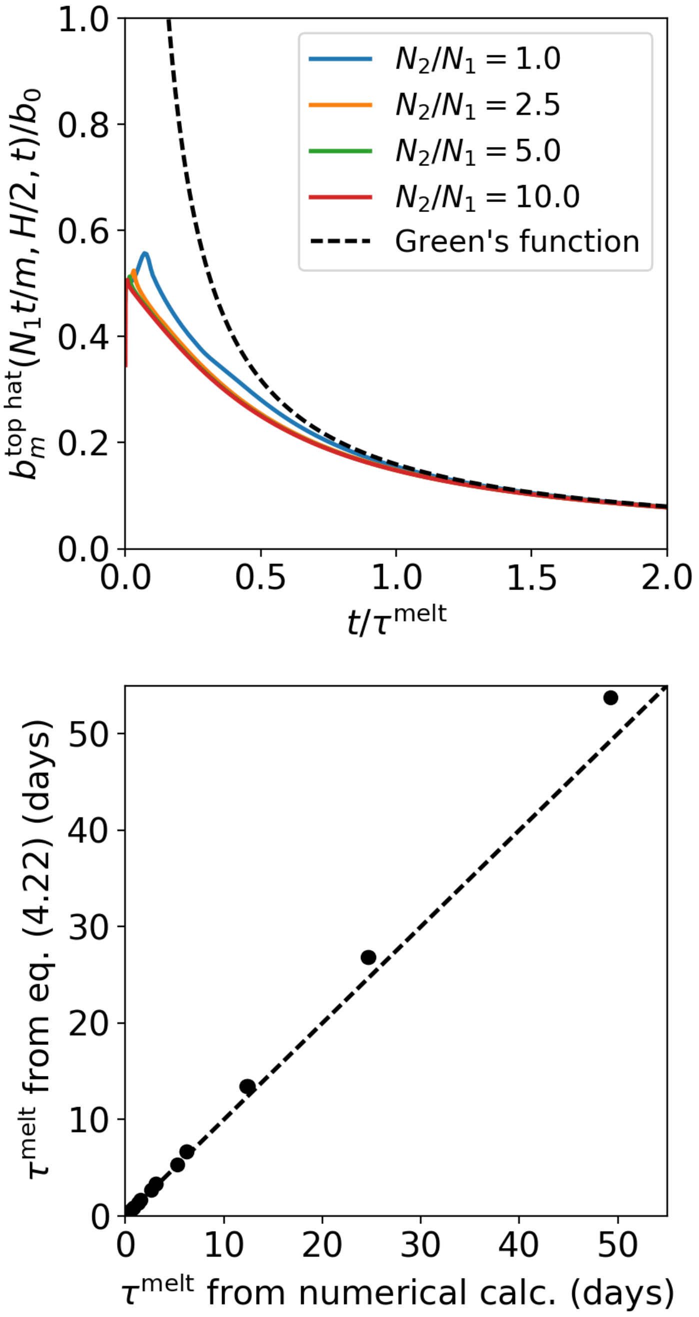

Figure 4.7: (top) Fraction of the initial peak buoyancy at $x = N_1 t/m$ as function of t/τ^{melt} for the right-moving half of a first-baroclinic top hat pulse of buoyancy, for $N_2/N_1 = 1$, 2.5, 5, and 10. (bottom) Estimated τ^{melt} from equation (4.22) plotted against the actual τ^{melt} for first baroclinic top hats of with $a = 100$, 500, 2000, 4000, and 8000 km, for $N_2/N_1 = 1$, 2.5, 5, and 10. The actual τ^{melt} is found by numerically integrating the Green's function (4.13) and finding the time when the buoyancy at $x = N_1 t/m$ drops below $b_0/2\pi$.

initial pulse width. To homogenize over a periodic domain of length L, we must wait a time equal to the τ_k from equation (4.18) with $k = 2\pi/L$. For a first-baroclinic pulse on a periodic domain of length L equal to the Earth's equatorial circumference of 40,000 km, this homogenization takes about 10 days. This is a remarkably short period of time: an isolated pulse of tropospheric heating generates left-moving and right-moving pulses that reduce to horizontal wavenumbers one and two by day 2.5, to horizontal wavenumber 1 by day 5, and to an approximately uniform heating around the entire 40,000-km-long domain by day 10.

4.4 Conclusions

Assuming that the tropical tropopause is a rigid lid greatly simplifies tropical wave dynamics, but is not physically justifiable and leads to a choice between the spurious persistence of buoyancy anomalies in the troposphere or using unrealistically strong damping. In this study, we show that replacing the rigid lid with an overlying layer of stratified fluid resolves this difficulty. We have derived equation (4.13), which is the Green's function for a two-dimensional, non-rotating, Boussinesq fluid comprised of two layers of constant but differing buoyancy frequency, which are meant to represent the troposphere and stratosphere. This solution is valid for any ratio of the buoyancy frequencies in the two layers. It includes the rigid-lid solution (an infinitely stratified upper layer) and the no-lid solution (a stratosphere with the same stratification as the troposphere) as limiting cases. We have used this Green's function to show that the dispersive nature of upward internal gravity wave propagation damps away buoyancy anomalies in Earth's troposphere on timescales of hours to days, which are comparable to the linear damping timescales used in simple models of the tropical atmosphere. This naturally leads to the speculation that simple models of the atmosphere with rigid lids at the tropopause may require strong Rayleigh friction or Newtonian cooling in part because they lack this process.

Of course, the dispersion of vertically-propagating internal gravity waves is not equivalent to a linear damping, e.g., Rayleigh friction or Newtonian cooling. While both processes smooth out buoyancy anomalies, linear damping also removes the horizontal mean buoyancy anomaly. On the other hand, vertically-propagating gravity waves leave behind a steady, horizontally-uniform buoyancy anomaly, and in a steady state this must be removed by a domain-mean diabatic cooling.

Chapter 5

Conclusions

Moist convection in the earth's atmosphere is a complex, nonlinear, turbulent process involving multiple phase changes. The spatial and temporal scales span multiple orders of magnitude, from ice crystals a few microns across to hurricanes hundreds of kilometers wide. Furthermore, moist convection plays a key role in earth's energy budget, transporting energy and moisture from the surface to high in the atmosphere. The fast and localized nature of convection makes it difficult to model at the global scale, but its influence on climate and large-scale atmospheric circulation are undeniably large, even if many aspects are poorly understood.

In this dissertation, we illuminated some key aspects of how moist convection interacts with large-scale circulations. In Chapter 2, we showed how the interaction between a patch of atmosphere and the environment can be modeled as a monochromatic gravity wave, and derived a simple method, known as the weak-pressure-gradient approximation (WPG), to use in cloud-resolving and single-column models. In Chapter 3, we tested WPG and other ways of parameterizing the interaction between a column of atmosphere and the large-scale circulation, and found that some of these methods pass a simple test of self-consistency. Finally, in Chapter 4, we looked beyond these simple models and derived new analytic solutions for pulses of heating in a stratified atmosphere with realistic vertical structure. These more realistic solutions solve some of the glaring problems present in solutions based on the assumption of rigid lid at the tropopause, and we discover that buoyancy anomalies in the tropical atmosphere decay on timescales of hours to days, purely due to upward radiation of wave energy.

Bibliography

Battisti, D. S., Sarachik, E. S., & Hirst, A. C. 1999, Journal of Climate, 12, 2956

Bergman, J. W., & Sardeshmukh, P. D. 2004, Journal of Climate, 17, 1004

Blossey, P. N., Bretherton, C. S., & Wyant, M. C. 2009, Journal of Advances in Modeling Earth Systems, 2, 8

Bony, S., Bellon, G., Klocke, D., et al. 2013, Nature Geoscience, 6, 447

Bretherton, C. S., Blossey, P. N., & Khairoutdinov, M. 2005, Journal of the Atmospheric Sciences, 62, 4273

Bretherton, C. S., & Smolarkiewicz, P. K. 1989, Journal of the Atmospheric Sciences, 46

Chan, I. H., & Shepherd, T. G. 2014, Journal of the Atmospheric Sciences, 71, 985

Chang, C.-P. 1977, Journal of the Atmospheric Sciences, 34, 901

Charney, J. 1963, Journal of the Atmospheric Sciences, 20, 607

Chiang, J., & Sobel, A. 2002, Journal of Climate, 15, 2616

Chumakova, L. G., Rosales, R. R., & Tabak, E. G. 2013, Journal of the Atmospheric Sciences, 70, 3119

Cohen, B. G., & Craig, G. C. 2004, Quarterly Journal of the Royal Meteorological Society, 130, 933

Daleu, C. L., Woolnough, S. J., & Plant, R. S. 2012, Journal of the Atmospheric Sciences, 69, 3683

Dias, P. S., Schubert, W., & DeMaria, M. 1983, Journal of the Atmospheric Sciences, 40, 2689

Edman, J. P., & Romps, D. M. 2014, Journal of the Atmospheric Sciences, 71, 2415

—. 2015, Journal of Advances in Modeling Earth Systems, 7, 320

—. 2017, Journal of the Atmospheric Sciences, 74

Emanuel, K., & Sobel, A. 2013, Journal of Advances in Modeling Earth Systems, 5, 447

Emanuel, K., Wing, A. A., & Vincent, E. M. 2014, Journal of Advances in Modeling Earth Systems

Fridlind, A., Ackerman, A., Petch, J., & Field, P. 2010, ARM/GCSS/SPARC/TWP-ICE CRM Intercomparison Study, Tech. Rep. NASA-TM-2010-215858, National Aeronautics and Space Administration

Ghan, S. J., Randall, D. A., Xu, K., & Cripe, D. G. 1999, in Ninth ARM Science Team Meeting Proceedings, 1

Gill, A. E. 1980, Quarterly Journal of the Royal Meteorological Society, 106, 447

—. 1982, Atmosphere-Ocean Dynamics, International Geophysics (Elsevier Science)
Hack, J. J., & Pedretti, J. A. 2000, Journal of Climate, 13, 352
Haertel, P., & Johnson, R. 1998, Quarterly Journal of the Royal . . . , 124, 615
Haertel, P. T., & Kiladis, G. N. 2004, Journal of the Atmospheric Sciences, 61, 2707
Held, I. M., Hemler, R. S., & Ramaswamy, V. 1993, Journal of the Atmospheric Sciences, 50, 3909
Hendon, H. H., & Wheeler, M. C. 2008, Journal of the Atmospheric Sciences, 65, 2936
Herman, M. J., & Raymond, D. J. 2014, Journal of Advances in Modeling Earth Systems, n/a
Holton, J. 1973, Monthly Weather Review, 101, 201
Jeevanjee, N., & Romps, D. M. 2013, Geophysical Research Letters, 40, 1
Kuang, Z. 2008, Journal of the Atmospheric Sciences, 65, 576
—. 2011, Journal of the Atmospheric Sciences, 68, 61
—. 2012, Journal of the Atmospheric Sciences, 69, 2759
Lin, J.-L., Mapes, B. E., & Han, W. 2008, Journal of Climate, 21, 165
Lin, Y. L., & Smith, R. B. 1986, Journal of the Atmospheric Sciences, 43, 40
Lindzen, R. S. 2003, Journal of the Atmospheric Sciences, 60, 3009
Mapes, B. 1993, Journal of the Atmospheric Sciences, 50
—. 1997, Equilibrium vs. activation control of large-scale variations of tropical deep convection, 321
—. 1998, Journal of the Meteorological Society of Japan, 76, 29
—. 2004, Journal of the atmospheric sciences, 2308
Mapes, B., Ciesielski, P., & Johnson, R. 2003, Journal of the Atmospheric Sciences, 60, 2697
Mapes, B. E. 2000, Journal of the Atmospheric Sciences, 57, 1515
Mapes, B. E., & Houze, R. A. 1995, Journal of the Atmospheric Sciences, 52, 1807
Matsuno, T. 1966, Journal of the Meteorological Society of Japan, 44, 25
Muller, C. J., & Held, I. M. 2012, Journal of the Atmospheric Sciences, 69, 2551
Neelin, J., & Held, I. 1987, Monthly weather review
Nilsson, J., & Emanuel, K. 1999, Quarterly Journal of the Royal Meteorological Society, 2239
Pandya, R., Durran, D. R., & Bretherton, C. 1993, Journal of the Atmospheric Sciences
Randall, D., Xu, K., Somerville, R., & Iacobellis, S. 1996, Journal of Climate, 9
Raymond, D. 2007, Quarterly Journal of the Royal Meteorological Society, 1085, 1073
Raymond, D. J., & Zeng, X. 2000, Quarterly Journal of the Royal Meteorological Society, 3117
—. 2005, Quarterly Journal of the Royal Meteorological Society, 131, 1301
Roads, J., Chen, S., Kanamitsu, M., & Juang, H. 1998, Journal of Geophysical Research, 103
Romps, D. M. 2008, Journal of the Atmospheric Sciences, 65, 3779
—. 2012a, Journal of the Atmospheric Sciences, 69, 2846
—. 2012b, Journal of the Atmospheric Sciences, 69, 2835
—. 2013, Journal of the Atmospheric Sciences, in review
—. 2014, Journal of the Atmospheric Sciences, 71, 553
Sessions, S. L., Sugaya, S., Raymond, D. J., & Sobel, A. H. 2010, Journal of Geophysical

Research, 115, D12110

Sobel, A., Bellon, G., & Bacmeister, J. 2007, Geophysical Research Letters, 34, L22804

Sobel, A., & Bretherton, C. 2000, Journal of climate, 13, 4378

Sobel, A., Nilsson, J., & Polvani, L. 2001, Journal of the atmospheric sciences, 3650

Stephens, G. L., van den Heever, S., & Pakula, L. 2008, Journal of the Atmospheric Sciences, 65, 3899

Sugiyama, M. 2009, Journal of the Atmospheric Sciences, 66, 1507

Tulich, S. N., Randall, D. a., & Mapes, B. E. 2007, Journal of the Atmospheric Sciences, 64, 1210

Wang, S., & Sobel, A. 2012, Journal of Geophysical Research, 10027, 1

Wang, S., Sobel, A., & Kuang, Z. 2013, Journal of Geophysical Research: Atmospheres, 118, 1

Wang, S., & Sobel, a. H. 2011, Journal of Geophysical Research, 116, 1

Wheeler, M., & Kiladis, G. N. 1999, Journal of the Atmospheric Sciences, 56, 374

Wing, A. A., & Emanuel, K. A. 2014, Journal of Advances in Modeling Earth Systems, 6, 59

Wu, Z., Sarachik, E., & Battisti, D. 2000, Journal of the Atmospheric Sciences, 2169

Yano, J., & Emanuel, K. 1991, Journal of the Atmospheric Sciences, 48, 377

Appendix A

A.1 Horizontal density gradients are small in the tropical atmosphere

Both WPG and WTG take advantage of the observation, that in the tropics, horizontal density gradients are small. We can see that this is due to the lack of influence of the earth's rotation in the tropics from a simple scaling analysis of the governing equations, originally carried out in Charney (1963). The governing equations for momentum, potential temperature, and mass for a rotating fluid in hydrostatic balance are:

$$\begin{aligned} \partial_t \mathbf{u} + \mathbf{u} \cdot \nabla \mathbf{u} + w \partial_z \mathbf{u} &= -\frac{\nabla p}{\rho} + f \hat{\mathbf{k}} \times \mathbf{u} & \text{(A.1)} \\ 0 &= \frac{\partial_z p}{\rho} + g & \text{(A.2)} \\ \frac{\partial_t \theta}{\bar{\theta}} + \frac{\mathbf{u}}{\bar{\theta}} \cdot \nabla \theta + \frac{w N^2}{g} &= 0 & \text{(A.3)} \\ \partial_t \rho + \nabla \cdot (\rho \mathbf{u}) + \partial_z \rho w &= 0 & \text{(A.4)} \end{aligned}$$

where $\mathbf{u}$ is the horizontal wind, w is the vertical velocity, ρ is the density, p is the pressure, θ is the potential temperature, g is the gravitational acceleration, f is the Coriolis parameter, and $N \equiv \sqrt{\frac{g \partial_z \theta}{\theta}}$ is the Brunt-Väisälä frequency. The ∇ refers to horizontal derivatives only.

Let us define the pressure anomaly as $p' \equiv p - \bar{p}(z)$, and similarly the density anomaly $\rho' \equiv \rho - \bar{\rho}(z)$. From equation (A.2), we define a scale height $H \sim p/\rho g$, which we also assume to be the characteristic vertical scale of the motion. Then, again invoking the hydrostatic equation, we see that

$$\frac{\rho'}{\rho} \sim \frac{p'}{p}$$

.

Designating U for a horizontal velocity scale, W for a vertical velocity scale, L for a length scale, and the timescale to be the advective timescale, L/U, the terms in equation (A.1) scale like

$$\frac{U^2}{L} \qquad \frac{U^2}{L} \qquad \frac{WU}{H} \qquad \frac{p'}{\rho L} \qquad fU \tag{A.5}$$

Furthermore, the continuity equation requires that $W \lesssim \frac{UH}{L}$, provided density anomalies $(\frac{\rho'}{\rho})$ are order 1 or less, so this scaling implies

$$\frac{\rho'}{\rho} \sim \frac{p'}{p} \sim \frac{U^2}{gH}\ ,\ \frac{fUL}{gH} \tag{A.6}$$

Defining the Rossby number (**Ro**) as U/fL and a Froude number (**Fr**) as U^2/gH (this is different from the Froude number we would normally consider in a stratified fluid, as $\sqrt{gH}$ is not the relevant gravity wave speed), the pressure anomaly scales as either **Fr**/**Ro** or **Fr**. Typical scales are $L \approx 100$ km, $H \approx 8$ km, and $U \approx 10$ m s^{-1}, so $\mathbf{Fr} \sim 10^{-3}$. In the midlatitudes, the Rossby number can be of comparable magnitude or smaller ($f \approx 10^{-4}$ s^{-1} at 45°N), which indicates that density anomalies can be quite large there. But, f goes to zero at the equator, so the Rossby number U/fL is very large throughout the tropics. Thus, because the influence of earth's rotation is negligible, density anomalies in the tropics scale with **Fr**, and are very small:

$$\frac{\rho'}{\rho} \sim \frac{p'}{p} \sim \frac{U^2}{gH} \sim \mathcal{O}(10^{-3}) \tag{A.7}$$

Appendix B

B.1 Inviscid shallow-water solution with a top-hat oscillating source

A top-hat mass source that oscillates with angular frequency ω in a column from x_1 to x_2 may be written as

$$Q(x,t;x_1,x_2) \;=\; Q_0\cos(\omega t)\mathcal{H}(x_2-x)\mathcal{H}(x-x_1)\,.$$

The fundamental solution to the inviscid shallow-water equations from equation (2.4) then becomes

$$\begin{aligned} h(x,t;x_1,x_2) = \frac{Q_0}{2}\int\limits_{-\infty}^{t} dt'\cos(\omega t')\Bigg\{&\mathcal{H}\Big[x_2-\Big(x+c\{t-t'\}\Big)\Big]\mathcal{H}\Big[\Big(x+c\{t-t'\}\Big)-x_1\Big] \\ &+\mathcal{H}\Big[x_2-\Big(x-c\{t-t'\}\Big)\Big]\mathcal{H}\Big[\Big(x-c\{t-t'\}\Big)-x_1\Big]\Bigg\}\,. \end{aligned} \tag{B.1}$$

We can rewrite the integrand using the identity $\mathcal{H}(ct'-a)\mathcal{H}(b-ct')=\mathcal{H}(ct'-a)-\mathcal{H}(ct'-b)$, which holds provided that $a<b$. In this case, a is always less than b since $x_2>x_1$. Rewriting (B.1) with this identity, we obtain

$$\begin{aligned} h(x,t;x_1,x_2) = \frac{Q_0}{2}\int\limits_{-\infty}^{t} dt'\cos(\omega t')\Bigg\{&\mathcal{H}\Big[ct'-(-x_2+x+ct)\Big]-\mathcal{H}\Big[ct'-(-x_1+x+ct)\Big] \\ &+\mathcal{H}\Big[ct'-(x_1-x+ct)\Big]-\mathcal{H}\Big[ct'-(x_2-x+ct)\Big]\Bigg\}\,. \end{aligned} \tag{B.2}$$

This can be broken up into four integrals, with different lower bounds imposed by the step functions:

$$\begin{aligned}
&h(x,t;x_1,x_2) = \\
&\frac{Q_0}{2}\Bigg\{ \int\limits_{t+\frac{x-x_2}{c}}^{t} dt'\cos(\omega t')\mathcal{H}\Big[ct'-(ct+x-x_2)\Big] - \int\limits_{t+\frac{x-x_1}{c}}^{t} dt'\cos(\omega t')\mathcal{H}\Big[ct'-(ct+x-x_1)\Big] \\
&\quad + \int\limits_{t+\frac{x_1-x}{c}}^{t} dt'\cos(\omega t')\mathcal{H}\Big[ct'-(ct+x_1-x)\Big] - \int\limits_{t+\frac{x_2-x}{c}}^{t} dt'\cos(\omega t')\mathcal{H}\Big[ct'-(ct+x_2-x)\Big]\Bigg\}.
\end{aligned} \tag{B.3}$$

Evaluating the integrals leads to the following solution for $h(x,t)$,

$$\begin{aligned}
h(x,t;x_1,x_2) = \frac{Q_0}{2\omega}\Bigg\{ & \mathcal{H}(x_2-x)\Big[\sin(\omega t) - \sin\Big(\omega t + \omega\Big\{x-x_2\Big\}/c\Big)\Big] \\
& -\mathcal{H}(x-x_2)\Big[\sin(\omega t) - \sin\Big(\omega t + \omega\Big\{x_2-x\Big\}/c\Big)\Big] \\
& -\mathcal{H}(x_1-x)\Big[\sin(\omega t) - \sin\Big(\omega t + \omega\Big\{x-x_1\Big\}/c\Big)\Big] \\
& +\mathcal{H}(x-x_1)\Big[\sin(\omega t) - \sin\Big(\omega t + \omega\Big\{x_1-x\Big\}/c\Big)\Big]\Bigg\},
\end{aligned} \tag{B.4}$$

which can be written as

$$\begin{aligned}
h(x,t;x_1,x_2) = \frac{Q_0}{2\omega}\Bigg\{ & \mathrm{sign}(x_2-x)\Big[\sin(\omega t) - \sin\Big(\omega t - \omega\Big|x_2-x\Big|/c\Big)\Big] \\
& + \mathrm{sign}(x-x_1)\Big[\sin(\omega t) - \sin\Big(\omega t - \omega\Big|x-x_1\Big|/c\Big)\Big]\Bigg\}.
\end{aligned} \tag{B.5}$$

For an oscillating source of the form in equation (2.24), the solution becomes

$$h(x,t) \ = \ \left(1+\frac{L_1}{L_2}\right)h(x,t;-L_1,L_1) - \frac{L_1}{L_2}h(x,t;-L_1-L_2,L_1+L_2)\,. \tag{B.6}$$

The average of this function over the column is

$$\overline{h}(t) \ \equiv \ \frac{1}{2L_1}\int_{-L_1}^{L_1} dx'\, h(x',t) \tag{B.7}$$

$$= \ \frac{Q_0}{\omega}\sin(\omega t) + \frac{Q_0 c}{\omega^2 2L_1}\left(1+\frac{L_1}{L_2}\right)\left\{\cos(\omega t) - \cos\left(\omega t - \omega\frac{2L_1}{c}\right)\right\} \tag{B.8}$$

$$-\frac{Q_0 c}{\omega^2 2L_1}\frac{L_1}{L_2}\left\{\cos\left(\omega t - \omega\frac{L_2}{c}\right) - \cos\left(\omega t - \omega\frac{2L_1+L_2}{c}\right)\right\}\,. \tag{B.9}$$

Written as $\overline{h}(t) = h_0 \cos(\omega t + \phi)$, the amplitude h_0 of this oscillation is given by equation (2.25).

Appendix C

C.1 Deriving the Green's function for a leaky-lid atmosphere

The path to our solution for an atmosphere with different N in the troposphere and stratosphere adheres closely to the derivations published by Lin & Smith (1986) and Pandya et al. (1993) for an atmosphere with constant N.

We begin by rewriting the two-dimensional, linearized Boussinesq equations (4.5) as wave equations for w in each layer:

$$\partial_t^2 \partial_z^2 w_1(x,z,t) + N_1^2 \partial_x^2 w_1(x,z,t) = \partial_x^2 Q\,, \quad 0 \leq z \leq H \tag{C.1a}$$

$$\partial_t^2 \partial_z^2 w_2(x,z,t) + N_2^2 \partial_x^2 w_2(x,z,t) = 0\,, \quad H < z. \tag{C.1b}$$

Then, we consider a buoyancy source of the form $Q = B_0 \delta(t)\delta(x)\delta(z - z_0)$. Taking the Laplace transform in time ($t \to s$) and the Fourier transform in x ($x \to k$) of equation (C.1), we find

$$\partial_z^2 \hat{w}_1(x,z,t) + \lambda^2 \hat{w}_1(x,z,t) = \frac{\lambda^2}{\sqrt{2\pi} N_1^2} B_0 \delta(z - z_0)\,, \quad z \leq H \tag{C.2a}$$

$$\partial_z^2 \hat{w}_2(x,z,t) + \lambda_2^2 \hat{w}_2(x,z,t) = 0\,, \quad H < z, \tag{C.2b}$$

where $\lambda \equiv iN_1|k|/s$, and $\lambda_2 \equiv iN_2|k|/s$. The presence of $\delta(z - z_0)$ in the source term Q imposes a jump condition on w_1 at $z = z_0$, which we can find by integrating equation (C.2a) twice in z:

$$[\hat{w}_1]_-^+ = 0 \tag{C.3}$$

$$[\partial_z \hat{w}_1]_-^+ = \frac{\lambda^2}{\sqrt{2\pi} N_1^2} B_0\,, \tag{C.4}$$

where $[\ ]_-^+$ represents the difference across $z = z_0$.

We seek a solution subject to conditions at the surface ($z = 0$) and at the tropopause ($z = H$), as well as a radiation condition as $z \to \infty$. At the surface, the rigid lower boundary requires $\hat{w}_1 = 0$. At the tropopause ($z = H$), enforcing continuity of pressure and vertical velocity requires $\hat{w}_1 = \hat{w}_2$ and $\partial_z \hat{w}_1 = \partial_z \hat{w}_2$. Above $z = H$, we require that $\hat{w}_2 \to 0$ as $z \to \infty$.

If the buoyancy frequency is constant (i.e., if $N = N_1$ everywhere), then the solution to the transformed equations (C.2) is

$$\hat{w}_1 = \hat{w}_2 \equiv \hat{w}_0^{\pm} = \begin{cases} -\frac{\lambda B_0}{\sqrt{2\pi} N_1^2} e^{i\lambda z_0} \sin(\lambda z)\,, & 0 \le z \le z_0 \\ -\frac{\lambda B_0}{\sqrt{2\pi} N_1^2} \sin(\lambda z_0) e^{i\lambda z}\,, & z_0 < z \end{cases} . \tag{C.5}$$

This solution applies throughout the whole atmosphere, so have we defined a new variable $\hat{w}_0^{\pm}$, where $+$ refers to the solution for $z > z_0$ and $-$ refers to the solution for $z < z_0$.

Multiplying by $1/s$ in Laplace-transformed space is integration in time in real space, so we solve for the buoyancy by multiplying the $\hat{w}$ solutions by $-N_1^2/s$ and inverting the Fourier and Laplace transforms. We find that the buoyancy due to a source term $Q = B_0 \delta(t) \delta(x) \delta(z - z_0)$ in an atmosphere with constant N is

$$b_{\text{point}}^{\text{no lid}}(x, z, t) = \frac{B_0 N_1 t}{\pi x^2} \sin\left(\frac{N_1 t z}{x}\right) \sin\left(\frac{N_1 t z_0}{x}\right) . \tag{C.6}$$

To find the solution for the source term with baroclinic structure in the troposphere given by equation (4.8), we integrate equation (C.6) against $\sin(m z_0)$ through the troposphere:

$$\begin{aligned} b_m^{\text{no lid}}(x, z, t) = & \textstyle\int_0^H dz_0 \sin(m z_0) b_{\text{point}}^{\text{no lid}}(x, z, t) \\ = & \tfrac{B_0}{2\pi} \cos(mH) \sin\left(H N_1 t/x\right) \sin\left(N_1 t z/x\right) \\ & \times \left[\tfrac{1}{N_1 t/m + x} + \tfrac{1}{N_1 t/m - x}\right] , \end{aligned} \tag{C.7}$$

where m is one of the baroclinic modes. This is the Green's function for the constant-N atmosphere, which is equation (4.10) in the main text.

Now, suppose $N_2 = (1 + \gamma) N_1$, where $\gamma \ge -1$. While we cannot integrate the modified version of equation (C.5) directly for the case $N_1 \ne N_2$, we can expand the modified version of equation (C.5) in γ around $\gamma = 0$ and integrate each term in the series. By integrating enough terms and determining what the series converges to, we find a solution valid for all $\gamma \ge -1$, i.e., for all $N_2 \ge 0$.

After rewriting $\hat{w}_1$ in terms of γ, we find

$$\hat{w}_1 = \begin{cases} -\frac{\lambda B_0}{\sqrt{2\pi} N_1^2} e^{i\lambda z_0} \sin(\lambda z) \left[\frac{1 + \frac{\gamma}{2}(1 - e^{2i\lambda(H - z_0)})}{1 + \frac{\gamma}{2}(1 - e^{2i\lambda H})}\right], & 0 \le z \le z_0 \\ -\frac{\lambda B_0}{\sqrt{2\pi} N_1^2} \left\{ e^{i\lambda z_0} \sin(\lambda z) \left[\frac{1 + \frac{\gamma}{2}(1 - e^{2i\lambda(H - z_0)})}{1 + \frac{\gamma}{2}(1 - e^{2i\lambda H})}\right] - \sin(\lambda(z - z_0)) \right\}, & z_0 < z \le H \end{cases} \tag{C.8}$$

and

$$\hat{w}_2 = -\frac{\lambda B_0}{\sqrt{2\pi} N_1^2} \left[e^{i\lambda z} \sin(\lambda z_0)\right] \left[\frac{e^{i\lambda\gamma(z - H)}}{1 + \frac{\gamma}{2}(1 - e^{2i\lambda H})}\right], \ H < z \tag{C.9}$$

We focus our attention on the solution in the troposphere, equation (C.8), which can be expanded about $\gamma = 0$ by noting that the denominator becomes

$$\left[1 + \frac{\gamma}{2}\left(1 - e^{2i\lambda H}\right)\right]^{-1} \approx 1 - \frac{\gamma}{2}\left(1 - e^{2i\lambda H}\right) + \frac{\gamma^2}{4}\left(1 - e^{2i\lambda H}\right)^2 - \dots . \tag{C.10}$$

Recalling the constant-N solution $\hat{w}_0^{\pm}$, where $+$ refers to the solution for $z > z_0$ and $-$ refers to the solution for $z < z_0$, the first-order expansion in γ can be written

$$\hat{w}_1 \approx \begin{cases} \hat{w}_0^- + \frac{\gamma}{2} e^{2i\lambda H}\left(1 - e^{-2i\lambda z_0}\right)\hat{w}_0^- & 0 \le z < z_0 \\ \hat{w}_0^+ + \frac{\gamma}{2} e^{2i\lambda H}\left(1 - e^{-2i\lambda z_0}\right)\hat{w}_0^- & z_0 < z \le H \end{cases} \tag{C.11}$$

Finding the higher-order terms is straightforward and the nth-order term is:

$$\left(\frac{\gamma}{2}\right)^n \left(e^{2i\lambda H} - 1\right)^{n-1} e^{2i\lambda H}\left(1 - e^{-2i\lambda z_0}\right)\hat{w}_0^- . \tag{C.12}$$

As in the constant-N case, we solve for the buoyancy by multiplying by $-N_1^2/s$ and inverting the Laplace and Fourier transforms. In this way, we calculate successively higher order approximations to the buoyancy in the troposphere and eventually determine the series converges to

$$b_{\text{point}}^{\text{leaky}}(x,z,t) = b_{\text{point}}^{\text{no lid}}(x,z,t) \times \frac{1+\gamma}{1 + (2\gamma + \gamma^2)\sin^2\left(\frac{HN_1 t}{x}\right)} \qquad z \le H. \tag{C.13}$$

The solution for $N_1 \neq N_2$ is just the constant-N solution (C.6) multiplied by a new factor. Note that this expression does not rely on the smallness of γ; it is valid over the entire range of N_2/N_1 from 0 to ∞, which corresponds to $\gamma = -1$ to ∞.

Since the multiplicative factor that converts the constant-N solution (C.6) to the differing-N solution (C.13) is independent of z, the solution for the buoyancy source with baroclinic structure given by (4.8) follows easily from equation (C.7):

$$b_m^{\text{leaky}}(x,z,t) = b_m^{\text{no lid}}(x,z,t) \qquad \times \frac{1+\gamma}{1 + (2\gamma + \gamma^2)\sin^2\left(\frac{HN_1 t}{x}\right)} \qquad z \le H\,. \tag{C.14}$$

This solution is the same as the tropospheric part of equation (4.13). Following a similar set of steps reveals the stratospheric part of the solution.